Numerical Predictions of Airfoil Acoustics with Inflow Turbulence

MT54035 MT MSc Thesis

G.J. Dekkers

Delft University of Technology

TU Delft

MARIN

Thesis for the degree of MSc in Marine Technology in the specialization of Ship Hydromechanics

Numerical Predictions of Airfoil Acoustics with Inflow Turbulence

By

G.J. Dekkers

Performed at

Maritime Research Institute Netherlands (MARIN)

This thesis (**MT.23/24.030.M**) is publicly available in accordance with the general conditions for projects performed by the TU Delft.

To be defended publicly on June 10 2024.

Company Supervisors
Responsible supervisor: Dr. Artur Lidtke
Daily supervisors: Dr. Artur Lidtke, Dr. Thomas Lloyd, Dr. Fernanda dos Santos

Thesis Exam Committee
Chair/Responsible professor: Prof. Dr. Gabriel Weymouth
Staff member: Prof. Dr. Thomas van Terwisga
Staff member: Dr. Bernat Font
Company member: Dr. Artur Lidtke

Author details
Author: Gert Dekkers
Studynumber: 4902718

Cover: The cover image is adapted from Yelmanov [1]
Style: TU Delft Report Style, adapted by Daan Zwaneveld and Gert Dekkers

An electronic version of this thesis is available at https://repository.tudelft.nl/

TU Delft

Abstract

The interaction of a turbulent flow with the leading edge of a foil is one of the dominant noise sources for many engineering applications, including aircraft wings, (wind) turbine blades, and non-cavitating marine propellers such as those found on tidal turbines, naval vessels and submarines. Incorporating a better understanding of the turbulence intensity on the far-field radiated noise in the early design phases can help reduce low-frequency broadband noise that is harmful to humans and (marine) wildlife. A simple framework, such as that proposed by Amiet, can provide fast predictions once validated for more complex problems. The current work assesses numerical predictions on far-field radiated noise by the leading edge of a NACA0008 airfoil for varying turbulence intensities. The flow is simulated within ReFRESCO, a partially averaged Navier-Stokes solver in which turbulence is generated using a synthetic inflow turbulence generator. Inflow turbulence and predicted far-field noise by the Ffowcs Williams-Hawkings formulations are experimentally and numerically validated, showing that the proposed method can generate realistic turbulence, pressure data on the foil surface and associated far-field noise. Variation in the turbulence intensity shows an unwanted change in the integral length scale, which did not seem to affect the far-field radiated noise. In agreement with Amiet, a linear increase in turbulence intensity leads to a near quadratic increase of the radiated noise for a receiver directly above the foil. A rapid change in scaling is seen for receivers more closely aligned with the flow direction both up- and downstream of the foil, for which the far-field noise scales with the turbulence intensity to the sixth power. Variations in the turbulence intensity between 4 % and 16 % dominate over a change in the integral length scale from 30 mm to 65 mm.

Preface

Before you lay the figurative last leg of a journey that started in 2018. A journey of six years, two diplomas, numerous friends and even many more insights gained. This journey, concluded by this master thesis, would not have been possible without the support of numerous people, too many to name. Words cannot express my gratitude towards them, especially for helping me navigate through the topic of turbulence within this thesis. One that is often stamped as complex, or as Peter Bradshaw put it:

"the whole phenomenon of turbulence was probably invented by the Devil on the seventh day of Creation when the Good Lord wasn't looking."

A topic that sparked my interest from one of the first courses I took in the master's: Advanced Fluid Dynamics. Even though that course did not contain much turbulence content, it directed my interest towards fluid dynamics. So when Prof. Dr. Tom van Terwisga offered this assignment, I knew I wanted to accept it. It contained another topic I was also interested in and one that I was keen on learning more about acoustics and CFD, respectively. As stated, completing this assignment would not have been possible without the help of numerous people.

First, I would like to thank the supervisors who guided me through the project. Thanks to Prof. Dr. Gabe Weymouth for keeping me on track and for also letting me experience the pitfalls that research has to offer. Additionally, many thanks for the interesting meetings that we had weekly together with Kiki and Zhihong. Thanks also to Dr. Artur Lidtke and Dr. Thomas Lloyd for their extended knowledge of the subjects, which helped me move forward whenever I felt stuck. Many thanks also to them for familiarising me with computational fluid dynamics and associated post-processing. Accordingly, thanks to MARIN for allowing me to perform this assignment with them and for providing me with the computational resources (ReFRESCO and the cluster). Special thanks to Dr. Fernanda dos Santos for providing me with her experimental results, which were much needed to make this project successful. Also, many thanks for sharing your in-depth knowledge of airfoil acoustics and the Amiet framework, which helped me interpret my results.

Finally, thanks to all my friends and family for your support: my roommates Evert, Floor and Marco for sharing the highs and lows of our academic careers and the many fun activities that we did together; the students at MARIN who were able to give me new insights into the project or distract me with a game of table tennis; Bas, Frans, Jurn, and Pieter for being amazing friends and the many (political) maritime related discussions that we had. Lastly, my greatest thanks to my mom and dad, who supported me during my whole academic career no matter my decisions and always showed great interest in my work. These six years, the diplomas, the numerous friends and the many insights have all been made possible by everyone who supported me. For that, I say thank you! Bedankt!

Gert Dekkers
Delft, May 2024

Contents

List of Figures

List of Tables

Nomenclature

Below is a list of abbreviations and symbols. Both abbreviations and symbols will be defined in text for the first time of usage. If not otherwise stated, the coordinate system is Cartesian, where (x, y, z) are in the streamwise/flow, vertical, and spanwise directions, respectively. The origin of the coordinate system is midspan on the (intended) leading edge of the foil.

Abbreviations

Abbreviation	Definition
Avg	Average/mean
CFD	Computational fluid dynamics
DB	Dampening box
dB	Decibel
DDES	Delayed DES
DES	Detached eddy simulations
DNS	Direct numerical simulations
Exp	Experiment
FW-H	Ffowcs Williams-Hawkings
IDDES	Improved DDES
iLES	Implicit LES
ITG	Inflow turbulence generator
LE	Leading edge
LES	Large eddy simulations
LLM	Log-layer mismatch
MARIN	Maritime Research Institute Netherlands
Max	Maximum
MSD	Modelled stress depletion
NuTTS'24	Numerical Towing Tank Symposium 2024
NS	Navier-Stokes
PANS	Partially averaged Navier-Stokes
PDS	Porous data surface
PSD	Power spectral density
p.d.u	Procedure defined unit
RANS	Reynolds-averaged Navier-Stokes
RDT	Rapid distortion theory
RMS	Root-mean-square
SDS	Solid data surface
SGS	Sub-grid scale
Sim	Simulation
SIMPLE	Semi-implicit method for pressure linked equations
SRS	Scale-resolving simulations
Std	Standard deviation
TE	Trailing edge
TSA	Transient scanning analysis
URN	Underwater radiated noise
VK, vK	Von Kármán
WP	Wall pressure
WPF	Wall pressure fluctuations

Symbols

Symbol	Definition	Unit
a	Fitting parameter	p.d.u.
B	Spectrum bandwidth	Hz
b	Amplification factor	-
b	Fitting parameter	p.d.u.
C_{xx}	Unbiased autocovariance	p.d.u.
$C_{xx,biased}$	Biased autocovariance	p.d.u.
c	Airfoil chord	m
c_∞	Speed of sound in air	m/s
d	Airfoil span	m
d	Bar thickness	m
$d_{\frac{1}{2}}$	Half airfoil span	m
$F_{b,i}$	Body force for i-th velocity component	N/m^3
f	Frequency	Hz
f_c	Centre frequency	Hz
f_{cut}	Mesh cut-off frequency	Hz
f_{low}, f_l	Lower frequency integration bound	Hz
G_{pp}	One-sided power spectral density of pressure fluctuations	Pa^2
$H(f)$	Heaveside function for surface f	-
k_e	Wavenumber of the largest eddies	1/m
k_x	Streamwise wavenumber	1/m
$k_{\%}$	Coverage factor	-
$\mathcal{L}$	Aeroacoustic transfer function	p.d.u.
L	Longitudinal position in wake	m
L_{ITG}	Thickness of ITG in streamwise direction	m
L_x	Integral length scale in the x-direction	m
L_γ	Coherence length	m
l	Length scale	m
M	Grid spacing	m
M	Mach number	-
$\hat{\mathbf{n}}$	Normal vector to surface f	-
p	Pressure	Pa
p_{ref}	Reference pressure	Pa
p'	Far-field radiated fluctuating pressure	Pa
R^2	Coefficient of determination	-
R_{11}	Two-point velocity correlation	m^2/s^2
$R(\tau)$	Autocovariance as a function of the time lag	m^2/s^2
$\mathbf{r}$	Longitudinal separation vector, $\mathbf{r} = (r_1, 0, 0)$	m
$\mathbf{r}$	Position of acoustic observer/receiver, $\mathbf{r} = (x_o, y_o, z_o)$	m
$\hat{\mathbf{r}}$	Vector in radiation direction	-
$r_{m,l,i}$	Point in m-th and l-th direction for i-th velocity component	-
r_{LE}	Airfoil leading edge radius	m
r_1	Longitudinal separation of correlation points	m
S	FW-H surface	m^2
$SPL_{corrected}$	SPL_{sim} corrected for turbulence intensity	dB
SPL_{sim}	Sound pressure level from simulation as predicted by FW-H	dB
SPL_γ	Sound pressure level corrected for span	dB
S_{xx}	One-sided autospectral density function	p.d.u.
$\mathcal{T}$	Integral timescale	s
T	Signal length	s
TI	Turbulence intensity, $TI = u_{rms}/\overline{u}$	%
TI_{Ci}	Turbulence intensity for case i	%
t	Time	s

Symbol	Definition	Unit
t_{max}	Airfoil maximum thickness	m
$U_{95,dB}$	Expanded uncertainty of PSD calculation	dB
$U_{95,m}$	Expanded uncertainty of the mean value	p.d.u.
U_{inf}	Set inflow velocity	m/s
u	Local instantaneous streamwise velocity, $u = \overline{u} + u'$	m/s
u_i'	Local instantaneous velocity fluctuation in i-th coordinate direction	m/s
$\overline{u_i}$	Local mean of velocity in i-th coordinate direction	m/s
u_n	Velocity in the surface normal direction	m/s
u_r	Velocity in the radiation direction	m/s
u_{ref}	Reference velocity	m/s
u_{rms}	Root-mean-square of the local streamwise velocity fluctuations	m/s
u_s	Velocity deficit in wake	m/s
u_1	Random standard uncertainty at first-order replication level	p.d.u.
x	Location vector, $\mathbf{x} = (x, y, z)$	m
x_o	Position of observer on x-axis	m
y	Location vector of generated fluctuations on surface f	m
y_o	Position of observer on y-axis	m
y_1	Cell size of first cell on foil surface	m
y^+	Wall-normal normalized first cell size	-
z_o	Position of observer on z-axis	m
Γ	Gamma function	-
γ	Coherence, $\sqrt{\gamma^2}$	-
γ^2	Magnitude squared coherence	-
Δd	Spanwise spacing of measurement positions	m
Δt	Timestep	s
Δt^*	Non-dimensional timestep, $\Delta t^* = \Delta t \cdot U_{inf}/c$	-
Δx	Cell size in the x-direction	m
θ	Angle of acoustic probe/receiver	Degrees
κ	Wavenumber, $\kappa = 2\pi/l$	1/m
Λ_f	Integral length scale in the flow direction	m
ν	Kinematic viscosity	m^2/s
ρ	Density of air	kg/m^3
ρ_{fit}	Fit of the autocorrelation	-
$\rho(\tau)$	Autocorrelation as a function of the time lag	-
σ_{u_i}	Standard deviation of velocity signal	m/s
σ^2	Measurement of observer position	m^2
τ	Retarded time	s
τ	Time lag between times t_2 and t_1	s
τ_w	Wall shear stress	$kg/(ms^2)$
Φ_{uu}	Power spectral level of the streamwise velocity	dB
Φ_{uu}^{vK}	One-dimensional turbulence spectrum in x-direction based on Von Kármán	dB
Φ_{vv}^{vK}	Two-dimensional turbulence spectrum in y-direction based on Von Kármán	dB
$\phi_i(t)$	Instantaneous quantity in i-th coordinate direction, $\phi_i(t) = \overline{\phi_i} + \phi_i(t)'$	p.d.u.
$\phi_i(t)'$	Fluctuation of instantaneous quantity in i-th coordinate direction	p.d.u.
$\overline{\phi_i}$	Mean of quantity in i-th coordinate direction	p.d.u.
ϕ_{pp}	Power Spectral Density of pressure fluctuations	Pa^2
ϕ_{uu}	Power Spectral Density of the streamwise velocity	$(m/s)^2$
ω_z	Spanwise vorticity	1/s
ω_z^*	Nondimensional spanwise vorticity, $\omega_z^* = \omega_z \cdot c/U_{inf}$	-

1

Introduction

Noise pollution from ships, wind turbines and aircraft has been know to impact both people and wildlife negatively [2]–[4]. While, for example, noise control onboard ships has been properly regulated [3], awareness has also been raised for underwater radiated noise (URN) [5]. It is the low-frequency broadband noise component, which can travel over large distances, that is mostly relevant for (marine) wildlife, impacting their natural mating and hunting behaviour [2], [4]. The low-frequency noise is dominated by the interaction of a body with a turbulent inflow. Examples of engineering applications where this dominates are wind turbine blades [6], aircraft wings, turbine blades [7], (air)foils [8] and propellers [9]. The latter mainly applies to non-cavitating propellers, such as for naval or research vessels or in the wake of a submarine [10]. Even for a cavitating propeller, the non-cavitating low-frequency noise source can dominate if the turbulence intensity is sufficiently high [11].

The main phenomenon that radiates low-frequency noise from the mentioned engineering applications is the impingement of turbulent structures on the foil's leading edge. The turbulence distortion generates pressure fluctuations on the surface of the foil, thereby radiating sound to the far-field [11]. Understanding this turbulence-body interaction is, therefore, key to predicting far-field noise and options to mitigate it. Initial research on leading edge noise focussed on incompressible gusts for flat plates [12], [13]. This was extended to compressible gusts at an angle [14] and later to two-dimensional gusts [15], [16]. The framework as presented by Amiet [17], who proposed a formulation to calculate the far-field radiated noise, is still being used nowadays due to its simplicity. However, these works all fell short in modelling the influence of the foil in the turbulent flow, i.e. they assumed flat plate conditions. One of the first methods that improved on this included the rapid distortion theory to calculate the velocity around bluff bodies [18].

Studies in the early 2010s tried to assess the effects of geometric properties of the foil, such as the leading edge radius, thickness, camber, chord length, curvature and angle of attack on the far-field radiated noise [19]–[22]. Airfoil camber, angle of attack and chord length were reported to have a minor effect on the leading edge radiated noise. The geometric properties forward of the maximum thickness, thus describing the leading edge, were found to influence the generated sound more [22]. Since the geometric properties of the foil on far-field noise have been well documented, this work will focus on the inflow turbulence. This adheres to the current trend that designs for the mentioned applications are often made based on requirements other than noise pollution. Noise prevention is thus overlooked, whereas noise mitigation by studying inflow turbulence parameters is more useful.

Recent works readily studied turbulence parameters on far-field noise. Bowen et al. [23] studied the far-field radiated noise experimentally by placing grids for turbulence generation in a wind tunnel. They reported increased far-field noise for increased turbulence intensity and integral length scale. No attempt was, however, made to separate the effects of these turbulence parameters. Additionally, measurements close to the leading edge were impossible due to the finite size of the measurement probes. This is similar to what is reported in the works by Dos Santos et al. [24], Botero-Bolívar et al. [25] and Dos Santos et al. [26]. In those works, the turbulence intensity was altered by increasing inflow velocity, and hence, an increase in integral length scale was achieved as well. It becomes clear that the literature lacks research into a change in turbulence intensity, without altering or accounting for other flow variables such as the inflow velocity in the results.

To address this research gap, the current work will focus on a pure increase in turbulence intensity on the far-field radiated noise by the leading edge of an airfoil. If separation is not possible an attempt will be made to attribute the resulting far-field noise to the different turbulence parameters. Results will be compared to the scaling for turbulence intensity as proposed by Amiet [17], which could promise to be useful in early design phases if validated for more complex problems. This work aims to establish the effect of turbulence intensity on far-field radiated noise and, accordingly, to show whether the predicted increase by Amiet is correct. These combined goals give insight into scaling laws of far-field noise based on the inflow turbulence (turbulence intensity) such that estimates of far-field noise increase or decrease can be made in the initial stages of the design. A numerical framework will be adopted to achieve this goal. Lidtke et al. [27] have readily shown that realistic turbulence can be generated that allows for the prediction of far-field noise. Additionally, both Piccolo et al. [28] and Ribeiro et al. [29] have shown promising results for numerically predicted far-field noise from airfoils.

1.1. Research question and structure of the report

The main research question that will be answered in this report is:

How do different turbulence intensities in generated inflow turbulence affect the numerically predicted magnitude and directionality of airfoil leading edge noise, and how does this compare to the scaling proposed by Amiet?

To answer this question, several steps are taken. A review of the literature is divided into two parts. The first part of the literature, Chapter 2, discusses relevant noise mechanisms from an airfoil. Additionally, it presents the expected effect of the turbulence intensity and integral length scale on leading edge radiated noise. The latter is discussed in case an unwanted change of integral length scale is induced for varying turbulence intensity. It will also present methods from the literature that can be used to quantify the turbulence intensity and integral length scale. The second part of the literature review, Chapter 3, shows the advantages of using computational fluid dynamics over experiments. Several turbulence modelling approaches will be presented, together with their (dis)advantages. Requirements for artificial turbulence generation will be given based on a review of experimental turbulence generation. Accordingly, several methods to generate turbulence artificially will be described. At last, two methods for far-field noise prediction will be presented.

Next, in Chapter 4, the methodology for simulating inflow turbulence and predicting far-field noise will be presented based on arguments from the literature review. Several post-processing tools used in the chapters hereafter will also be discussed. A concise verification study regarding mesh resolution and spanwise domain size will also be presented. Chapter 5 presents results for the extensive validation of the methodology as proposed in Chapter 4. Based on the validated methodology, results for cases with varying turbulence intensity will be presented in Chapter 6. The discussion and interpretation of the results will also be given in that chapter.

Chapter 7 summarises the main steps and findings regarding turbulence generation, turbulence simulation, far-field acoustics and comparisons to the Amiet framework. At last, Chapter 8 presents several recommendations for further research.

1.2. Contributions

Besides this master thesis report, a closed exam (defence) and a public presentation, a part of the work is also documented in a paper (extended abstract) titled "*Quantifying the effect of turbulence intensity on turbulence-interaction noise of an airfoil using scale-resolving simulations*". This paper will be submitted to the 26th Numerical Towing Tank Symposium (NuTTS'24), which will take place in October 2024 in Duisburg, Germany. For more information on the conference, the reader is referred to their website. The current draft of the paper can be found in Appendix A. The draft is based on information found within this work but may be altered after handing in the final version of this report. The paper, as well as this report, have been written by G.J. Dekkers. All other authors (mentioned in the paper) will only partake in the paper once the MSc Thesis has been handed in and graded.

2

The airfoil as a noise generator in turbulent inflow

This chapter will describe the airfoil as a noise generator in a turbulent flow. Section 2.1 will describe basic airfoil noise mechanisms. Section 2.2 will present more details on the influence of the turbulence intensity and integral length scale on the leading edge radiated noise. Finally, Section 2.3 will present several methods to calculate the turbulence intensity and integral length scale, as they vary in literature.

2.1. Airfoil noise mechanisms

Noise generation from airfoils is typically divided into cavitating and non-cavitating induced noise. Cavitating noise, the collapse of a bubble creating a shockwave, is stated to be the dominant noise source for marine propellers, especially at higher velocities [9]. Improvements often focus on increasing the speed at which cavitation occurs, thereby delaying the cavitation-induced noise. On the other hand, there is non-cavitating induced noise, which is dominant in non-cavitating applications. Apart from non-cavitating marine propellers, such as those for navy and research vessels, other applications are hydrofoils, rudders, wind turbine blades, rotor blades or turbine blades [6]–[8]. Even for cavitating marine propellers the non-cavitating induced noise can be dominant if the turbulence intensity of the inflow is sufficiently high [11, p. 139–143], showing the significance of research into non-cavitating induced noise.

Non-cavitating induced noise can be further divided into two categories based on the characteristics of the sound pressure spectrum [30, p. 75–76]:

1. Tonal noise is the noise generated by the interaction of the foil with the periodic incoming flow. This mechanism is also called self-noise.
2. Broadband noise is the noise generated by the interaction of the foil with (random) fluctuations in the flow field. This mechanism is also called interaction noise.

The current work will only focus on the broadband noise component generated by the foil. This broadband component is generally induced at one of two locations, either at the leading edge or the trailing edge. Figure 2.1 shows these two components for an airfoil in a turbulent inflow. Trailing edge noise is generated at the rear of the foil. The sound is radiated either by the interaction of the boundary layer with the foil leading to pressure fluctuations on the surface of the foil; the separation of the flow from the foil at angles of attack where stall occurs; the vortex shedding at the trailing edge due to bluntness leading to pressure fluctuations in the flow and on the trailing edge of the foil; the interaction between the upper and lower surface flows when they rejoin at the trailing edge creating vortices and hence pressure fluctuations in both the flow and on the trailing edge; or a combination of these [8], [30, p. 75–76], [31], [32]. Since the current work only focuses on leading edge radiated noise, these mechanisms must be removed from or quantified in the results. It will become clear in Section 5.3 how this will be done.

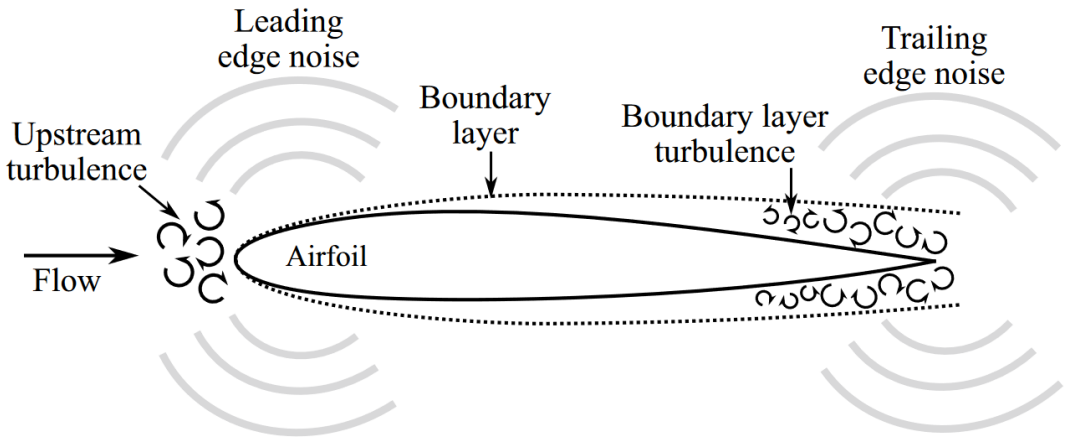

Figure 2.1: Airfoil in a turbulent inflow showing leading edge and trailing edge noise production mechanisms [11, p. 140].

Leading edge radiated noise is generated at the front of the foil. It is generated when a turbulent inflow impinges on the airfoil's leading edge, creating unsteady pressure fluctuations on the surface of the airfoil and, hence, sound. These unsteady pressure fluctuations follow from the energy-containing eddies spreading their energy from the flow direction into the other two directions. This is done most efficiently in the vertical direction since the surface of the foil extends less in that direction compared to the spanwise direction. This was already implied by Figure 2.1, but Figure 2.2 also shows this (exaggerated) dipole shape. The efficiency at which the distortions on the leading edge occur will be discussed in the next section. However, a second mechanism can induce sound at the leading edge: the complex flow coupling close to the leading edge. Not only do the eddies induce an unsteady pressure on the foil, they can also interact with the incoming turbulence by the (back)scatter from the leading edge. Similar to the rejoining of the boundary layers at the trailing edge of the foil, this can create vortices and, thus, unsteady pressure fluctuations in front of the foil. This, in turn, can then affect the unsteady pressure fluctuations on the surface of the foil, indicating the complex coupling of the flow and the foil [9], [11], [30]. Now that the main airfoil noise mechanisms have been introduced, it is key to discuss the expected efficiency at which the leading edge mechanisms work based on different turbulence parameters. This will be done in the next section.

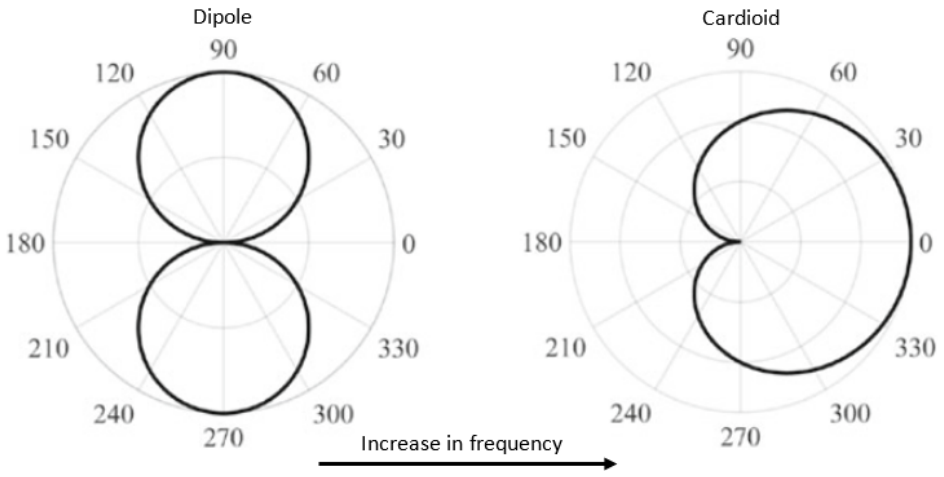

Figure 2.2: Noise directivity patterns for airfoil leading edge radiated noise in a turbulent inflow. The flow is from left to right and the leading edge is at the origin. Adapted from Doolan et al. [11, p. 142].

2.2. Turbulence intensity and integral length scale on radiated noise

Turbulent inflows for the previously named applications can be generated in many ways. Turbine and rotor blades can experience inflow turbulence from the wind, boundary layer effects from the ground [33] and wake effects from other blades. Marine applications will often only experience effects induced by the boundary layer of the ship or the wake of appendages. The efficiency at which these inflows generate noise at the leading edge of a foil not only depends on the operating point of the application but also on the parameters that define the inflow turbulence. Two main parameters defining the turbulent inflow are the turbulence intensity (TI) and integral length scale in the direction of flow (Λ_f).

The turbulence intensity is directly linked to the magnitude of the generated sound. The turbulence intensity is associated with the level of fluctuations compared to the velocity. From Section 2.1, it became clear that the eddies direct their energy away from the flow direction and (mostly) into the vertical direction. If the turbulence intensity is higher, these eddies will contain more energy, allowing them to redistribute more energy to the other directions. This, in turn, leads to bigger unsteady pressure fluctuations on the foil and thereby radiated sound. It was proven by Bowen et al. [23] that turbulence interaction noise significantly increased with increasing turbulence intensity. However, within that research, the effect of the integral length scale was not decoupled from the turbulence intensity. Intended or not, most works found in the literature suffer from this problem [25], [26]. In this work, an attempt will, therefore, be made to split the effect of the intensity and integral length scale from one another.

Additionally, often research is performed into the effect of the increase of velocity fluctuations which is not necessarily an increase of turbulence intensity. Likewise, with the increase in integral length scale, bigger velocity fluctuations are often achieved by increasing the inflow speed. While the fluctuations indeed increase, the turbulence intensity can stay similar due to the proportional increase of inflow speed [24]–[26]. The literature lacks research into the effect of solely changing the turbulence intensity on leading edge radiated noise, hence signifying the added value of this work.

A similar line of reasoning can be followed for the integral length scale. The integral length scale falls in the first of three wavenumbers of the energy spectrum: the energy-containing range. Figure 2.3 shows the three-dimensional energy spectrum in which a wavenumber is defined as $2\pi/l$ with l the length scale. As the name states, the energy-containing range contains the largest flow structures and energy. These structures have the largest effect on the magnitude of the radiated noise since they carry more energy than smaller structures. Moving to larger wavenumbers results in going into the inertial subrange, representing the change from the macrostructure (integral length scale) to the microstructure (Taylor microscale) by energy cascade. Finally, it moves into the dissipation range, where the energy from the microstructure is dissipated (into heat) [34, p. 182–195], [35, p. 190–192]. Throughout this work, the integral length scale input is kept constant to solely study the effect of turbulence intensity. It has readily become clear that such a separation is difficult, if not impossible, and later on it will become clear if the separation was successful.

Works on leading edge radiated noise for a change of integral length scale are also scarce. Initial works focussed on modelling the incoming turbulence as a gust. These methods failed to include the effect of the foil, i.e. they assumed flat plate conditions [12], [14], [16]. Improvements over time were made, and several works investigated limited ranges of integral length scales [25], [26], [28], [29]. Conclusions about the effect of the integral length scale on the radiated sound are difficult to make since all of these works experience the problem of increased fluctuations and/or inflow speed, making it hard to quantify the actual effect of the integral length scale compared to the other turbulence parameters. Bowen et al. [23] have shown that the behaviour of the flow near the leading edge depends on the eddy size. They stated that smaller flow structures are broken up near the leading edge, whereas larger ones distort and tend to become more two-dimensional rather than break up. This is in line with the Rapid Distortion Theory (RDT) where the larger structures indeed show behaviour similar to vortex stretching [35, p. 153, 240–244]. This is also confirmed by the acoustic pattern around the leading edge, which was readily visible in Figure 2.2. At low frequencies (bigger length scales), the noise directivity is a pure dipole since the turbulence has time to distort around the leading edge. Higher frequencies (small length scales) do not have this time and tend to break up with sound mainly being produced in the direction of the flow leading to the cardioid pattern [11, p. 139–143]. As stated, the integral length scale input is kept constant throughout this work. Suppose it changes by changing the turbulence intensity. In that case, a scaling method will be investigated to either remove the effect of the length scale or to investigate it separately, showing added value to the literature.

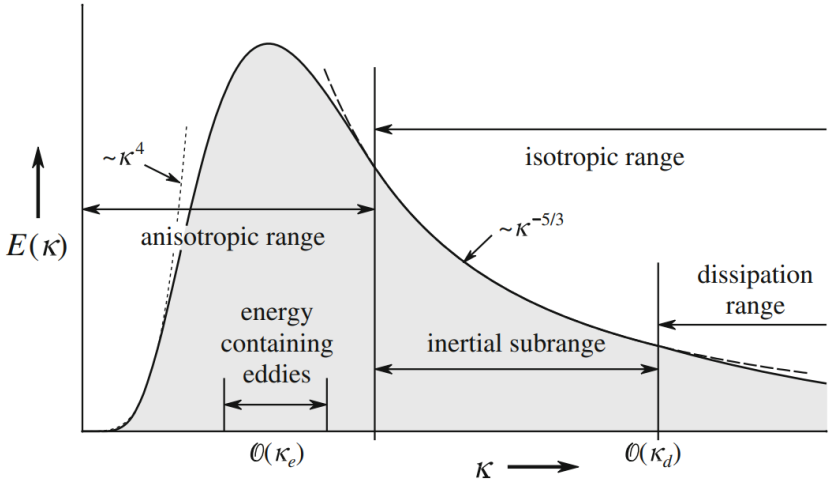

Figure 2.3: Three-dimensional energy spectrum showing the three ranges in association to the wavenumber based on the integral length scale (κ_e) and the Taylor microscale (κ_d) [35, p. 191].

2.3. Computational methods for turbulence intensity and integral length scale

In literature, several methods exist to calculate the turbulence intensity. The baseline for all these methods is dividing the root-mean-square fluctuating velocity component(s) by a mean velocity. These components follow from the Reynolds decomposition of a signal, which states that an instantaneous quantity $\phi_i(t)$ can be split into the average over time $\overline{\phi_i}$ plus an instantaneous fluctuation $\phi_i'(t)$. In this way, the velocity fluctuations can be defined as $u_i'(t) = u_i(t) - \overline{u_i}$ where i indicates the velocity component. As stated, the mean component is taken over time such that

$$\overline{u_i} = \lim_{T\to\infty} \frac{1}{T} \int_0^T u_i(t)dt. \tag{2.1}$$

The time element from the velocity fluctuations can be removed by taking the root-mean-square of the signal, giving the standard deviation of that signal at location **x**

$$\sigma_{u_i}(\mathbf{x}) = u_{i,rms}(\mathbf{x}) = \sqrt{\overline{u_i(t)'^2}}. \tag{2.2}$$

Here **x** is defined as the location vector with $\mathbf{x} = (x, y, z)$ and the mean is again taken over time [35, p. 75–77]. From this, the most common definition of the turbulence intensity, based on all velocity components, becomes [35, p. 128]

$$TI(\mathbf{x}) = \sqrt{\frac{\frac{1}{3}\cdot(u_{rms}^2 + v_{rms}^2 + w_{rms}^2)}{\overline{u}^2 + \overline{v}^2 + \overline{w}^2}}. \tag{2.3}$$

It should be noted that all of these components are a function of the location vector **x**, but for clarity, these dependencies have been removed from the equation.

Although this formulation captures all three velocity components, it is unnecessary for the current problem for two reasons. First, even though there will be velocity fluctuations in all three directions, a mean velocity will only be created in the streamwise (x) direction signifying that $\overline{v} = \overline{w} = 0$ m/s. Second, the turbulence within this work will be mainly isotropic such that $u_{rms} = v_{rms} = w_{rms}$, meaning that Equation 2.3 can be simplified to

$$TI(\mathbf{x}) = \frac{u_{rms}}{\overline{u}}. \tag{2.4}$$

This method is also proposed by Hinze [36, p. 4]. It will be used mostly throughout this work since it only requires the measurement of the mean velocity in the streamwise (x) direction, thereby relaxing the

requirements set for experimental data without losing accuracy on the calculated turbulence intensity, assuming that the turbulence is indeed isotropic. If experimental results do not present fluctuations in all three directions, the statement of isotropy should be checked in another way. An alternative to Equation 2.4 is to replace the local mean speed $\overline{u}$ by the set inflow velocity U_{inf}. This makes it easier to evaluate the turbulence intensity close to the leading edge since the local mean tends to zero, rendering infinite values for the intensity otherwise.

Similar to the turbulence intensity, several methods exist to calculate the integral length scale. The integral length scale of the turbulence can be calculated by applying either a spatial or time correlation. The spatial correlation relies on the simultaneous measurement of the velocity fluctuations at two points $\mathbf{x}_1$ and $\mathbf{x}_2$ in the flow. The integral length scale in the flow direction Λ_f can then be calculated as

$$\Lambda_f = \frac{1}{\overline{u'^2}} \cdot \int_0^\infty R_{11}(\mathbf{r}) dr_1, \tag{2.5}$$

with R_{11} the two-point correlation based on a pure longitudinal change of the separation vector **r**

$$R_{11} = \overline{u'_1(\mathbf{x}_1) u'_1(\mathbf{x}_2)}. \tag{2.6}$$

This method, as proposed by Nieuwstadt et al. [35, p. 188–192] is, however, not preferred since it does not allow for length scale computations close to foil due to the need for a separation vector. That separation vector cannot exist due to the presence of the airfoil wall. Additionally, since the separation vector relates the turbulence at two points, it signifies that turbulence must be homogenous between those two points. And although homogenous isotropic turbulence is required within this work, it does not have to be throughout the whole domain. Especially close to the turbulence generation point, the turbulence may very well be inhomogeneous, which is not allowed for in this method. The integral length scale from the two-point correlation is, therefore, not a suitable method.

A similar method based on a time correlation instead of a spatial correlation removes this need for homogeneous turbulence and can be applied anywhere within the domain. Explained in more detail in Pope [34, p. 65–69] and Nieuwstadt et al. [35, p. 183–186], they state that the integral length scale can be calculated from

$$\Lambda_f = \overline{u} \cdot \mathcal{T} = \overline{u} \cdot \int_0^\infty \rho(\tau) d\tau. \tag{2.7}$$

Here $\overline{u}$ represent the mean local streamwise velocity and $\mathcal{T}$ the integral timescale. The latter describes the time over which significant correlation exists and is thus a measure of the macrostructure and associated integral length scale. For Equation 2.7 to be true, the Taylor hypothesis for frozen turbulence must hold, stating that based on an Eulerian measurement the time it takes for an eddy to advect past the measurement point must be much shorter than the time it takes for the eddy to change size, i.e. the turbulence is frozen [35, p. 194–195],[37]. This allows the integral timescale to be multiplied by the mean local velocity by which the eddy is advected. Similar to the spatial correlation, this has the downside of being less accurate for rapidly changing eddies which is likely to occur close to the turbulence generation point. Nonetheless, according to Pope [34, p. 65–69] and Lin [38] this hypothesis provides accurate results as long as $u^2_{rms} << \overline{u}^2$. Within this work u^2_{rms} was always at least one order of magnitude smaller than $\overline{u}^2$ at locations where interest is shown in the integral length scale.

The integral timescale from Equation 2.7 follows from the integration of the normalised autocovariance such that

$$\mathcal{T} = \int_0^\infty \rho(\tau) d\tau = \int_0^\infty \frac{R(\tau)}{\overline{u'^2}} d\tau = \int_0^\infty \frac{\overline{u'(t_1) u'(t_1+\tau)}}{\overline{u'^2}} d\tau. \tag{2.8}$$

Indeed, here it becomes clear that the integral timescale is only a function of the difference in time and not space, with $\tau = t_2 - t_1$. From Equation 2.8 it also obvious that for $\tau = 0$ s, the autocorrelation becomes 1, i.e. $\rho(0) = 1$. All properties that the autocorrelation must adhere to are [35, p. 184]

$$\begin{aligned} i: &\quad \rho(0) = 1, \\ ii: &\quad |\rho(\tau)| \leq \rho(0) = 1 \quad \forall t, \\ iii: &\quad \rho(\tau) = \rho(-\tau), \\ iv: &\quad \rho(\tau) \to 0 \; for \; \tau \to \infty. \end{aligned} \tag{2.9}$$

Properties i to iii are often not problematic, property iv however is. Both Bowen et al. [23] and Ribeiro et al. [29] show that the autocorrelation indeed goes to zero for an infinite time lag but that it additionally starts to oscillate around zero. The associated side effect is that the integral from Equation 2.7 cannot be performed until infinity. A possible solution, also adapted by Ribeiro et al. [29], is to find the first zero-crossing of the autocorrelation. This method works if property iv is satisfied based on a smoothly decaying curve. This is also not always the case since the autocorrelation could oscillate around a non-zero value before reaching zero. An example of this, and the oscillating behaviour around zero, is given in Figure 2.4. Indeed, one can observe the small fluctuations around a non-zero value that the orange line experiences for $8 \cdot 10^{-3} < \tau < 3 \cdot 10^{-2}$ s. Even though this seems small, it leads to an approximate 60 % bigger length scale at the two different positions. Ribeiro et al. [29] associate this unwanted behaviour with the autocorrelation being more susceptible to short measurement times, more often found in simulations.

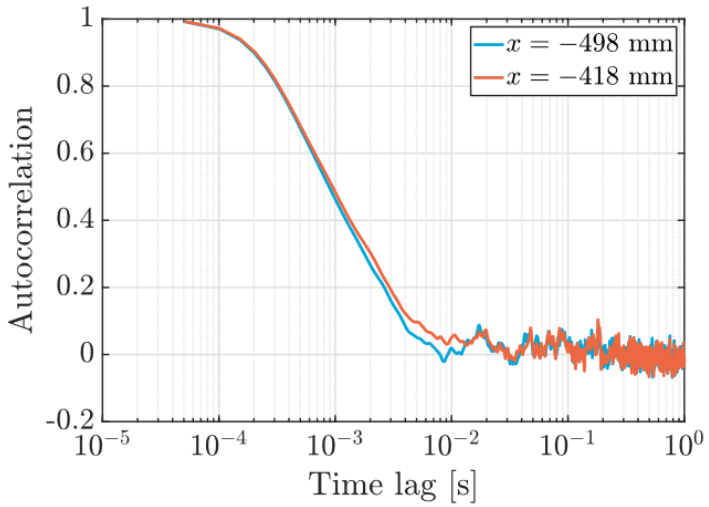

Figure 2.4: Autocorrelation at two positions in the domain from a numerical simulation. Autocorrelation is determined based on Equation 2.8 [29].

Both Trush et al. [39] and Nandi et al. [40] propose different methods that might overcome the non-zero oscillating problem:

1. Fitting of a power spectral density model such as the Von Kármán model. The main assumption here is that the chosen model can describe the turbulence spectrum, which does not necessarily have to be true. Additionally, even if that assumption holds, this method is susceptible to the chosen frequency range over which the fit is applied. This method is, therefore, not preferred for this work.
2. Finding the peak of the power spectral density function such as that shown in Figure 2.3. The integral length scale follows from the frequency where the power spectral density reaches its maximum. This method is also not preferred since spectral figures often do not show a clear peak thereby being susceptible to the user defined maximum.
3. Integrating Equation 2.7 until the value of the time lag where the autocorrelation reaches the critical value of $1/e$ (rather than zero). This is also not preferred since it severely underestimates the integral length scale for cases where the oscillatory behaviour does not occur.
4. Integration of best-fit curves for the autocorrelation. The accuracy of this approach heavily depends on the chosen function for fitting. Nandi et al. [40] proposes to use a one-term exponential decay function. Several functions for fitting have been investigated within this work to determine which describes the autocorrelation most appropriately; the most accurate one will be described in more detail in Section 4.3.

3

Computational fluid dynamics, turbulence generation and acoustics

This chapter will present several topics regarding numerical approaches for investigating leading edge radiated noise. The chapter will start by describing the added value of computational fluid dynamics (CFD) and give a description of turbulence modelling approaches in Section 3.1. Next, in Section 3.2, several turbulence generation mechanisms will be discussed based on requirements from experimental approaches. Finally, Section 3.3 presents two acoustic analogies that can be used to predict far-field radiated noise.

3.1. Numerical approaches for turbulent inflow acoustic problems

One of the biggest decisions within CFD is the choice of the turbulence modelling approach. Before going into that choice, a short evaluation will be given as to why simulations (CFD) have added value to experiments.

3.1.1. CFD versus experiments

Experiments have proven useful for centuries but the development in computational power has changed the use of computational fluid dynamics (CFD) from a research area into a powerful tool. The term CFD encompasses a wide spectrum of numerical models which can solve complex fluid problems [41], [42]. There are many advantages and disadvantages coupled to the use of CFD. A few of those, most related to this work, will be presented below:

- CFD methods are often used since they can save costs compared to experiments. There is no need for physical prototypes, arranging a test location or acquiring expensive measurement equipment. On the other hand, CFD simulations take a lot of man hours to set up and computational time can be expensive, so a trade-off has to be made [43].
- CFD simulations allow for the mapping of flow parameters throughout the whole domain, merely being limited by the storage capacity of a computer. This allows for better understanding and visualisation of flows (by coherence, correlation, etc.). Experiments are often limited by the number of measurement devices, such that flow measurements are only possible at one location or a repetition of experiments must be performed, as was done in Dos Santos et al. [24]. This is supported by the fact that measurement equipment has a finite size and shape, thereby influencing flow parameters making concurrent measurements difficult. Measurement devices in simulations have no weight, dimension, etcetera thereby not influencing the flow.
- Also noted by Dos Santos et al. [24], is the calibration of measurement equipment, which induces an uncertainty in the measured parameters. CFD requires no such calibration, thereby returning exact results from the solver with machine precision. On the other hand, uncertainty is introduced into the solver by choosing methods to discretize the Navier-Stokes equations or other simplifications. To assess these uncertainties, in-depth verification and validation is needed based on experimental results [42].

- Noise measurements in experiments are sensitive to background noise from people, the wind tunnel or other sources. Section 3.2 will describe this problem in more detail. A CFD simulation does not suffer from background noise. Additionally, noise measurements are often only feasible above the foil to prevent interaction between the flow and measurement equipment.
- At last, flow measurements in experiments is limited to feasibly reachable places. Take, for example, the finite size of the probes in Dos Santos et al. [24], which, due to their size, could be placed no closer than 3.5 mm to the leading edge. CFD measurements do not have this problem since probes do not possess physical quantities such as size and weight as introduced before.

In short, CFD simulations have numerous reasons to be preferred over experiments. Care should, however, be taken to ensure that the pros (abundance of measurement data) outweigh the downside of CFD (possible increased costs). Another downside is the simplifications adapted to make the CFD computation viable. One of these simplifications, arguably the most important one in this work, is the choice on how to model the turbulence as will be discussed in the next section.

3.1.2. Turbulence modelling in CFD

One of the most important choices for simulating turbulence problems is the model that will be used to represent the turbulence. It already became clear in Section 2.2 that turbulence cannot be characterised by one specific value. Turbulence is rather a division of energy over different length scales, see Figure 2.3. There are two ways to capture the turbulence at different length scales [42, p. 347–349]:

- Resolving the turbulence is to solve the discretized Navier-Stokes (NS) equations for a specific length scale.
- Modelling the turbulence is to implement an alternative simplified model approximating the turbulence at a specific length scale.

The most accurate method would be to resolve all turbulent length scales up to the smallest scale where energy is contained in the eddies, i.e. the Kolmogorov scale. The turbulence model that does this, is called direct numerical simulations (DNS). DNS resolves the NS equations for all length scales and is thus only dependent on the (controllable) discretization errors. It is the most accurate representation of a flow field that can (currently) be achieved with CFD. For a DNS to be effective, it must capture both the biggest and smallest length scales. This means that the domain must be sufficiently large to capture bigger length scale, whereas the mesh[1] must be small enough to capture small length scales accurately. Both requirements lead to an increase of computational costs and although such detailed flow information can be useful, it is excessive for the analysis performed in this work. Especially since 80 % of the energy is contained in the energy-containing range as depicted in Figure 2.3 [44, p. 197]. The increased computational time and abundance of unnecessary resolution makes that DNS is not a suitable turbulence model for the current work [42, p. 350–363], [44, p. 211–217], [45].

A less computationally expensive turbulence model is the Reynolds-Averaged Navier-Stokes (RANS) method. RANS assumes that an instantaneous quantity can be split into a mean quantity and a fluctuating quantity, similar to that introduced in Section 2.3. It then averages the NS equations, resulting in the loss of the fluctuating component. Removal of these eddies implies that the flow is steady, which is not the case for turbulent flows. The loss of this energy, together with the randomness of the turbulence, will lead to large errors in the outcomes of any parameters other than mean values. This method is, therefore, not suitable to model the turbulence in this work [42, p. 363–365], [44, p. 197–200], [45].

A more suitable method would be one that partially resolves and partially models the turbulence. These methods are called scale-resolving simulations (SRS), i.e. resolution of the turbulence is performed up to a certain length scale. An example of such a method is the large eddy simulations (LES). Within LES the NS equations are only resolved for the largest eddies, thereby reducing the computational cost compared to DNS and increasing the accuracy compared to RANS. It, however, models the effect of the smaller eddies below the mesh limit by applying a sub-grid scale (SGS) [42, p. 366–369], [44, p. 199–210]. The choice of sub-grid scale determines the accuracy of the turbulence model for smaller length scales. Implicit LES (iLES) does not require the choice for a SGS, but bases it on the numerical truncation error. Numerical dissipation in iLES determines the effects of the unresolved eddies [46].

[1] A ‘mesh’ refers to the computational mesh used for the CFD simulation (in literature often referred to as a grid). A ‘grid’ within this work refers to the grid used to generate turbulence, explained in more detail in Section 3.2.

The mechanisms and effects of the three introduced methods so far are summarised in Figure 3.1.

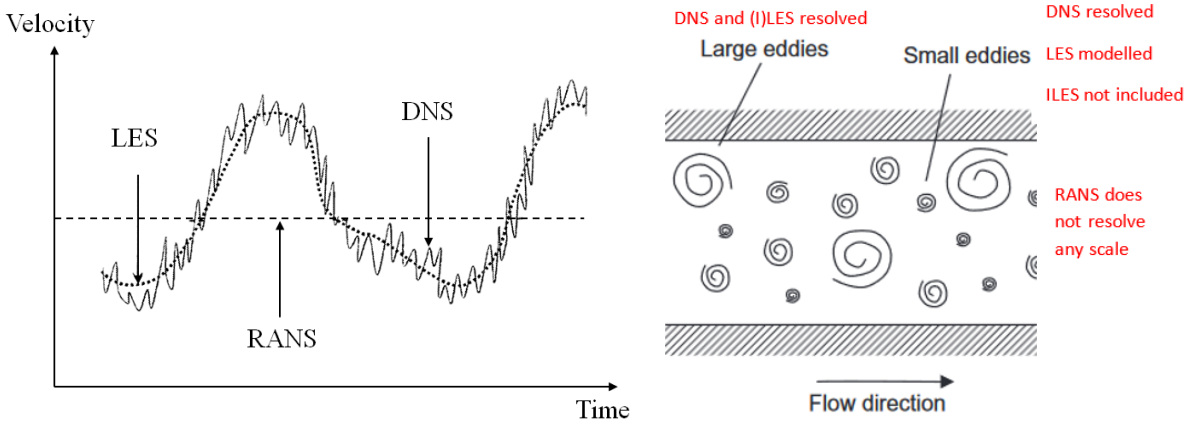

(a) Averaging behaviour of the instantaneous velocities [47].

(b) Resolving and modelling mechanisms, adapted from Tu et al. [48].

Figure 3.1: Mechanisms of DNS, RANS and (i)LES for flow velocity and eddy size.

Although practical, LES suffers from the requirement of finer meshes and possibly smaller time steps for high Reynolds number flows. Especially in the near-wall region, finer meshes are needed if it is required that LES resolves eddies in the near-wall region as well [45], [49]. Liefvendahl et al. [50] have shown that wall-resolved LES can need two to four orders of magnitude more cells to capture the boundary layer accurately compared to wall-modelled LES. The latter still needs much more cells compared to RANS as well. Additionally, Liefvendahl et al. [51] state that RANS allows for much longer (anisotropic) cells in the boundary layer since mean flow quantities are only determined. This is beneficial for the current work, since resolution of the boundary for leading edge noise is not required. The only assumption being made here is that the effect of those eddies does not propagate upstream.

The most suitable method for the current work would, therefore, combine LES and RANS. The detached eddy simulations (DES) framework initially proposed this. Within this method, the near-wall region is treated by RANS, whereas LES is applied to the bulk of the flow. The 'grey area' between the two methods proved problematic unless the switch was abrupt. Otherwise, the region could contain too little resolved turbulence, thus biased towards RANS, resulting in a loss of accuracy. Or too little modelled turbulence, thus biased towards LES leading to expensive computations. This phenomenon, driven by the mesh design, was called the modelled stress depletion (MSD) [52, p. 62]. The delayed detached eddy simulations (DDES) framework improved on this, but likewise to DES still suffered from the log-layer mismatch (LLM) [53]. The LLM, describing the deviation of the wall-shear stress from reality, was reportedly solved by another improved method conveniently named the improved delayed detached eddy simulations (IDDES) [52, p. 63], [42, p. 417–419],[45]. The IDDES framework seems to be the most favourable method for the current work since it applies LES in the bulk of the flow, whereas it switches to RANS in the boundary layer. LES could also be applied if sufficiently refined meshes and associated computational time are allowed but that is not the case for the current work.

3.2. Turbulence generation in CFD

Another key parameter in both experiments and simulations (CFD) is the generation of the inflow turbulence. Before presenting several methods to generate turbulence within simulations, it is first key to establish the methods by which turbulence is usually generated within experiments. These methods can then be used to define criteria for simulation-generated turbulence.

3.2.1. Turbulence generation in experiments

Within experiments, turbulence is often generated by placing a passive grid in the contraction of a wind tunnel as depicted in Figure 3.2a. The flow over each bar induces a turbulent wake behind the bar. These wakes then interact with one another to create a turbulent field. Roach [54] was one of the first to present guidelines on using grids to generate inflow turbulence. It was stated that the turbulence

parameters of nearly isotropic turbulence by passive grids mainly depend on the geometric properties of the grid, such as those displayed in Figure 3.2b. Additionally, it was proven that scaling laws exist, which can define the decay of the turbulence intensity in the wake of the grid. Care must be taken to place the grid sufficiently upstream to ensure that the turbulence decay has levelled out, indicating homogenous turbulence. More recent works confirmed these scaling laws and the ability of passive and multi-scale grids to generate isotropic turbulence downstream of the grid [55]–[57]. The simplicity and robust inflow of the grid-generated turbulence make it a suitable method for experimental turbulence generation.

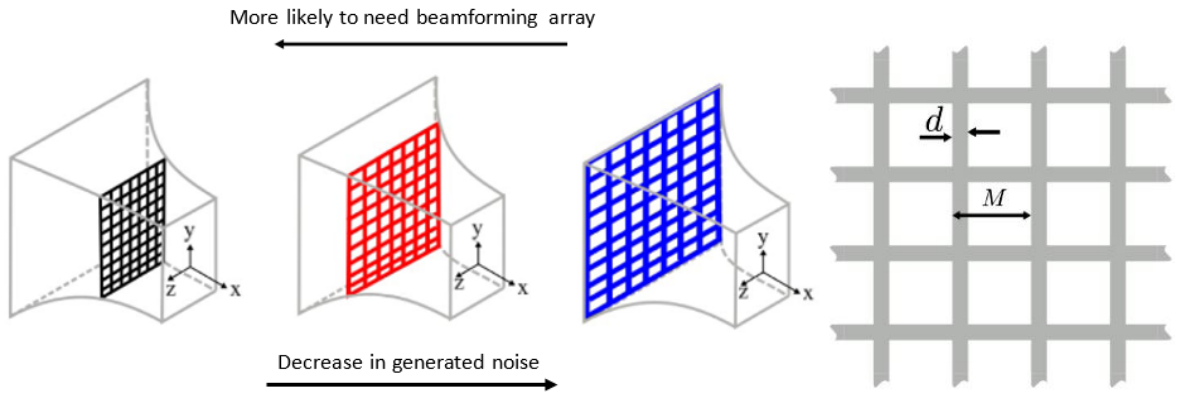

(a) Generated noise and need for beamforming arrays for different grid placements. Turbulence is generated by a flow in the positive x-direction.

(b) Geometric definitions of the grid. Turbulence is generated by a flow perpendicular to the plane.

Figure 3.2: Geometrics and placement effect of passive turbulence grids. Both figures are adapted from Bowen et al. [58].

Bowen et al. [58] also confirmed this and additionally performed research into the placement of the grid within the contraction of the wind tunnel, see Figure 3.2a. They highlighted one key downside to grid-generated turbulence: the self-noise production. The grid itself also produces noise based on the geometric properties but, more importantly, based on the placement within the contraction of the tunnel. They have proven that grids with a high contraction ratio between the grid and the nozzle outlet area produce the least self-noise with a compromise on the isotropy of the turbulence. The difference between self-noise can be as much as fifteen decibels when comparing the black and blue cases from Figure 3.2a. Additionally, they have proven that the highest self-noise sound production from the grid can be almost as big as the noise generated by a NACA00012 airfoil. This makes it hard to distinguish between grid self-noise, airfoil-radiated noise and possibly background noise from the wind tunnel as well. CFD simulations are not sensitive to background noise, showing their added value to experiments.

One solution to distinguish the airfoil radiated noise from the grid self-noise is by applying an acoustic beamforming array. This was applied in works by Dos Santos et al. [26] and Geyer et al. [59], who have both shown that accurate measurements of leading edge noise are possible while excluding other noise sources, such as the grid self-noise, background noise but also trailing edge noise. An additional uncertainty (one decibel according to Dos Santos et al. [26]) is added to the analysis. Applying an acoustic beamforming array is thus a suitable method, but it is not preferred due to the many complex steps required for the process and the added uncertainty.

An alternative to grid-generated turbulence, which produces less sound, is turbulence generated by a rod in the flow. The grid of Figure 3.2b is replaced by a rod (cylinder) with its longitudinal axis in the spanwise direction as depicted in Figure 3.3. This method works similarly to grid-generated turbulence, but now there is only one ‘bar’ with which the uniform inflow can interact. Several key differences with grid-generated turbulence, however, occur:

1. The turbulence generated in the wake of the rod is due to the shedding of vortices named the Von Kármán vortex street. Disadvantageous to this Von Kármán similarity is that it is highly periodic. Only if the Reynolds number is sufficiently high can true turbulence with a high shedding frequency be created [11, p. 124–126],[35, p.39]. This problem is not present for grid-generated turbulence since the turbulence mixes much more in the wake of the grid.

2. On the other hand, there is also an advantage to this periodicity. The self-noise from the rod is only centred around this shedding frequency, whereas grid self-noise is present over the whole frequency range [60]. The problem of self-noise is thus not fully removed, but this method makes direct noise measurements much easier when compared to grid-generated turbulence.
3. The wake generated by the rod is expanding in the vertical direction [61], i.e. the y-direction in Figure 3.3. Dos Santos et al. [26] reported this problem and stated that placing the rod upstream further ensured the foil was fully in the turbulent wake. This problem is similar to the grid placement for levelling out the turbulence decay to homogeneous turbulence.
4. At last, Figure 3.3 presents a velocity decay in the wake of the cylinder. Both Shih et al. [61] and Liu et al. [62] prove that there is not only a decay of the streamwise velocity in the wake but that there is also an increase of velocity fluctuations for the streamwise and vertical directions compared to grid-generated turbulence. This is a key reason why rod-generated turbulence is not preferred if isotropic turbulence is required since the velocity fluctuations differ per direction. It is, however, preferable if direct noise measurements are required without the need for complex beamforming arrays.

Rod-generated turbulence has been used in recent works to predict airfoil radiated noise by Dos Santos et al. [24], [26]. They have shown viable methods with favourable outcomes regarding acoustic data. As stated, rod-generated turbulence does, however, display anisotropic behaviour. This method is, therefore, not preferred when choosing a turbulence generation mechanism for the simulations.

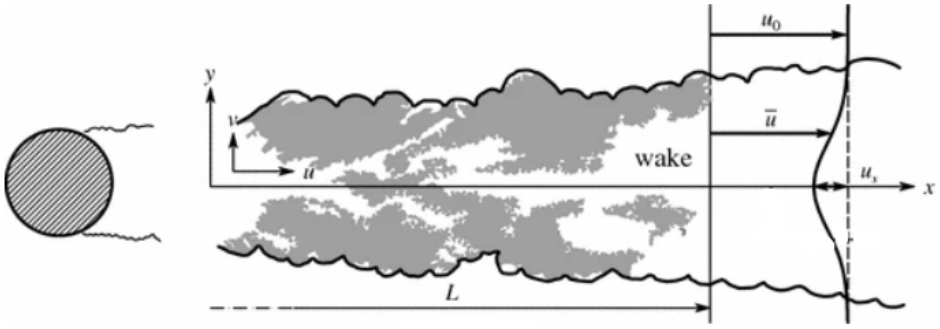

Figure 3.3: Example of a turbulent wake from a cylinder with flow in the positive x-direction. Adapted from Nieuwstadt et al. [35, p. 108].

3.2.2. Requirements for artificial turbulence generation

The previous section is used to set requirements for turbulence generation within CFD. Additional requirements for the turbulence generation from the CFD perspective can also be set. The following is required from the turbulence generator within the simulations. The method should [63]–[65]:

1. be varying on scales down to the set filter scale (both spatially and temporally);
2. be compatible with the Navier-Stokes equations. Meaning that the solver (simulation) must support the turbulence rather than destroy it after it is generated;
3. 'look like actual turbulence' such that it is similar to grid-generated turbulence. Therefore:
    - the turbulence must decay throughout the domain;
    - the turbulence must be divergence-free;
    - the turbulence must be isotropic (after a development length);
    - the eddies must interact in a physical manner, contain energy and possess realistic structures up to the desired scale scale.
4. be compatible with the proposed scale-resolving simulation turbulence models from Section 3.1.2, i.e. IDDES, LES and RANS (the latter if the choice is made for the IDDES framework);
5. be such that the approach is cheap (low computational time);
6. be easy to implement and adjustable for new inlet conditions and desired turbulence properties, i.e. the turbulence intensity and integral length scale.

Requirements 1 and 3 follow directly from the turbulence generated within experiments described in the previous Section 3.2.1. Properties 2, 4, 5 and 6 are requirements from a computational perspective, some of which are needed for the actual turbulence and others for user-friendliness. These requirements can be used to evaluate the different generation methods which will be proposed in the next Section 3.2.3.

3.2.3. Precursor and synthetic turbulence generation

Present turbulence generation methods for CFD, regardless of whether they satisfy the conditions of Section 3.2.2, can be divided into precursor and synthetic methods. Precursor methods use an auxiliary simulation that is either run beforehand or simultaneously with the main simulation. The generated turbulence over a solid boundary on a plane in the auxiliary simulation is introduced at the inlet of the main simulation. Figure 3.4 describes the three concepts associated with this method. Turbulence for the main simulation can either be created in an auxiliary simulation (a), in an auxiliary simulation which rescales its data (b) or in the main simulation for which internal mapping is applied (c). An obvious downside to this method is the computational costs associated with running an auxiliary simulation, as well as possible storage costs if that simulation is run beforehand. The latter will increase substantially if different inflows are needed and even more if turbulence up to the smallest length scales (Kolmogorov) is required. The setup of these simulations also plays an important role in generating the turbulence, where tuning can take a lot of time if the user is not familiar with the turbulence quantities. Auxiliary simulations do not have to be carried out on the same Reynolds number as the main simulation since the turbulence can be scaled, after which it can develop throughout the main computational domain. This is both advantageous and disadvantageous since it increases the application space while requiring increased computational time due to increased domain. Furthermore, the inlet size has to be kept the same between the auxiliary and main simulation, making it hard to generate turbulence for a wide range of (complex) applications. The biggest advantage of this method is that it possesses realistic turbulence characteristics, correlation and energy spectral levels since a genuine simulation of turbulence is run. [63]–[68]

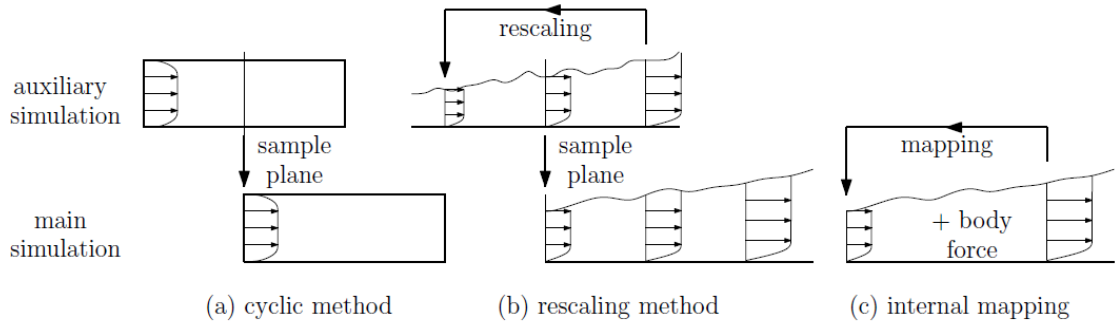

Figure 3.4: Recycling (a), rescaling (b) and internal mapping (c) precursor turbulence generation methods [68].

Synthetic methods, on the other hand, generate turbulence by applying mathematical expressions based on constraints on a plane. This plane can either be on or close to the inlet. These semi-random deformations of the flow field generate turbulence. The simplest method to do so is by applying white noise on the velocity signal at the plane. Although simple, this method is easily destroyed by the solver while also not containing many realistic turbulence characteristics. Other more sophisticated methods exist, such as Fourier techniques, principal orthogonal decomposition analysis, digital filtering methods and eddy methods. The reader is referred to the work by Lloyd [68], who performed an in-depth literature study for the different methods. The main advantage of these methods is the low computational time and storage space since an auxiliary run is not required. Additionally, all of these methods can be applied to a wider range of applications since the input parameters can be tuned based on the domain, inlet size and application. The downside to this method is, however, the need for a development length for the turbulence to acquire realistic turbulence properties. Additionally, one has to have knowledge of the (developed) turbulence characteristics to choose suitable input parameters. Tuning of this method is, however, significantly faster when compared to precursor methods since long simulations can be avoided. [63]–[68]

A summary of the different arguments for precursor and synthetic methods based on different properties is shown in Table 3.1. These arguments will be used in Chapter 4 to define the turbulence generation within the methodology used in this work.

Table 3.1: Performance of precursor and synthetic turbulence generation methods. The numbers in brackets refer to the requirements from Section 3.2.2. The colours indicate poor (red), moderate (orange) and good (green) performance.

Property	Precursor	Synthetic
Compatible with solver	Yes (2,4)	Yes, apart from white noise (2,4)
Turbulence realism	Realistic (1,3)	Less realistic, needs to develop (1,3)
Divergence free	Yes (3)	Depends on method (3)
Tuning	Time consuming (6)	Straightforward (6)
CPU cost	High (5)	Low (5)
Memory cost	High (5)	None (5)
Location of generator	At the inlet (6)	Anywhere (6)

3.3. Acoustic analogies for leading edge radiated noise

Within this work, so-called acoustic analogies are used to predict the far-field sound. These acoustic analogies assume that the generation and radiation of the sound are two separate phenomena for which separate calculations can be made. Acoustic analogies are preferred over directly computing (resolving) the sound waves due to the high associated costs. Resolving the acoustic waves requires much finer and bigger meshes than necessary for the turbulence modelling. According to Peng et al. [52, p. 65–66] resolution of sound waves can require a mesh that is nine times finer than required for the turbulence dependent on the direction of radiation. Since acoustic wave propagation outside of the noise generation part within the main flow is well understood and modelled by linear wave equations, it is wasteful to extend this much finer mesh to far-field receivers [69], [70]. Within this work, two acoustic analogies will be used: the theory by Amiet as explained in Section 3.3.1 and the Ffowcs Williams–Hawkings theory explained in Section 3.3.2.

3.3.1. Amiet

Amiet proposed a framework to predict the far-field acoustic power spectral density caused by the leading edge of an airfoil in a subsonic uniform flow as a function of the turbulence characteristics. For an in-depth derivation of the equations, the reader is referred to the original work by Amiet [17] and the work by De Santana [71]. According to Amiet, the one-sided power spectral density of pressure fluctuations (and hence sound) for an observer at $(x_o, y_o, z_o = 0)$ for a flat plate in uniform inflow as a function of frequency is:

$$G_{pp}(x_o, y_o, z_o = 0, f) = 4\pi^2 \left(\frac{2\pi f y_o \rho (c/2)}{c_\infty \sigma^2} \right) U_{inf} \frac{d}{2} |\mathcal{L}(x_o, k_x)|^2 \Phi_{vv}^{vK}(k_x). \tag{3.1}$$

Here c_∞ is the speed of sound, $\sigma^2 = x_0^2 + (1 - M^2)(y_0^2 + z_0^2)$ a measure of the position of the observer, $k_x = 2\pi f / U_{inf}$ the streamwise wavenumber and $\mathcal{L}$ the aeroacoustic transfer function. The latter is derived in more detail by De Santana [71, p. 154–168]. Amiet makes several assumptions to derive this far-field spectrum:

1. The observer is stationary and directly above the foil at mid-chord and midspan ($x_0 = 0.5 \cdot c$ and $z_0 = 0$);
2. The foil is modelled as a flat plate of infinitely large span ($d \to \infty$) and negligible thickness ($t \to 0$);
3. The incoming gusts are modelled as two-dimensional upwash velocity gusts;
4. Turbulence is modelled by assuming the isotropic Von Kármán spectrum $\Phi_{vv}^{vK}(k_x)$. Additionally, the turbulence is assumed to be frozen.

Assumption one merely limits the application of Amiet to one specific stationary observer. It is expected that assumption two also confirms this due to the removal of effects induced by the realistic geometry of a foil. Additionally, these induced effects are not considered while modelling the turbulence spectrum by assumptions three and four. Assumption three is likely to induce a bias towards low-frequency large

gusts, whereas the far-field noise due to high-frequency smaller turbulence is most likely less accurately predicted. This is supported by assumption four, which states that the turbulence spectrum is modelled based on the Von Kármán (vK) spectrum such that

$$\Phi_{vv}^{vK} = \frac{4}{9\pi}\frac{u_{rms}^2}{k_e^2}\frac{(k_x/k_e)^2}{[1+(k_x/k_e)^2]^{7/3}}, \tag{3.2}$$

which is known for being less accurate at higher frequencies. Here $k_e = \frac{\sqrt{\pi}}{\Lambda_f}\frac{\Gamma(5/6)}{\Gamma(1/3)}$ is the wavenumber of the largest eddies and $k_x = 2\pi f/U_{inf}$ the streamwise wavenumber. Besides the transverse velocity spectrum, Von Kármán is also well known for its one-dimensional streamwise velocity spectrum Φ_{uu}^{vK}, which states that

$$\Phi_{uu}^{vK} = \frac{2}{\sqrt{\pi}}\frac{\Gamma(5/6)}{\Gamma(1/3)}\frac{u_{rms}^2}{k_e}\left[1+\left(\frac{k_x}{k_e}\right)^2\right]^{-5/6}. \tag{3.3}$$

It can be used as a reference to validate the numerical results to check for isotropic turbulence. From Equation 3.3 it also becomes clear that for high frequencies the Von Kármán spectrum follows a -5/3 power law in k_x (and thus in f). This power law and Equation 3.3 will be used later on in this work.

Dos Santos et al. [26] and Santana et al. [72] both try to improve the high-frequency prediction by implementing a turbulence model that is more accurate being based on the Rapid Distortion Theory (RDT). Additionally, they both improve the RDT and vK spectra by taking turbulence parameters in the distorted region close to the leading edge rather than in the mean flow at infinity or from the inflow conditions. Both show improved results (for higher frequencies) by adapting the RDT with distorted turbulence quantities, thereby improving the downsides of assumptions two to four. Although of lesser importance for this work, since the scaling of Amiet will be used, it is useful to see recent advances in the work of Amiet showing its usefulness to current engineering problems. The latter part of assumption four, the frozen turbulence, merely states that the generated turbulence (either by grid or rod) should have decayed towards a steady state. In short, assumption four requires the turbulence to be homogenous and isotropic.

It should become clear from the analysis above that, although quick since little computational time is needed, Amiet is heavily dependent on the chosen input parameters and spectra. Additionally, it lacks the interaction of the turbulence with the foil, making it less accurate for acoustic receivers other than the intended one at midspan and mid-chord. A more sophisticated approach is desired to more accurately predict the far-field noise based on the inflow and interactions with the foil without having to resolve the sound waves. In the next section, such an approach will be introduced.

3.3.2. Ffowcs Williams-Hawkings

A more sophisticated approach, without the need to resolve sound waves, is proposed by Ffowcs Williams-Hawkings (FW-H). The reader is referred to the original work [73] and the works by Glegg et al. [70] for a detailed derivation of the framework. The FW-H framework assumes a surface close to or on the body for which it propagates the pressure fluctuations to arbitrary receiver locations. These receiver locations can be outside of the computational domain, signifying the usefulness of FW-H when compared to directly resolving the sound waves and to experimental measurements, which are often only possible above the foil. The acoustic analogy from FW-H can be written as the sum of six terms. Five of which are defined on the surface and one accounting for the volume term outside of the surface. The far-field radiated pressure (and hence noise) p' for an acoustic receiver at any arbitrary location $\mathbf{r} = (x_o, y_o, z_o)$ then becomes [49]:

$$\begin{aligned} 4\pi p'(\boldsymbol{r},t)H(f) = &\underbrace{\int_S \frac{\rho\dot{u}_n}{|\mathbf{r}|}\bigg|_\tau dS(\boldsymbol{y})}_{\text{monopole}} + \underbrace{\int_S \frac{p\hat{\boldsymbol{n}}\cdot\hat{\boldsymbol{r}}}{|\mathbf{r}|^2}\bigg|_\tau dS(\boldsymbol{y})}_{\text{near-field dipole}} + \underbrace{\int_S \frac{\rho u_n u_r}{|\mathbf{r}|^2}\bigg|_\tau dS(\boldsymbol{y})}_{\text{near-field non-linear}} + \underbrace{\int_S \frac{\dot{p}\hat{\boldsymbol{n}}\cdot\hat{\boldsymbol{r}}}{c_0|\mathbf{r}|}\bigg|_\tau dS(\boldsymbol{y})}_{\text{far-field dipole}} \\ &+ \underbrace{\int_S \frac{\rho\,(u_n u_r)}{c_0|\mathbf{r}|}\bigg|_\tau dS(\boldsymbol{y})}_{\text{far-field non-linear}} + \underbrace{p'_{\mathrm{Q}}(\mathbf{x},t)}_{\text{Ouadrupole volume integral}}. \end{aligned} \tag{3.4}$$

Here $H(f)$ is the Heaveside function for the FW-H surface defined by f, u_n the velocity in the surface normal direction, u_r the velocity in the sound radiation/receiver direction, **y** the location of the generated fluctuations on surface f, $\hat{\mathbf{n}}$ the surface normal vector and $\hat{\mathbf{r}}$ the normal vector in the direction of the acoustic receiver. Integration for the surface-dependent terms is performed over the surface as denoted by $\int_S [...] dS$. Each term is evaluated at the retarded time τ. This signifies that, although small, there is a difference between the generation moment of the sound and perception of it. Equation 3.4 is the full representation for the FW-H formulation. The actual formulation depends on the chosen surface type, see Figure 3.5. Note that these are merely examples of surfaces that can be chosen. Many sizes and shapes are possible. In general, one has to choose between a porous or solid data surface:

1. A porous data surface (PDS) encompasses the solid body and a part of the flow around it. The advantage of this method is that it also considers pressure fluctuations in the flow that can be regarded as noise sources. A clear example is the shedding of vortices from the (blunt) trailing edge of an airfoil as described in Section 2.1. The associated downside is that hydrodynamic structures (turbulence) may be wrongfully recognised as noise sources. This can happen upstream (close to the ITG) or downstream of the airfoil. Additionally, close to the domain's boundaries, the flow can induce pressure fluctuations by interacting with the boundaries. Both Ribeiro et al. [74] and Lidtke et al. [49] report this problem. The latter removed the up- and downstream end caps of the porous surface to minimise these hydrodynamic-induced noise sources. The PDS also requires a finer mesh within the whole data surface to calculate the pressure fluctuations on the data surface accurately. This leads to increased computational costs if high-frequency resolution is required.
2. A solid data surface (SDS) encompasses only the solid body or a part of it, i.e. the surface overlaps with the solid surface of the simulation. The clear advantage of this method is the removal of the hydrodynamic-induced noise sources. The downside is the loss of rightfully recognised noise sources in the flow. This is acceptable since, for leading edge noise, these are less efficient than the interactions on the foil [30, p. 75–76]. Compared to a porous surface, the solid surface only needs refinement of the mesh near the solid boundary (assuming that the turbulence is well captured upstream of the foil), thereby saving computational costs. For a solid boundary at rest (only movement of the flow), Equation 3.4 reduces to the near-field dipole and far-field dipole terms. The other terms drop out since the normal velocity to the body must be zero for a stationary body, such that $\dot{u}_n = u_n = 0$ m/s. This agrees with the fact that non-linear terms can only be created by the movement of the body in the flow relative to the observer, similar to the well-known Doppler effect The quadrupole volume term is also lost since no volume containing turbulence structures is present.

The FW-H framework has been adapted in many lines of research. Several works regarding non-cavitating applications have shown accurate results based on the FW-H analysis indicating the usefulness of FW-H for the current work [29], [74]–[76]. This concludes the description of the turbulence models, turbulence generation and acoustic analogies. The methodology, where decisions will be made based on the previous analysis, will be given in the next chapter.

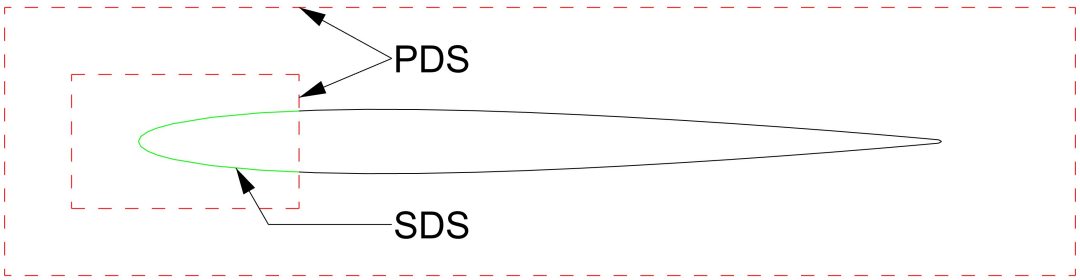

Figure 3.5: Examples of choices for the porous data surface (PDS) and solid data surface (SDS) for the FW-H analysis.

4

Methodology

Within this chapter, the methodology for the simulations and post-processing tools will be presented. Section 4.1 will present the numerical solver and acoustics analogies and accordingly Section 4.2 will describe the turbulence generation method. The integral length scale computation will be discussed in Section 4.3. Section 4.4 will give a detailed description of the domain, mesh and numerical setup used for the simulations. Several post-processing tools used throughout this work will be presented in Section 4.5. Finally, Section 4.6 will present a concise study into the verification of the mesh and the spanwise domain size.

4.1. Fluid flow solver and acoustic analogies

Numerical simulations are performed using the open-usage finite volume code ReFRESCO developed by MARIN (Maritime Research Institute Netherlands) [77]. ReFRESCO is a widely used tool both verified and validated for numerous industry applications [78], [79]. It solves the unsteady incompressible Navier-Stokes and mass continuity equations using a finite-volume and time-implicit framework. ReFRESCO allows the use of both structured and unstructured meshes as well as turbulence and cavitation models. To ensure mass conservation, a pressure-velocity coupling based on the SIMPLE scheme is used, where at every timestep the non-linear system is linearised using Picard's method. Recent works with methodologies comparable to the current show satisfactory results regarding the inflow and radiated noise of a propeller [49] and cylinder [27], both have thoroughly validated the current setup.

A scale-resolving simulation (SRS) framework is adapted for which the biggest length scales are resolved, whereas the effect of the smallest length scales is only modelled. The change between resolving and modelling is determined by the improved delayed detached eddy simulation (IDDES) framework, which employs the $k - \omega$ model, resulting in a switch between LES and RANS based on the turbulent length scale [80], [81]. This method was chosen based on a trade-off between accuracy and computational costs, also explained in more detail in Section 3.1.2. LES is applied in most of the domain, whereas the method switches to RANS in the boundary layer. The ill-resolving of the boundary layer is found acceptable since no boundary layer analysis is conducted and since the acoustics and turbulence parameters are only determined upstream or close to the leading edge of the foil.

Acoustic analogies are used to predict the far-field noise of the foil, both explained in Section 3.3. The numerical code written for the Amiet acoustic analogy is validated with the algorithm used by Dos Santos et al. [26]. Both codes give identical outputs for identical inputs. The outcomes of the Ffowcs Williams-Hawkings (FW-H) acoustic analogy will be validated within this work, but several works with similar methodology have readily shown promising results [28], [29], [49], [52, p.59–76]. A solid data surface will be used to remove spurious disturbances in front of the foil and to reduce computational time. Additionally, the solid surface allows for the separation of leading and trailing edge induced noise by defining it for a part of the foil. The ReFRESCO solver allows for parallel computation of the FW-H equations for specified receiver locations, thereby minimising additional computational time.

4.2. Turbulence generation

A synthetic method is preferred over precursor methods due to the low computational time and the simple tuning for different turbulence intensities. The reduced realism of the turbulence in synthetic methods can be overcome by applying a sufficient development length for the turbulence. Turbulence in the simulations will be generated using the synthetic digital filtering approach as originally proposed by Kim et al. [82]. Based on this work, velocity fluctuations were inserted at the inflow. This caused the solver to try to correct the mass imbalance through the pressure equation since the continuity equation was no longer satisfied. This led to the creation of instabilities and pressure fluctuations, which affected the solution in the whole domain [65]. The work by Jarrin et al. [83] improved this by applying the velocity fluctuations on a defined plane within the flow. Still this method suffered from two problems. First, the velocity fluctuations were still being destroyed by the solver. Second, the build-up of fluctuations at every timestep could mean poorer convergence of the solver. The solution was to apply body forces based on the velocity fluctuations on the flow instead of the velocity fluctuations themselves.

This setup, as implemented in ReFRESCO by Lidtke et al. [27] and Klapwijk et al. [84], uses a Cartesian plane generated at the desired point in the flow (not necessarily the inlet) with its normal vector in the direction of the flow. At each outer loop (timestep), random numbers $r_{m,l,i}$ with zero mean and unit variance are generated on this plane. The indices refer to the m-th and l-th position on the plane for the i-th velocity component. Spatial correlation is ensured using exponential correlation function whereas temporal correlation is assumed by implying

$$\Psi_i(t) = \Psi_i(t-\Delta t) exp\left(-\frac{\pi \Delta t}{2\mathcal{T}}\right) + \psi_i(t)\left[1 - exp\left(-\frac{\pi \Delta t}{2\mathcal{T}}\right)\right]. \tag{4.1}$$

This formulation ensures temporal correlation between the current and previous timestep. Here the integral timescale is calculated from the intended integral length scale and the velocity taken at the initialisation of the generator, such that $\mathcal{T} = \mathcal{L}/\overline{u_i}$. This is similar to the method proposed in Section 2.3. These spatially and temporally correlated numbers are converted to velocity fluctuations u_i' based on input Reynolds stresses and are in turn transformed into body forces by using

$$F_{b,i} = \frac{\rho \overline{u_i}(\overline{u_i} + u_i' - u_i)}{L_{ITG}} \cdot b. \tag{4.2}$$

Here $F_{b,i}$ is the body force in the i-th direction, $\overline{u_i}$ the mean velocity taken at the initialisation of the generator in the i-th direction, u_i' the desired instantaneous velocity fluctuation and u_i the instantaneous velocity. One can recognise the Reynolds decomposition in the numerator of Equation 4.2. In this case if the instantaneous velocity fluctuation (u_i') is readily achieved at that point ($\overline{u_i} - u_i = -u_i'$) the body force term iterates towards zero, thereby improving the convergence behaviour of the solver. L_{ITG} and b indicate the thickness in the flow direction over which the body forces are spread and an amplification factor used to achieve faster convergence to the desired fluctuations. The generated body forces are added to the momentum equation at every non-linear loop. The input Reynolds stresses, amplification factor and thickness were tuned by running empty domain simulations until desired turbulence characteristics and values were achieved.

4.3. Integral length scale computation

As introduced in Section 2.3, several ways exist to compute the integral length scale even for the time correlation. The zero-crossing method proposed by Ribeiro et al. [29] and the integration of best-fit curves will be used within this work. Both methods rely on calculating the integral length scale based on Equation 2.7. Two key differences between the methods can be noted. The zero-crossing method takes the maximum integration time as the first time lag where the autocorrelation $\rho(\tau)$ reaches zero. The fitting method, on the other hand, takes the full time lag. Second, the zero-crossing method integrates the correlation as proposed in Equation 2.8. The fitting method, however, integrates the best-fit curve over the whole time lag. That best-fit curve is defined based on the one-term exponential decay function with the addition of a tangent hyperbolic to capture the initial behaviour of the correlation better. This combination of functions, together with their coefficients, was determined based on an analysis of the errors for the different options. The final curve for fitting the correlation was determined as

$$\rho_{fit}(\tau) = exp\left(-a \cdot \tau^{0.4}\right) \cdot \left((1 - tanh(b \cdot \tau^{0.6})\right). \tag{4.3}$$

Here, a and b are fitting coefficients that are determined by the curve-fit procedure from the scipy.optimize library in Python. The proposed best-fit curve satisfies all of the requirements set in Equation 2.9. Both procedures are validated by applying them to experimental data. Experimental data is provided by Dos Santos et al. [85], who performed velocity measurements at different streamwise positions by hot-wire anemometry. Evaluation of the data is performed at one position in the domain. Similar durations of the time signal to that of the simulation are chosen to reflect the shorter time signals often found in numerical data. The results for the zero-crossing and fitting method for the experimental data can be seen in Figure 4.1a. Two observations can be made. First, due to the fluctuations in the length scale of both methods, it is hard to talk about 'the' integral length scale. To make comparison easier, the means of both methods are also displayed in the legend of the figures. Second, quite often, the fitting method overestimates the length scale. This is due to the fluctuating behaviour of the autocorrelation as previously introduced. To partially solve this problem, the fitting procedure was altered to not fit up to the zero-crossing but up to the time lag where $\rho(\tau) = 0.2$. These improved results can be seen in Figure 4.1b.

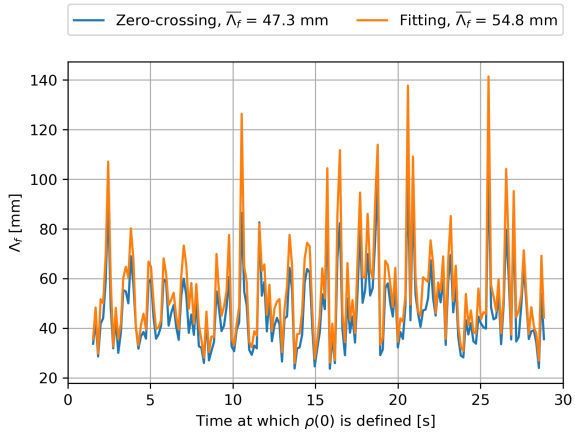

(a) Autocorrelation fitting performed until $\rho(\tau) = 0$.

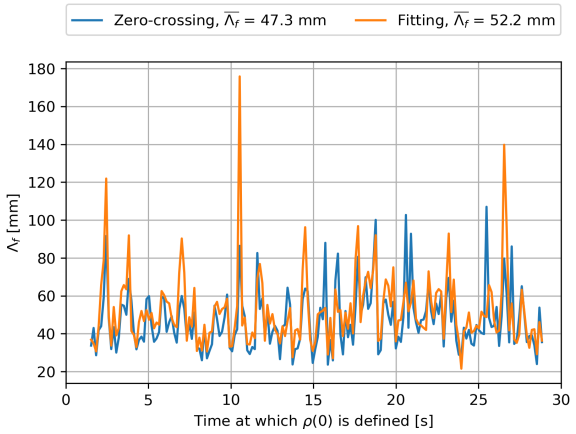

(b) Autocorrelation fitting performed until $\rho(\tau) = 0.2$.

Figure 4.1: Experimental zero-crossing and fitting method for the integral length scale calculation. Fitting the autocorrelation is performed until zero (a) and 0.2 (b). The mean value of the integral length scale for both methods is displayed in the legend.

The partial fit shows more accurate results also reflected by the mean value. As a reference, the integral length scale as reported in Dos Santos et al. [85] is 49.6 mm. The partial fitting method overestimates the integral length scale by 5.8 %, while the full fitting procedure overestimates it by 10.5 %, showing a significant improvement. The zero-crossing method is similar for both figures, underestimating the integral length scale by 4.9 %. This is likely due to the limited duration of the autocorrelation taken, which in the experiments could be as much as one hundred times longer.

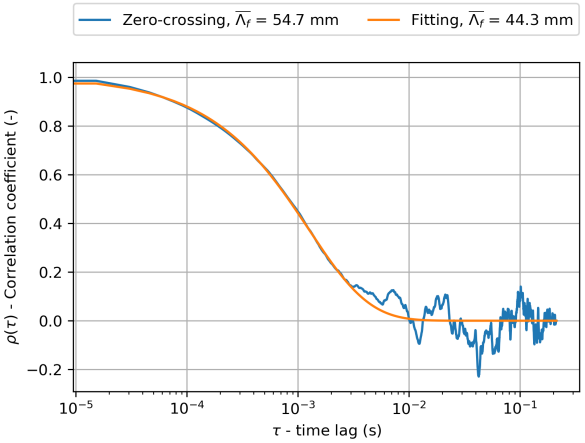

Figure 4.2: Experimental autocorrelation and fitting of the autocorrelation until $\rho(\tau) = 0.2$. The returned integral length scale of both methods is displayed in the legend.

To verify that the fitting procedure works, it is key to visualise a fit. A fit based on the partial fitting procedure can be seen in Figure 4.2. Excellent overlap between both methods is found for $10^{-5} < \tau < 3 \cdot 10^{-3}$ s. From $\tau \approx 3 \cdot 10^{-3}$ s the regular autocorrelation (zero-crossing method) fluctuates. The fitting method removes this by smoothly decaying to zero. The differences between the methods is clearly depicted in the integral length scales, as shown in the legend. The zero-crossing procedure overestimates the length scale of 49.6 mm [85], whereas the fitting method underestimates it by approximately the same amount. It seems that the fitting method is a bit more conservative for the integral length scale. On the other hand, the zero-crossing procedure overestimates it.

4.4. Domain, mesh and numerical setup

A side view of the numerical setup showing the domain, inflow turbulence generator (ITG) position, boundary conditions and acoustic probes can be seen in Figure 4.3. The coordinate system with x in the flow, y in the vertical and z in the spanwise directions has its origin midspan at the (intended) leading edge of the foil. The boundary conditions of the sides of the tunnels are periodic to prevent interactions between them within the domain as much as possible. These boundary conditions are at $-0.33c$ and $0.33c$, making the total width $0.67c = 200$ mm. This size was chosen to minimize computational time while allowing the turbulence to develop naturally. The current setup is able to capture at least eight times the length scale in the spanwise direction, which should suffice to overcome strong interactions with the boundaries. Additionally, RANS is applied in the boundary layer which does not allow for generation of (bigger) structures on the surface of the foil. Pressure and acoustic data on the surface of the foil should, therefore, also not be influenced by the chosen span size. This will, however, be investigated in Section 4.6.2. Dampening boxes (DB) are placed upstream of the ITG and downstream of the foil to prevent reflections from the inlet and outlet. Inflow turbulence is generated not over the full height of the domain to prevent strong interactions with the top and bottom boundary conditions and to save computational time. The acoustic receivers are placed at 1.5 m in a circle around the airfoil at every two degrees with the array's centre at midspan and half of the chord, i.e. $(x, y, z) = (0.5c, 0, 0)$. The angle defining the placement of the probes is θ with $\theta = 0$ degrees in the direction of the trailing edge.

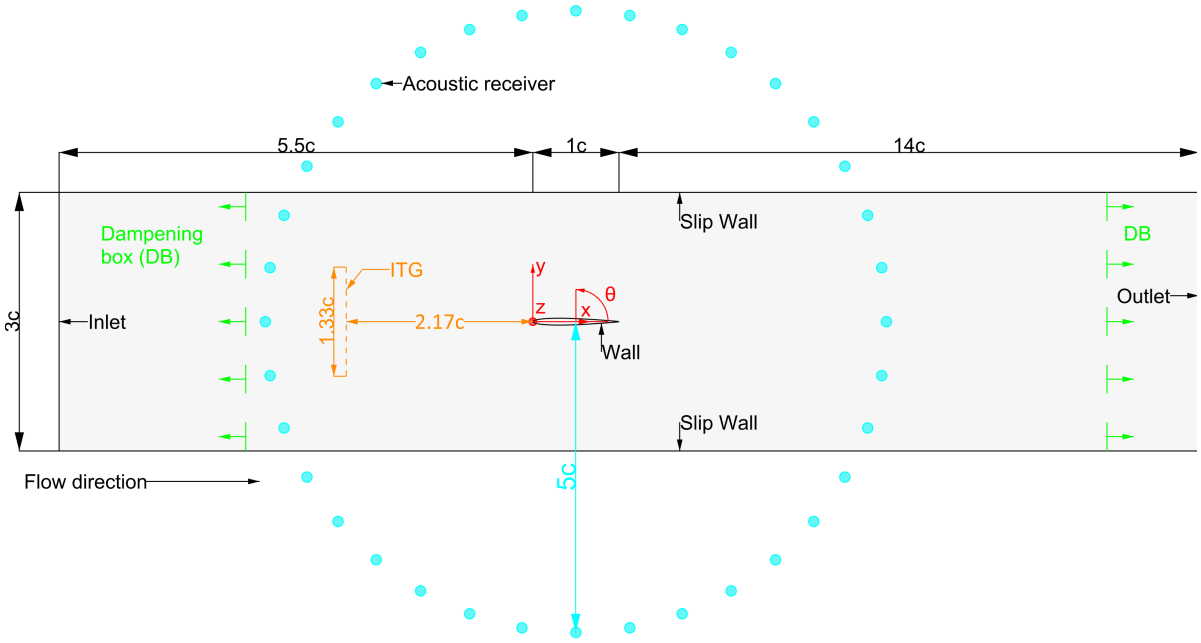

Figure 4.3: Side view of the numerical setup. All distances are visualised based on the chord of the NACA0008 airfoil ($c = 300$ mm). The domain extends fourteen chord lengths behind the trailing edge of the foil. The acoustic receivers are shown every ten degrees while they are placed every two degrees in the simulation.

The computational mesh was kept constant throughout the different simulations. Mesh coarsening was adapted in front of the ITG and behind the foil. Mesh refinement was applied around the foil, and additional refinement was applied at both the leading and trailing edges to accurately capture high frequency pressure and acoustic data. The choices resulted in a mesh with approximately 15.6 million cells for the no-foil simulations and 9.3 million cells for the simulations with the foil. A render of the mesh with the foil can be seen in Figure 4.4. A similar mesh was used for the no-foil turbulence tuning simulations.

All simulations were run with a fixed time step of $\Delta t = 3.55 \times 10^{-5}$ s, or based on the inflow velocity and chord of the foil $\Delta t^* = 3 \times 10^{-3}$. Simulations with a bigger timestep showed unsatisfactory results regarding the resolution of the turbulence and the Courant number. The chosen fixed time step resulted in a maximum Courant number below fifteen for the highest turbulence intensity case. This was deemed acceptable since such high values only occurred sporadically near the foil. Simulations of both the empty domain (without the foil) and with the foil showed the same order of convergence for the L_2 and L_∞ norms for all variables. For all simulations convergence of the L_2 norm of at least order 10^{-5} were obtained. The L_∞ norm performed slightly worse for all cases being at least of order 10^{-4}. These were deemed acceptable for the analysis performed in this work.

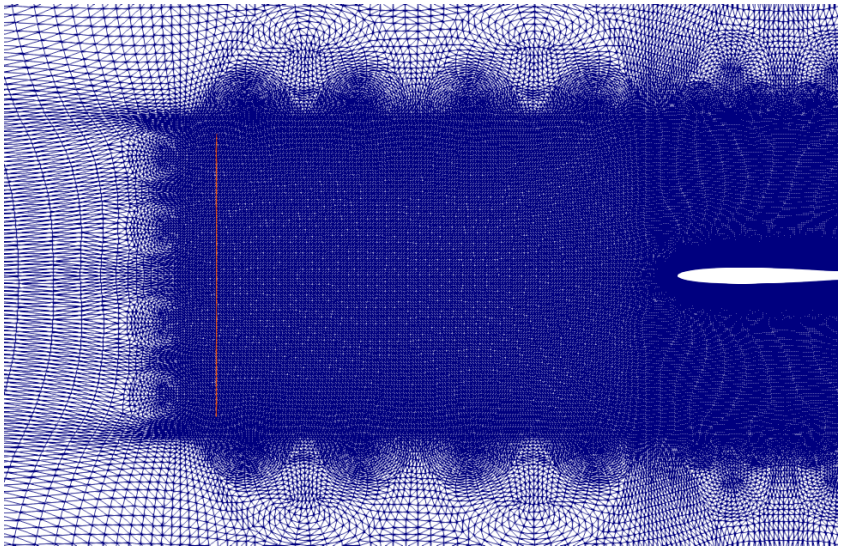

Figure 4.4: Rendering of the mesh with the foil. The slice is taken at midspan of the foil. The orange line depicts the ITG.

Figure 4.5 shows a visualisation of a simulation with the foil present. The empty flow domain, without the foil, is similar to the one depicted in Figure 4.5 apart from the foil. The spanwise vorticity is made nondimensional by the chord and the set inflow velocity. Turbulence is generated on a plane with its normal in the flow direction, visualised directly above the definition of the coordinate system. One can also observe the natural decay of the turbulence throughout the domain, which is required from an experimental point of view; see Section 3.2.2. This also highlights the need to simulate the empty domain to accurately tune the turbulence parameters to desired values at the (intended) leading edge without being influenced by the foil.

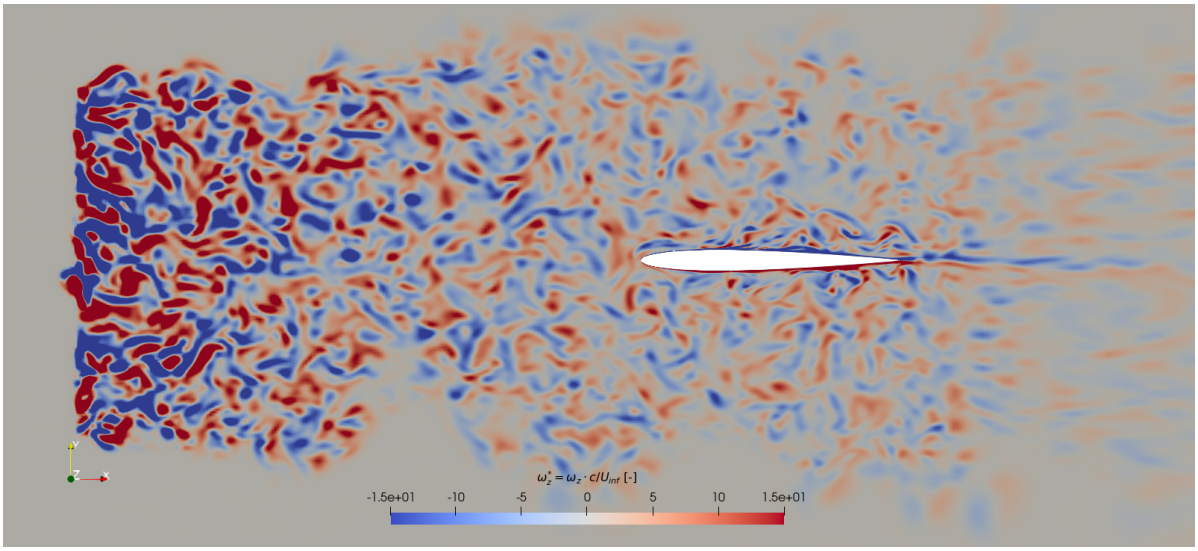

Figure 4.5: Instantaneous spanwise vorticity as a visualisation of the numerical cases. The slice is taken at midspan of the foil.

4.5. Post-processing tools

Within this work, several typical post-processing tools are used. How these are used will be explained in the following sections.

4.5.1. Transient scanning analysis

To remove start-up effects from the simulations, a transient scanning analysis (TSA) will be adapted based on the work of Brouwer et al. [86] implemented as function in Python. The TSA is strong in identifying possible start-up and end effects which do not stand out in a visual inspection of the signal. Assuming that the random standard uncertainty of the mean value at the first-order replication level is equal to the standard deviation of the mean ($u_1 = s_m$), the TSA calculates the cumulative u_1 with

$$u_1 = \sqrt{\frac{1}{T}\int_0^T \left(1 - \frac{\tau}{T}\right) C_{xx,biased}(\tau) d\tau}, \tag{4.4}$$

where $C_{xx,biased}$ is a biased estimator for the autocovariance. The biased autocovariance increases the stability of the calculation by forcing the outcome of Equation 4.4 to be positive. The biased autocovariance follows from an estimate of the unbiased autocovariance such that

$$C_{xx,biased}(\tau) = \left(1 - \frac{|\tau|}{T}\right) \cdot C_{xx}(\tau). \tag{4.5}$$

The unbiased autocovariance is defined from the Fourier transform of the one-sided autospectral density function $S_{xx}(f)$, better known as the Wiener-Khinchine relation as explained in more detail in Brouwer et al. [87]. A signal is said to be stationary if the trend of the $u_1 - T$ plot on a log-log scale follows a slope of minus one. Any other slope should be deemed non-stationary. Brouwer et al. [86] show an application of the TSA removing the start-up effect of a signal.

4.5.2. Spectral analysis

Spectral analysis of a signal gives insight into a parameter at one point in the flow as a function of frequency. Spectral analysis within this work are performed by the Scipy Welch algorithm in Python [88]. A 50 % overlap was used between each of the segments in which the traces were subdivided, resulting in the power spectral density (PSD) of the signal. For clarity, these evaluations are smoothed by using a one-third octave bandwidth top hat filter. To do so, frequency bands are established with centre frequency f_c having a separation of one-third octave ($2^{1/3}$) with 1 kHz defined as the baseline centre frequency. The original PSD is integrated within each frequency band, after which it is corrected to the desired narrowband spectrum. Within this work, this method of a one-third octave bandwidth top hat filter is referred to as the mean decidecade band power density of the signal. Both the PSD and mean decidecade band power density are often depicted on a decibel (dB) scale using reference values for the velocity and pressure, in this work set to $u_{ref} = 1$ m/s and $p_{ref} = 2 \cdot 10^{-5}$ Pa.

Spectra can be integrated to retrieve values represented by the entire time signal. An example is the integration of the spectrum of the wall pressure fluctuations, which results in the RMS of the wall pressure. Integration bounds will always be mentioned in the text, and integration will only be performed for mean decidecade band power density spectra to avoid integration of highly oscillatory signals.

4.5.3. Acoustic correction for span

To validate the acoustic results, the numerical data will be compared to experimental data. Both data sets are for the NACA0008 foil with similar dimensions apart from the span. To make a fair comparison between the data sets, a correction for the radiated noise from the foil based on the span has to be applied. Corrections are often based on the pressure magnitude squared coherence (γ^2) in the spanwise direction. Giret et al. [89] propose a correction based on the work of Kato et al. [90], who assume that the coherence function has the shape of a boxcar function, such that

$$SPL_\gamma(f) = \begin{cases} SPL_{\text{sim}}(f) + 10\log_{10}\frac{d_{\text{exp}}}{d_{\text{sim}}}, & L_\gamma(f) < d_{\text{sim}} \\ SPL_{\text{sim}}(f) + 20\log_{10}\frac{L_\gamma(f)}{L_{\text{sim}}} + 10\log_{10}\frac{d_{\text{exp}}}{L_\gamma(f)}, & d_{\text{sim}} < L_\gamma(f) < L_{\text{exp}} \\ SPL_{\text{sim}}(f) + 20\log_{10}\frac{d_{\text{exp}}}{d_{\text{sim}}} & d_{\text{exp}} < L_\gamma(f). \end{cases} \tag{4.6}$$

Here, the corrected value $SPL_\gamma(f)$ as a function of the frequency is based on the outcome of the FW-H prediction $SPL_{sim}(f)$ plus an additional term. The additional term is determined by comparing the span of the experiment d_{exp} and simulation d_{sim} to the coherence length $L_\gamma(f)$. Simulations are preferably made in such that the coherence length, for the frequencies of interest, will always be smaller than the span of the foil, thereby forcing the correction to the incoherent version (first line) of Equation 4.6.

Several methods exist to calculate the coherence length. Kato et al. [90] proposed to take the coherence length as the spanwise spacing where the root of the magnitude squared coherence function $\sqrt{\gamma^2}$ drops to the critical value of one half. This method is crude and will result in a coherence length smaller than the span of the foil. It is also desired to include the coherence for values smaller than the proposed critical value of one half. This method will therefore not be used in this work.

The second method is based on Von Kármán [68, p. 35], estimating the coherence length as

$$L_\gamma(f) = \frac{8\Lambda_f}{3}\left[\frac{\Gamma(1/3)}{\Gamma(5/6)}\right]^2 \frac{(k_x/k_e)^2}{(3+8(k_x/k_e)^2)\sqrt{1+(k_x/k_e)^2}}. \tag{4.7}$$

Downsides to this method are the assumption by Von Kármán that the turbulence must be isotropic and the dependence on the integral length scale. The latter is more problematic since it requires an exact value of the integral length scale, which (as will become clear later on) is hard to predict accurately. This method will be used but it will become clear that this is a very conservative estimate.

The third and most promising method is also based on $\sqrt{\gamma^2}$. The coherence length is computed as

$$L_\gamma(f) = \int_0^d \sqrt{\gamma^2(f,\Delta d)}d\Delta d, \tag{4.8}$$

where the coherence is calculated between points spaced by Δd with the reference at midspan [26]. This method accounts for the development of the coherence below the one half critical value.

In all of the above calculations, the magnitude squared coherence is calculated by the method proposed in Glegg et al. [91] such that

$$\gamma^2_{0,i}(f,\Delta d) = \frac{|\phi_{pp}(0,i)|^2}{\phi_{pp}(0,0)\phi_{pp}(i,i)}. \tag{4.9}$$

Here $\phi_{pp}(0,0)$ and $\phi_{pp}(i,i)$ represent the PSD of the pressure fluctuations at the midspan reference location and location i, calculated as explained in Section 4.5.2. The cross-spectrum $\phi_{pp}(0,i)$ is calculated by the Scipy signal csd command in Python, using the Welch algorithm as introduced before.

4.5.4. Statistical uncertainty estimates

Within this work, two types of uncertainty estimates are performed. The first uncertainty estimate is a direct result of the TSA from Section 4.5.1. Equation 4.4 readily calculated the standard random uncertainty of the mean. For a 95 % confidence level, this value can be multiplied by the coverage factor of 1.96 to get the expanded random uncertainty of a signal [86], such that

$$U_{95,m} = k_{\%} \cdot u_1 = 1.96 \cdot u_1. \tag{4.10}$$

This expanded random uncertainty is not a measure of the errors induced by the simulation but merely a measure of the uncertainty of the mean with respect to the signal (after applying the TSA).

The second uncertainty estimate is made for the spectral analysis as introduced in Section 4.5.2. The uncertainty, assuming a 50 % overlap and $k_{\%} = 1.96$, can be calculated in decibels as

$$U_{95,dB} = 10log_{10}\left(1 \pm \frac{1.96}{\sqrt{2BT}}\right), \tag{4.11}$$

with B the spectrum bandwidth in Hz and T the length of the signal in s [49]. The actual uncertainty is the average of the lower and upper bounds that are returned by this method. If the lower bound calculation is not possible when the log becomes negative, the upper bound is taken as the total uncertainty. Similar to the expanded uncertainty of the mean, this analysis does not say anything about the errors of the simulations. It merely gives the uncertainty induced by calculating the PSD from a finite signal.

Uncertainty estimates for the numerical simulations, such as round-off, discretization and iterative uncertainties, have not been made in this work [92]. Lidtke et al. [49] commented on this by noting that the total uncertainty is the root sum square of all uncertainties. Similar to their work, the uncertainty proposed in Equation 4.11 is in the order of decibels, meaning that other uncertainties must be of the order of 100 % to become dominant. It is, therefore, assumed that the statistical uncertainty from Equation 4.11 is dominant and that quantification of other uncertainties is unnecessary.

4.6. Verification of mesh resolution and spanwise domain size

Two studies have been performed to verify the choice for the mesh refinement in Section 4.6.1 and the choice of the spanwise domain size in Section 4.6.2.

4.6.1. Mesh resolution

A concise mesh resolution study was conducted to show the effect(s) of the mesh resolution on the numerical results, if present. Table 4.1 shows the mesh used within this work (medium), as well as a coarser and finer mesh. Wall-normalised first cell sizes were calculated from the wall shear stress τ_w, such that $y^+ = \frac{y_1 \cdot \sqrt{\tau_w / \rho}}{\nu}$. Table 4.1 shows both the maximum value found for each case as well as the average and the standard deviation around the average.

A clear link between the maximum y^+ value and the mesh refinement can be observed. This link is, however, not that obvious in the average value of y^+ over the foil. This is explained by the sporadic higher values of y^+ only found near the leading edge, see Figure 4.6. The maximum value found near the leading edge has little to no influence on the average value of y^+ taken over the whole foil. This is supported by the small standard deviation around the mean, as shown in Table 4.1. A more elaborate mesh resolution study should also entail bigger refinements of the (first) cells near the boundary of the foil. However, since RANS is used in the boundary layer, it is of lesser importance to investigate it since no turbulent scales will be resolved. It is, however, key to verify that the y^+ values for the chosen mesh are sufficiently small. Peng et al. [52, p. 59–76] have shown accurate results for $y^+ \leq 1.5$ while Lidtke et al. [27] place the boundary for accurate results slightly lower with $y^+ \leq 1$. Note that the latter used partially averaged Navier-Stokes (PANS) equations for which they state that normalised first cell sizes can be bigger (than one) since only a part of the turbulence is resolved. This aligns with the previous statement that RANS resolves none of the turbulence, thereby allowing for (even) higher normalised first cell sizes. The slightly higher sporadic values near the leading edge are, therefore, deemed acceptable, indicating that all three meshes suffice based on the y^+ values.

Table 4.1: Parameters of the three numerical mesh refinement study cases.

Parameter	Symbol	Case 1	Case 2	Case 3
Label figures	N.A.	Coarse	Medium	Fine
Cell size in the x-direction	Δx [mm]	4.52	3.39	2.27
Maximum y-plus	y^+_{max} [-]	1.75	1.65	1.56
Average y-plus	y^+_{avg} [-]	0.421	0.419	0.417
Standard deviation y-plus around the average	y^+_{std} [-]	0.011	0.012	0.012

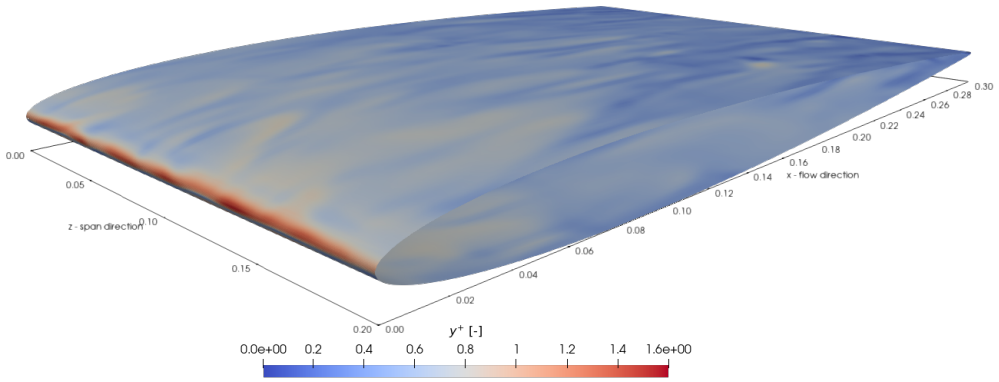

Figure 4.6: Distribution of instantaneous y^+ values over the foil for the numerical medium mesh case.

Note that the only change made between runs is the refinement of the meshes. No other changes are made to the simulations, as well as inputs for the turbulence generation. From Section 4.2, however, it became clear that the body forces are spread over a distance L_{ITG}. Although the distance itself is not changed, the number of cells within that distance will. The way in which the ITG is programmed should compensate for this by increasing or decreasing the body forces when necessary. Small deviations might occur, likely closer to the ITG, although the actual refinement of the mesh is expected to dominate over this. Figure 4.7 shows the mean decidecade band power density of the streamwise velocity component at two different positions in the domain with the foil present. The choice to include the foil in the mesh resolution study was made to also assess the effects of the mesh resolution on pressure data on the surface of the foil. Figure 4.7a shows the mean decidecade band power density close to the ITG, i.e. the ITG is located at $x/c = -2.17$. Results match well for $f < 1500$ Hz. Any results at the lowest frequencies are difficult to assess due to the relatively short signal used for the PSD calculations. The coarsest mesh loses energy more rapidly than the finer cases, which aligns with a coarser mesh's inability to resolve smaller eddies and, thus, higher frequencies. For $f > 1100$ Hz the results, as expected, do not overlap. This effect can be seen more clearly in Figure 4.7b, which shows the PSD closer to the leading edge. At that point, the turbulence has developed through the domain, which means that, according to Section 2.2, energy from the lower frequencies has decayed to higher frequencies. The coarse mesh readily starts to underpredict the energy levels from $f \approx 600$ Hz. The medium and fine meshes, however, overlap reasonably well until $f \approx 1400$ Hz.

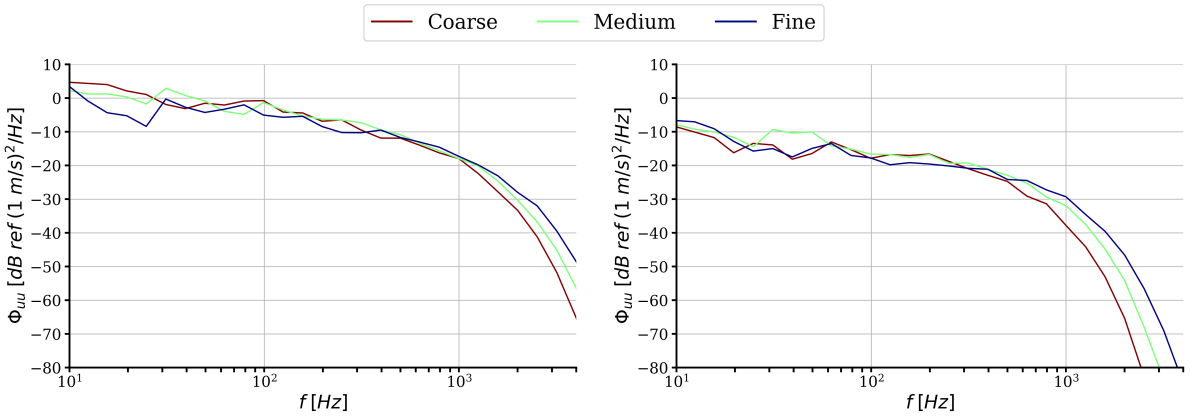

(a) $x/c = -2.$ **(b)** $x/c = -0.2.$

Figure 4.7: Mean decidecade band power density of the streamwise velocity component at two chordwise positions and midspan for the three numerical cases.

Figure 4.8 shows the mean decidecade band power density of the wall pressure at two different positions on the foil surface. These spectra are indicative of the mesh resolution effects close to/on the foil. Both spectra show poor overlap for $f < 200$ Hz. For $f > 200$ Hz, the overlap in Figure 4.8a is much better up to the mesh cut-off frequencies. Comparison of the medium and fine meshes, however, shows a higher mesh cut-off than predicted from the inflow turbulence spectra, indicating that the frequencies from the two types of spectra are not directly linked. This is supported by the unexpected effect that all three meshes overlap well for $f > 200$ Hz in Figure 4.8b. There does not seem to be a distinct mesh cut-off frequency when moving further along the foil chord. This is partially induced by the chosen methodology, which switches to RANS close to the surface of the foil. RANS averages the results over time, thereby making them less dependent on the actual fluctuations and, according to the results, the resolution of the mesh. That can, however, not be the only effect since Figure 4.8a does show a difference while RANS is also applied there. Another effect is that further down the foil, the pressure fluctuations become less dependent on upstream inflow conditions. The coarsest mesh in Figure 4.8b does underpredict the wall pressure for $f > 1000$ Hz, indicating that only the medium and fine mesh are mesh converged for high frequencies. Similar results are also found for the far-field acoustic data compared to the pressure data.

The differences in Figures 4.7 and 4.8 (especially at lower frequencies) are considered acceptable such that the medium mesh used throughout this work is mesh converged.

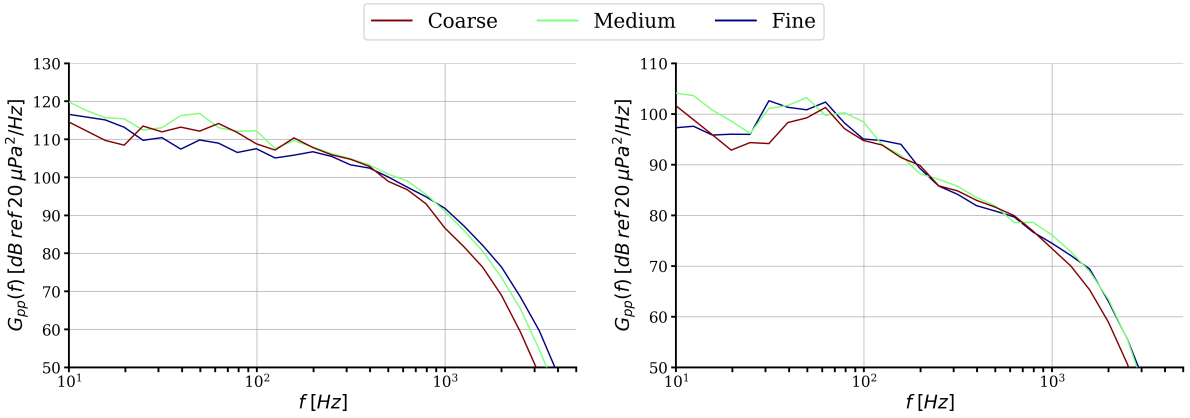

(a) $x/c = 0.$ **(b)** $x/c = 0.5.$

Figure 4.8: Mean decidecade band power density of the wall pressure at two chordwise positions and midspan for the three numerical cases.

4.6.2. Spanwise domain size

A similar study was also conducted to show that the span is sufficient to capture the inflow turbulence, pressure on the foil and far-field acoustics. Effects of the domain size in the spanwise direction are evaluated by running a larger domain. Since RANS is used near the foil, it is expected that differences will only be minor, assuming that the turbulence is well resolved upstream. Two cases are compared:

1. A case with a span of $d = 0.67c = 0.2$ m. This has readily been used in the mesh resolution study called “Medium”. It will also be used in Chapter 5 for validating the methodology and in Chapter 6 as one of the results, called “C2: TI=11.4%”.
2. A case with a span of $d = c = 0.3$ m. This simulation is exactly the same as the other one, with only the span being 1.5 times bigger.

Inflow turbulence is again evaluated close to the ITG and closer to the foil, see Figure 4.9. The two runs agree well close to the ITG (Figure 4.9a). This is to be expected since the turbulence has not been able to develop and, therefore, has not interacted with the boundaries much. If the limited span indeed influences the simulation, such an effect should be better visible closer to the foil. Figure 4.9b, however, also shows a near perfect overlap between the two cases for $f > 60$ Hz. For $25 < f < 60$ Hz a clear difference in energy levels (up to 7 dB) is visible. This could indeed be induced by the limited span, but for $f < 20$ Hz the results again overlap. It is, therefore, more likely that this is merely induced by the duration of the signal. The excellent overlap in both figures shows that the turbulence is accurately captured by the domain with a span of $d = 0.67c$. Additionally, any deviations at lower frequencies (bigger length scales) do not propagate to higher frequencies and thus do not influence the results.

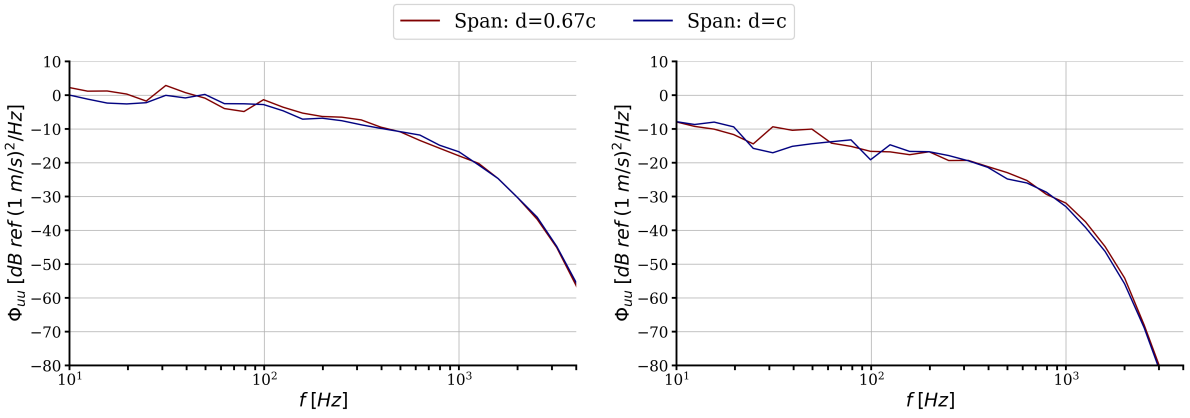

(a) $x/c = -2.$ **(b)** $x/c = -0.2.$

Figure 4.9: Mean decidecade band power density of the streamwise velocity component at two chordwise positions and midspan for the two numerical cases.

Figure 4.10 shows the mean decidecade band power density of the wall pressure directly at the leading edge, as well as further downstream. Again near excellent overlap is found between the two simulations for both chordwise positions. This signifies that no larger structures are generated on the boundary of the foil, which readily became clear from the mesh resolution study. It also shows that the pressure fluctuations on the foil are merely dependent on the accuracy with which the turbulence is resolved. This again shows that the mesh resolution study with limited change in y^+ values over the foil is accurate. The slight difference at lower frequencies can very well be explained by the change in span. Although, as argued before, those lower frequencies are not useful due to the short signal and additionally do not propagate to higher frequencies. Figure 4.10 is taken at midspan. Similar results are, however, found when moving closer to the boundaries of the domain. Indicating that the effects of the boundaries are indeed not present rather than being dampened out when moving along the span of the foil.

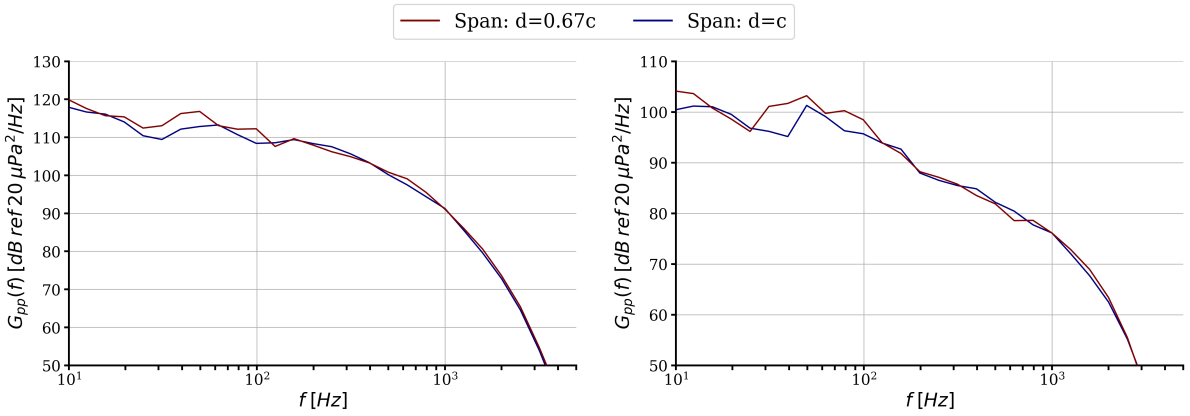

(a) $x/c = 0.$ **(b)** $x/c = 0.5.$

Figure 4.10: Mean decidecade band power density of the wall pressure at two chordwise positions and midspan for the two numerical cases.

To finalize the spanwise domain size study, the far-field acoustic data is compared. Comparison of this also gives insight into the applied correction based on the span, as explained in Section 4.5.3. Figure 4.11 shows the far-field noise at $\theta = 90$ degrees, see Figure 4.3. Both simulations have been corrected based on the span to match the experimental span as will be presented in the next chapter. Again near perfect overlap is found for $100 < f < 2500$ Hz. This not only supports the statement that the results are not influenced by the limited span, but it also shows that the correction applied in Section 4.5.3 is trustworthy. The difference for $f > 2500$ Hz is numerical noise and will be disregarded in this work. To conclude, the chosen span for the remainder of the simulations $d = 0.67c$ does not influence the results. Additionally, the method to correct for the limited span shows reliable results.

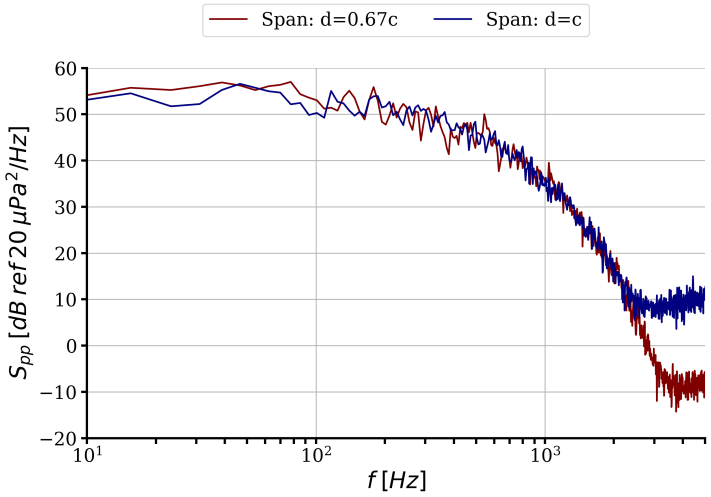

Figure 4.11: Power spectral density of the far-field noise for the two numerical cases at $\theta = 90$ degrees. Numerical cases are corrected based on their span.

5

Validation

Within this chapter, the methodology as proposed in Chapter 4 will be thoroughly validated. Sections 5.1 and 5.2 will validate the turbulence generation for the empty domain (without the foil) and the domain with the foil, respectively. Next, the coherence and pressure data will be validated in Section 5.3. Finally, the validation of the acoustics will be presented in Section 5.4.

A comprehensive overview regarding the validation case input parameters for both the numerical simulation and experiments can be found in Table 5.1. Throughout this chapter, validation data regarding the inflow turbulence without the foil is used from Dos Santos et al. [85], which was made available by the authors. In that work, velocity measurements are performed in an empty wind tunnel by hot-wire anemometry for a turbulent inflow generated by a grid represented by the parameters given in Table 5.1. Validation data regarding the inflow turbulence with the foil present, pressure and acoustics are made available by the authors from Dos Santos et al. [26] and Ribeiro et al. [29]. For more information about these measurements, the reader is referred to these works and to Dos Santos et al. [60]. The next section will start by validating the inflow turbulence generated when the foil is not present in the domain. Note that any references within Section 5.1 to $x/c = 0$ and 'midspan' refer to the intended leading edge of the foil, i.e. the location in the empty domain where the leading would be if the foil was present.

Table 5.1: Parameters of the investigated numerical and experimental cases for validation.

Parameter	**Symbol**	**Numerical simulation**	**Experiment grid [85]**	**Experiment rod [26], [29]**
Label figures	N.A.	C2: TI=11.4%	Exp. Grid	Exp. Rod
Foil type [m]	N.A.	NACA0008		
Foil chord [m]	c	0.3		
Foil span [m]	d	0.2	0.7	
Foil leading edge radius [mm]	r_{LE}	2.1		
Foil maximum thickness [mm]	t_{max}	24		
Turbulence generation	N.A.	Synthetic body forces, Section 4.2	Grid, see Section 3.2.1	Rod, see Section 3.2.1
Turbulence intensity [%] At $x/c = 0$ in empty domain	$TI = u_{rms}/\overline{u}$	11.4	12.3	N.A.
Inflow velocity [m/s]	U_{inf}	25.26	30	25 and 30
Acoustic data	N.A.	Yes	No	Yes

5.1. Inflow turbulence without the foil

The first step for the validation is comparing the inflow turbulence, without the foil, to experimental results. To remove the initial start-up effects of the simulation, a transient scanning analysis (TSA) is performed as was explained in Section 4.5.1. The results of the TSA for the numerical validation case can be seen in Figure 5.1. It becomes clear that the TSA removes an initial transient in the velocity signal, which is not visible to the naked eye. Mean and root-mean-square (RMS) values are calculated based on the results from the TSA. Velocity, fluctuations and acoustics show less response to the outcome of the TSA, whereas the integral length scale experiences more influence from the removed results. To make a comparison between simulations possible, the outcome of the TSA is overruled for the integral length scale computations. For those computations, the discarded time is set at 0.284 s. This includes the time it takes for the turbulence to move through the domain from the ITG to the (intended) leading edge and, additionally, at least one hundred flowthroughs based on the intended integral length scale (50 mm).

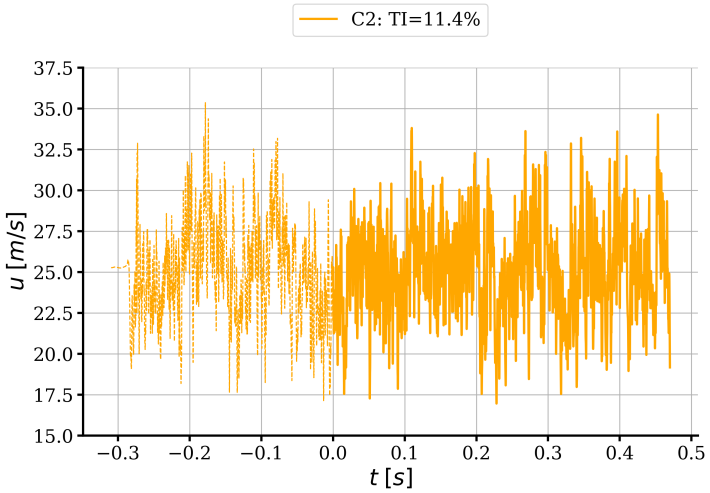

Figure 5.1: Numerical results of the transient scanning analysis applied to the local streamwise velocity u at $x/c = 0$ and midspan. The dashed part of the signal is flagged as the initial transient and is removed from the results.

The outcomes of the TSA can be used to quantify the velocity fluctuations and turbulence intensity over the domain. Here the velocity fluctuations can be defined as $u_i' = u_i - \bar{u}_i$ where i indicates the velocity component. This will return the velocity fluctuations over time. To remove the time element, the root-mean-square of the fluctuations is calculated which can be compared to experimental data. Figure 5.2a shows the root-mean-square of the three velocity fluctuations compared to experimental results. Note that experimental results are only present for u_{rms}. Experimental results have been scaled to correct for the difference in inflow velocity as seen in Table 5.1. Results are scaled by the ratio of inflow velocities, i.e. $u'_{exp,scaled} = u'_{exp} \cdot \frac{U_{inf,sim}}{U_{inf,exp}}$. Figure 5.2a shows a clear peak of the fluctuations just after the ITG. Close to the ITG, the decay of the fluctuations is steep, whereas this slope decreases over the domain. This is desired to ensure that the turbulence has fully developed to a homogeneous state. From $x/c \approx -0.5$ onwards, there is a good agreement between numerical and experimental results. The overlap between the three numerical fluctuations in Figure 5.2a is indicative of isotropic turbulence. The difference visible in the detailed view, less than ten percent, is deemed acceptable.

A similar analysis of the results holds for the turbulence intensity (TI) as shown in Figure 5.2b. As explained in Section 2.3, there are several ways to calculate the turbulence intensity. The one chosen here is based on the mean local streamwise velocity and RMS of the velocity fluctuations, such that $TI = u_{rms}/\bar{u}$. Again, there is good agreement between numerical and experimental results with a minor difference close to $x/c = 0$. The good agreement in Figure 5.2 signifies that the ITG has been accurately tuned so that the turbulence can develop to its intended state and that further results can be compared.

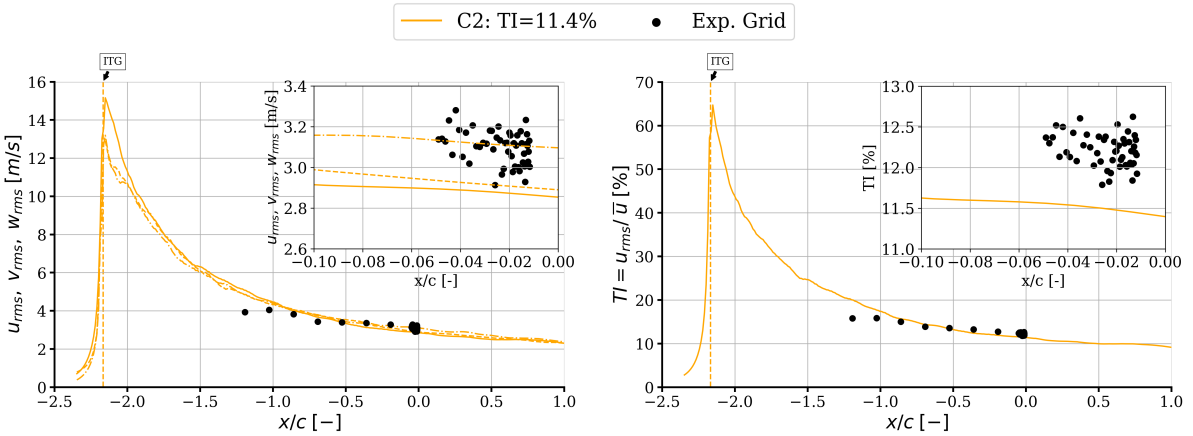

(a) Root-mean-square of velocity fluctuations u_{rms} (——), v_{rms} (- - -) and w_{rms} (-·-·-).

(b) Turbulence Intensity (TI) based on local mean streamwise velocity.

Figure 5.2: Velocity fluctuations (a) and turbulence intensity (b) over the domain at midspan for the numerical validation and experimental (u_{rms}) [85] cases. The vertical orange line represents the location of the inflow turbulence generator (ITG). Experimental data is scaled for (a) to match the inflow conditions of the simulation.

Figure 5.3 shows the mean local streamwise velocity over the domain normalised by the inflow velocity. A clear dip in velocity is visible after the ITG, but the simulation recovers this deficit immediately. The velocity decays slightly throughout the domain, but the deviations from unity are small enough (less than two percent) to state that the turbulence intensity is dominated by the change in velocity fluctuations. Additionally, one can observe that the numerical results show less scatter than the experimental results.

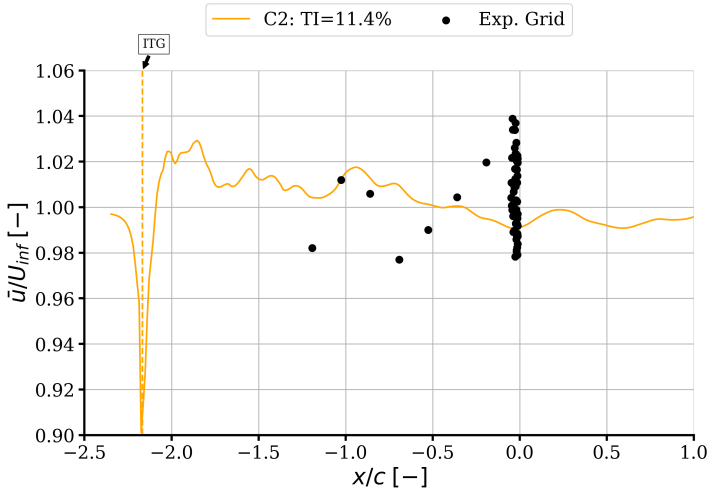

Figure 5.3: Mean streamwise velocity component over the domain at midspan for the numerical validation and experimental [85] cases. The y-axis is normalised by the set inflow velocity.

As remarked before, Figure 5.2a already indicated that the generated turbulence is isotropic. To confirm this statement, the relations between velocity fluctuations over time can be plotted. Figures 5.4a and 5.4b show the relations between $u'v'$ and $u'w'$ over time, respectively. For clarity, the fluctuations have been plotted for every five time steps rather than every single one. No clear visible correlation between the sets is found, supporting the previous statement of isotropic turbulence. To confirm this conclusion, the Pearson correlations and associated p-values are calculated. Table 5.2 shows the Pearson correlations and p-values for the numerical validation case at $x/c = 0$ and midspan. The correlation values for both relations ($u'v'$ and $u'w'$) indicate no clear linear correlation. Additionally, the low p-value indicates a statistically significant correlation, meaning that the calculated Pearson correlations are trustworthy. It can thus be concluded that the turbulence is isotropic at the intended leading edge of the foil.

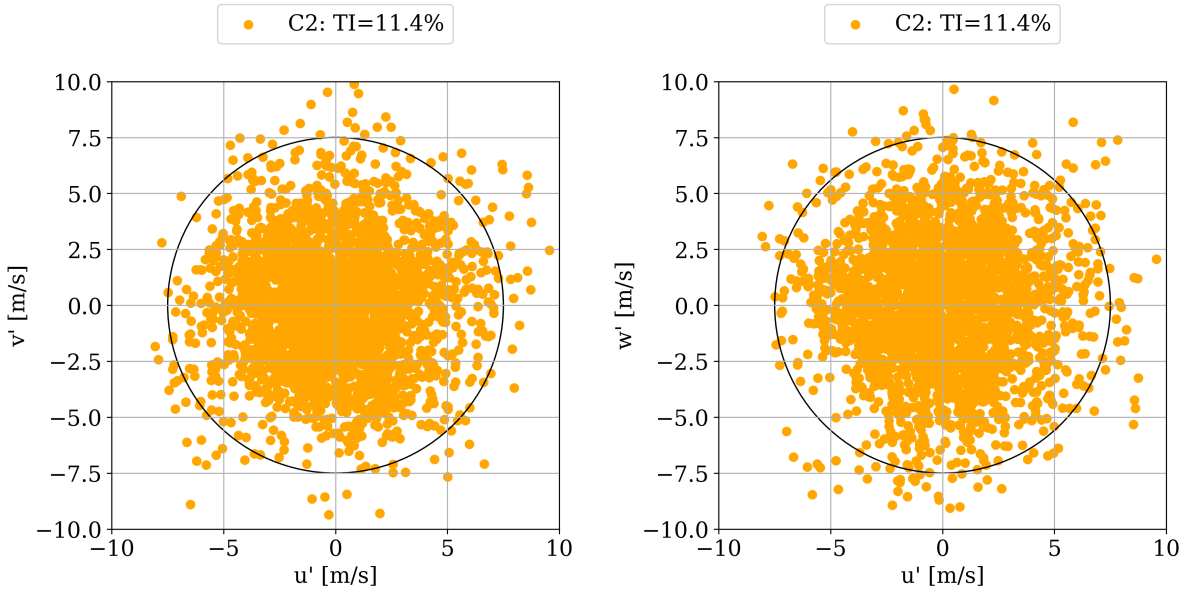

(a) Relation of $u'v'$.

(b) Relation of $u'w'$.

Figure 5.4: Relations of velocity fluctuations at $x/c = 0$ and midspan for the numerical validation case. The circle is plotted as a reference representing isotropic behaviour for which the Pearson correlation goes to zero.

Table 5.2: Pearson correlation and p-values for the numeric validation case. Correlation and p-value are shown for $u'v'$ and $u'w'$.

Case	**Pearson correlation** $u'v'$ **[-]**	**p-value** $u'v'$ **[-]**	**Pearson correlation** $u'w'$ **[-]**	**p-value** $u'w'$ **[-]**
C2: TI=11.4%	6.37E-02	1.96E-02	-3.74E-02	1.67E-02

Figure 5.5 shows the power spectral density (PSD) of the local streamwise velocity component corrected to a decibel scale at $x/c = 0$ and midspan, i.e. $\Phi_{uu} = 10 \cdot log_{10}(\phi_{uu}/u^2_{ref})$ with the reference displayed in the graph. The spectral analysis is based on the method explained in Section 4.5.2. Again, a scaling of the experimental data is adopted. The frequency axis is scaled based on the local Strouhal number, which in turn depends on the local velocity and integral length scale. The power spectral density of the velocity is scaled by analyzing the Von Kármán spectrum for isotropic turbulence, represented by Equations (4), (5) and (8) in Ribeiro et al. [29]. The scalings for the frequency and spectral level of the experiment then become:

$$f_{exp,scaled} = f_{exp} \cdot \frac{\bar{u}_{sim}}{\bar{u}_{exp}} \cdot \frac{\Lambda_{f,exp}}{\Lambda_{f,sim}}, \tag{5.1}$$

$$\phi_{uu,exp,scaled} = \phi_{uu,exp} \cdot \frac{\bar{u}_{exp}}{\bar{u}_{sim}} \cdot \frac{\Lambda_{f,sim}}{\Lambda_{f,exp}} \cdot \left(\frac{u_{rms,sim}}{u_{rms,exp}}\right)^2. \tag{5.2}$$

The mesh cut-off frequency in Figure 5.5 is estimated by dividing the convection velocity of the eddies by the average cell size along the stagnation line. The convection velocity is estimated as 60 % of the inflow velocity. Additionally, a factor of eight is introduced, which represents the minimum amount of cells that is needed to resolve the integral length scale accurately. Such that $f_{cut} = \frac{0.6 \cdot U_{inf}}{\Delta x \cdot 8} \approx 1100$ Hz. Note that this is twice as conservative as the estimate proposed by Peng et al. [52, p.65]. Since the mesh cut-off frequency is merely an indication, no improvement in its estimation was made. A comparison with experimental spectra will more accurately determine the mesh cut-off frequency.

Figure 5.5a shows the PSD from the Welch algorithm. It is hard to make remarks about the overlap with the experimental data, but two observations can readily be made. First, for $f > 1000$ Hz the numerical spectrum drops significantly signifying that the simulation (the mesh) cannot support energy

levels above that frequency. This is in line with the estimated mesh cut-off frequency. Second, for $f < 100$ Hz, the numerical spectrum shows less fluctuating behaviour, indicating that the time signal is too short to describe that frequency range accurately. This is, however, acceptable since the length scales within both the simulation and experiment are an order of magnitude smaller than these lowest frequencies. Additionally, the mesh resolution and domain size studies in Section 4.6 have shown that low-frequency differences do not propagate to higher frequencies.

Comparison to the experimental spectrum can be made by comparing the mean decidecade band power density as shown in Figure 5.5b. The uncertainty is estimated based on Equation 4.11. For $f < 50$ Hz the numerical spectrum occasionally under-predicts the spectrum compared to the experimental outcome. This is likely associated with the length of the time signal, resulting in too little energy for these frequencies. For $50 < f < 1400$, the numerical spectrum over-predicts the experimental spectrum by a maximum of five decibels. Similar decay behaviour is found when comparing the numerical spectrum to the experimental spectrum in this frequency range. Similar to the conclusion based on Figure 5.5a, the numerical spectrum significantly under-predicts the experimental spectrum for $f > 1400$ Hz. This aligns with the estimated mesh cut-off frequency, although that estimate seems too conservative.

This line of reasoning also holds when comparing the numerical results to the Von Kármán spectrum. Additionally, both the Von Kármán spectrum and $f^{-5/3}$ power law are indicative of isotropic turbulence. Reasonable agreement between the slope of the numerical spectrum, power law and Von Kármán spectrum can be seen for $150 < f < 1400$ Hz. In general, a reasonable agreement within +/- 5 dB between the numerical, experimental and Von Kármán spectra is found for $60 < f < 1400$ Hz.

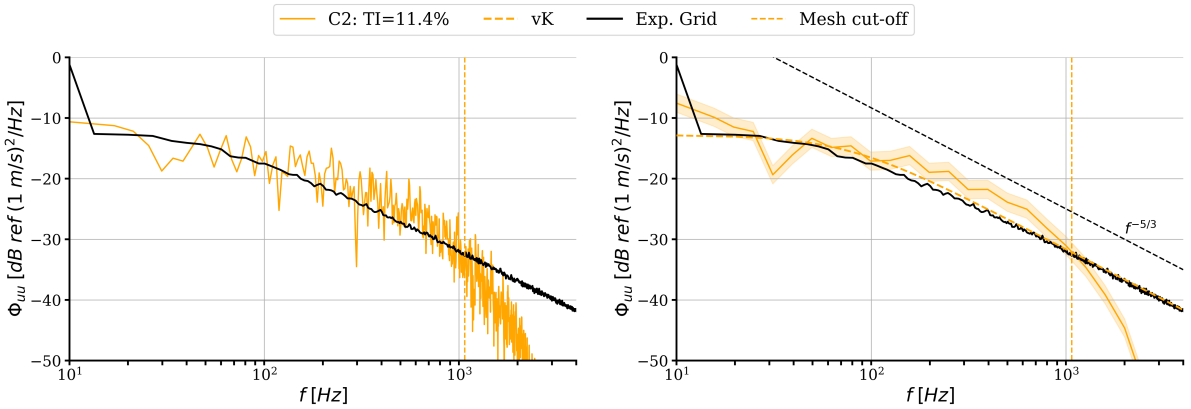

(a) Narrowband spectrum with a frequency resolution of 1 Hz.

(b) Mean decidecade band power density, Von Kármán (vK, see Equation 3.3) and uncertainty bands.

Figure 5.5: Power spectral density of the streamwise velocity component at $x/c = 0$ and midspan for the numerical validation and experimental [85] cases. The experimental frequency and spectrum have been scaled according to Equations 5.1 and 5.2.

The final part of the empty domain validation is to compare the integral length scale. The zero-crossing and fitting procedures have been presented in Section 4.3. The results for the numerical validation and experimental cases can be seen in Figure 5.6. The experimental data within the figure has not been calculated using the method proposed in this work but is taken directly from Dos Santos et al. [85] who applied the zero-crossing method. Several observations can be made. First, throughout the whole domain, there is always a difference between the two numerical results, with the zero-crossing method being larger than the fitting method. This is to be expected since it became clear from Section 2.3 that the fitting procedure is mostly accurate if the decay behaviour of the correlation is smooth. Since the length scale representation in Figure 5.6 is a mean over time, the differences between the two methods will stack, resulting in possibly large disagreements. The fitting method is thus more conservative than the zero-crossing since it disregards any fluctuating behaviour of the autocorrelation below 0.2.

One can also see a clear drop in the integral length scale over the ITG. This is an expected effect since the length scale is calculated based on the correlation of the velocity fluctuations in the streamwise direction. Since there is no turbulence in front of the ITG, the velocity fluctuations will be correlated for a longer time as there is nothing to disturb them, leading to bigger (unrealistic) values. In turn, this also explains the tendency of the integral length scale to increase in size over the domain. This behaviour is present in both the numerical and experimental results, while the latter increases less.

When comparing the numerical data to the experimental data, one can see that the results do not match well. First, the overall level of the numerical and experimental results do not match. Especially the fitting method deviates a lot from the experimental values, which was readily explained by it being too conservative. Nonetheless, close to the intended leading edge ($x/c = 0$), the zero-crossing method also predicts values smaller than those within the experiments. No scaling has, however, been implemented for the experimental data in Figure 5.6. One theory is that the integral length scale scales with the magnitude of the velocity fluctuations. If that scaling is applied, the integral length scales from the experiment shifts downwards, for which the overlap between numerical and experimental results is much better. Nonetheless, the zero-crossing method still significantly overestimates most of the experimental results. More accurate control over the length scale is desired, but it will be proven later that this is not feasible with the current setup.

Second, the experimental data shows much less fluctuating behaviour over the domain. This is a direct effect of the duration of the signal used for the integral length scale computation. Since the numerical signal is rather short, the autocorrelation is hard to predict for larger values of the time lag, being one of the main reasons why the fitting method was proposed in this work. Indeed, the fitting method shows less fluctuations in the length scale over the domain, but it also seems to be too conservative. To gain more accurate control over the length scale, a possible solution is to increase the simulated time. This was, however, not feasible within the limited time of the project.

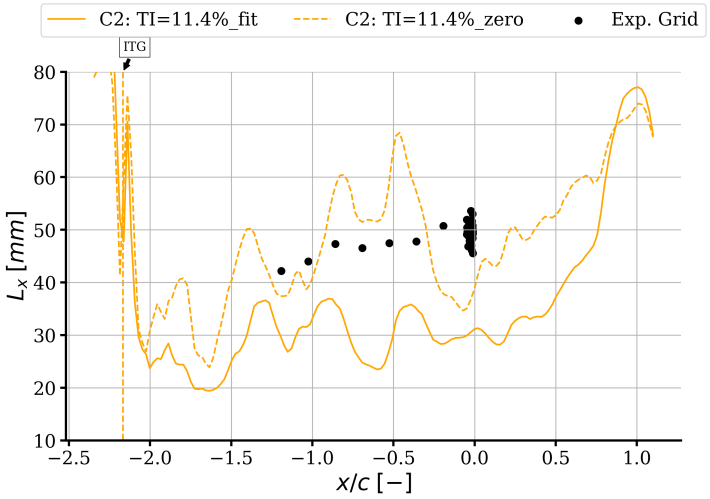

Figure 5.6: Integral length scale over the domain at midspan for the numerical validation and experimental [85] cases. Fit and zero refer to the fitting and zero-crossing methods, respectively. Experimental data is taken as presented and is not scaled nor recalculated.

An alternative was to perform a study on the different input parameters that the inflow turbulence generator (ITG) takes to study the effects of those on the integral length scale. The study consisted of studying different parameters of the ITG that could influence the integral length scale generation and determination. As became clear from Section 4.2, the ITG takes only a few input parameters. A description of these, together with their impact on the integral length scale, are discussed below:

- The size of the ITG in the spanwise and vertical directions were not investigated since these were fixed by the size of the domain.
- The thickness of the ITG over which the body forces are spread. An increase of thickness resulted in an increase of the integral length scale. This feels natural since the integral length scale has more cells (thickness) to reach its desired level. The downside to this increase is the associated increase of body forces for the velocity fluctuations to reach the desired value, which leads to an unwanted increase of computational time due to slower convergence.
- The amplification factor showed little effect on the integral length scale. From Equation 4.2 it became clear that it only amplifies the body forces to speed up the convergence to the desired velocity fluctuations. A slight increase in the integral length scale was observed for an increase in the amplification factor. The downside to this method is the associated increase in fluctuations.

- The input Reynolds stresses were not altered since those predominantly determine the achieved velocity fluctuations. It was key to alter the integral length scale without impacting the turbulence intensity such that they could be evaluated seperately from one another. It will become clear later on whether the chosen Reynolds stresses also influenced the integral length scale.
- The input value for the integral length scale had, strangely enough, only a small impact on the calculated integral length scale. A doubling in the input value led only to a small increase of the value retrieved during post-processing.
- The mesh refinement, although technically not an input of the ITG, showed a decrease of the integral length scale for a finer mesh. Differences were, however, too small to accept the large increase of computational time.

Control of the integral length scale through a change of ITG size, ITG thickness, amplification factor, Reynolds stresses and mesh refinement is not desired since these also induce a change of other turbulence quantities. The integral length scale showed little to no response to a change of its input value. It is likely that the body forces, as calculated from Equation 4.2, are not able to control the length scale accurately. Additionally, none of the methods above improved the behaviour of the integral length scale over the domain. This seems to remain dominantly influenced by the duration of the simulations. More accurate control was desired, but it was unavailable for the current setup. For this work the length scale has been left untouched, whereas a change due to the Reynolds stresses will be quantified. For future works, it is recommended that effort be put into the implementation of a different turbulence generation method, which allows more accurate control over the integral length scale.

5.2. Inflow turbulence with the foil

Validation of the inflow turbulence with the foil present is performed similarly as for the no-foil case. One key difference is that numerical data is compared not only to grid-generated experimental data but also to rod-generated experimental data. This choice has been made to investigate the decay behaviour of different parameters when approaching the leading edge for different turbulent generation methods and, hence, turbulence statistics. To allow for a fair comparison, all of the data is normalised by values upstream, which are not yet affected by the presence of the foil. Due to the normalisation, none of the data has to be scaled. Note that any reference to $x/c = 0$ and 'midspan' now refer to the leading edge of the foil. The coordinates of this location are the same as in Section 5.1.

The first parameter to investigate is the mean velocity in the streamwise direction. Normalisation is taken at the point where the mean velocity of the numerical validation case reaches a plateau, as seen from the leading edge. This was established to be at $x/r_{LE} = -47$. Normalisation for the experimental results is taken at the point closest to the established point. The results for the normalised mean streamwise velocity can be seen in Figure 5.7a, with a detailed view closer to the leading edge in Figure 5.7b. Please note that the x-axis is now normalised by the radius of the leading edge. For reference, the ITG is located at $x/c = -2.17 \rightarrow x/r_{LE} = -310$.

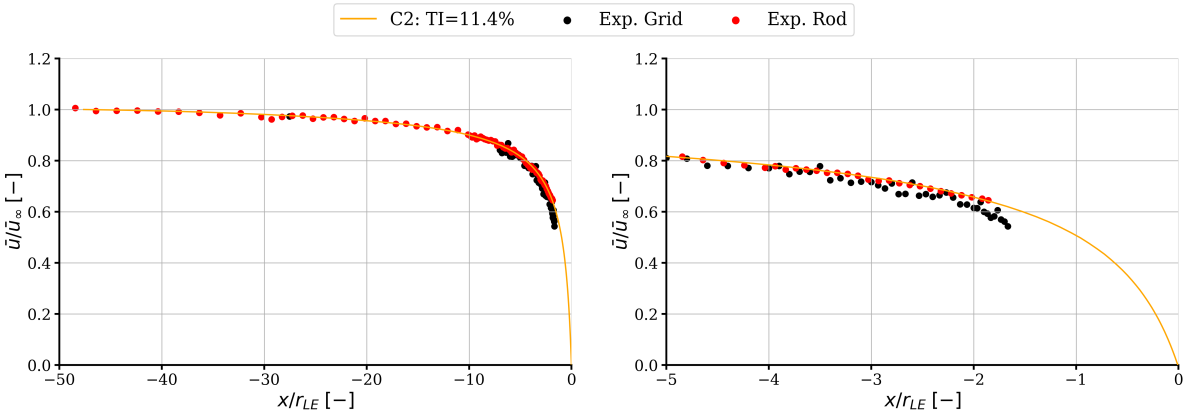

(a) Normalisation taken at $\frac{x}{r_{LE}} = -47$.

(b) Detailed view of (a), normalisation taken at $\frac{x}{r_{LE}} = -47$.

Figure 5.7: Normalised mean local streamwise velocity over the domain at midspan for the numerical validation and experimental [26] cases. The y-axis is normalised by the streamwise velocity at the specified location in the sub-caption.

Excellent overlap between numerical and both experimental data sets is observed. Only close to the leading edge, $\frac{x}{r_{LE}} > -5$, does the grid-generated inflow decay slightly faster. The difference is too minor for it to be important and is likely induced by the uncertainty of the normalisation procedure that is used. Normalisation is taken at $\frac{x}{r_{LE}} = -47$, but from Figure 5.7a it becomes clear that there is no data point for the grid-generated turbulence at this point. The closest points for that case are at $\frac{x}{r_{LE}} = -27 \wedge -52$, with the latter being outside of the x-axis limit. The second point is, however, taken for normalisation since it is closest to the desired point. Since the mean streamwise velocity is slightly higher there, it leads to a bias in the normalisation shifting the data downwards. This effect is most dominant for data closest to the leading edge. Data normalisation could have been improved, but the excellent overlap readily validates the results.

A similar analysis can be conducted for the RMS of the velocity fluctuations. One key difference is the decision at which point the normalisation is taken. This is kept the same as for the mean streamwise velocity rather than performing the same plateau analysis again. Two reasons can be given for this choice. First, this allows for a fairer comparison with the decay plot of the mean velocity. Second, the RMS of the velocity fluctuations do not reach a plateau as was readily seen in Figure 5.2a showing the fluctuations without the foil present. Since the turbulence is decaying throughout the domain, it is impossible to pinpoint the start of a constant plateau. To overcome this, the normalisation point was chosen to be kept constant.

The results for the normalisation of the RMS of the streamwise velocity fluctuations and a detailed view close to the leading edge can be seen in Figures 5.8a and 5.8b, respectively. Again, excellent overlap between numerical and experimental data is found for all positions up to the leading edge. Only a small difference occurs for $-47 < \frac{x}{r_{LE}} < -15$. This is a consequence of the turbulence that is naturally decaying throughout the domain, regardless of the fact if the foil is present or not. Figure 5.2a already showed that the decay is slightly more for the numerical case than for the grid-generated experimental case. This additional decay leads to a slight shift of the RMS normalised values in Figure 5.8a. The difference disappears when moving towards the leading edge, where the effect of the foil starts to dominate over the natural decay behaviour. Excellent overlap between numerical and experimental data is also found close to the leading edge as visible in Figure 5.8b.

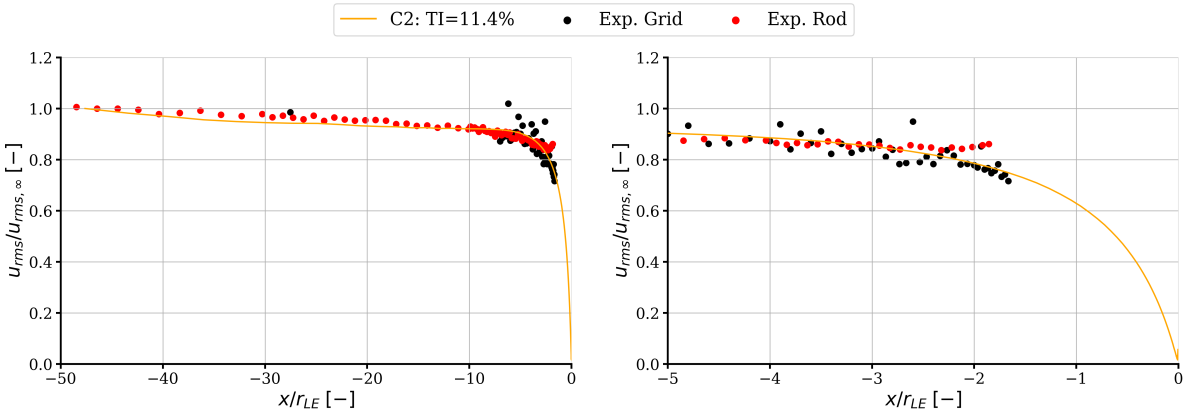

(a) Normalisation taken at $\frac{x}{r_{LE}} = -47$.

(b) Detailed view of (a), normalisation taken at $\frac{x}{r_{LE}} = -47$.

Figure 5.8: Normalised root-mean-square velocity fluctuations over the domain at midspan for the numerical validation and experimental [26] cases. The y-axis is normalised by the value at the specified location in the sub-caption.

Figure 5.9 shows the results for the normalisation of the integral length scale when moving to the leading edge. Two different positions for data normalization have been chosen. The first aligns with the previous analysis, i.e. at $x/r_{LE} = -47$. From that point of normalisation, it becomes clear that the overlap between numerical and experimental data is poor. This is likely the effect of the normalisation value chosen for the integral length scale. After the normalisation, the integral length scale from the numerical data still keeps its normal behaviour of increasing throughout the domain before it starts to decrease due to the interaction with the leading edge. The big spread of experimental data in Figure 5.9 for $-50 < x/r_{LE} < -30$ also makes it hard to pick a specific point for normalisation as well.

From Figure 5.9a it becomes clear that the integral length scale for the rod-generated turbulence case also does not decay before $x/r_{LE} = -20$, i.e. the normalised value fluctuates around one. A second point of normalisation is, therefore, chosen at $x/r_{LE} = -20$. This is much closer to the leading edge, such that the effect of the foil dominates over the natural tendency of the integral length scale to increase. Indeed, Figure 5.9b shows much better overlap between numerical and experimental data both for values close to the leading edge, as well as further upstream.

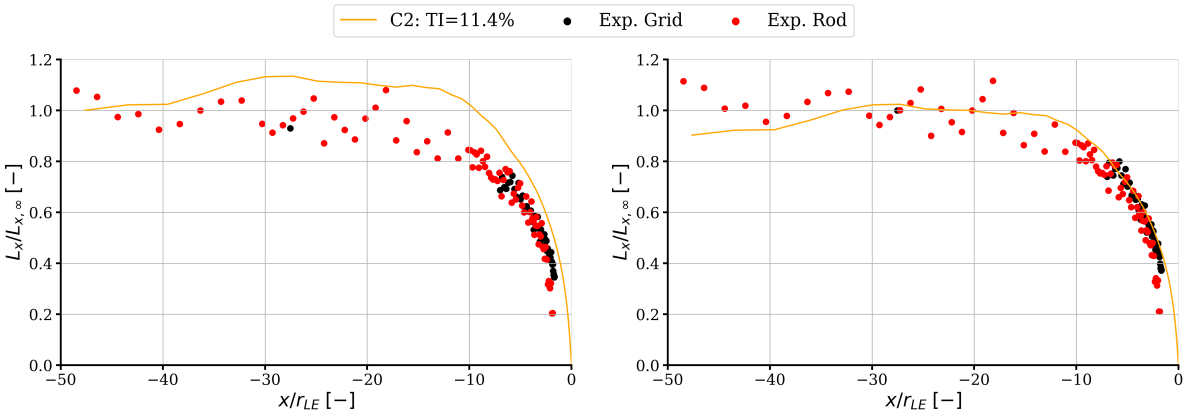

(a) Normalisation taken at $\frac{x}{r_{LE}} = -47$.

(b) Normalisation taken at $\frac{x}{r_{LE}} = -20$.

Figure 5.9: Normalised integral length scale over the domain at midspan for the numerical validation and experimental [26] cases. Only data from the fitting method is presented. The y-axis is normalised by the value at the specified location in the sub-caption. Experimental data is taken as presented and is not scaled nor recalculated.

5.3. Coherence and pressure

Validation of acoustics can only be performed once both the pressure and coherence data have been evaluated. The outcomes of this section will, amongst other things, determine the acoustic correction and the definition of the FW-H surface.

From the methodology, see Section 4.5.3, it became clear that there are three methods to calculate the coherence length as input for the acoustic correction for the limited span of the simulation. The method proposed by Kato et al. [90] is deemed too crude and will not be used. The second method is based on Equation 4.7, which calculates the coherence length based on the Von Kármán model. Although dependent on frequency, it is sufficient to look at the maximum of that method. If that maximum is smaller than the span of the simulation, the acoustic correction will always remain purely incoherent, i.e. the top line of Equation 4.6. The maximum coherence length estimated by this method, for $U_{inf} = 25.26$ m/s and $\Lambda_f = 0.04$ m (see Figure 5.6), is 0.039 m. This is indeed smaller than the span of the simulation ($d_{sim} = 0.2$ m), signifying that for all frequencies, the correction will remain purely incoherent. There are, however, several downsides to this method:

- It does not account for local turbulence distortion (over the chord of the foil), i.e. the input parameters are reference values taken from the empty domain;
- It does not account for influences of the boundary conditions, i.e. it does not account for the actual properties of the flow.
- It assumes isotropic turbulence, which is not true for turbulence distortion near the leading edge.

The third method should rule out all of these assumptions by calculating the coherence length based on the magnitude squared coherence from the pressure, as presented in Equations 4.8 and 4.9 respectively. The coherence (being the root of the magnitude squared coherence) for several chordwise positions can be seen in Figure 5.10. The reference for the coherence $\phi_{pp}(0,0)$ is calculated at midspan $z/d_{\frac{1}{2}} = 0$. For clarity, only half of the span is shown since the other half showed similar results. The contour line depicts the critical value of $\gamma_{p_i,p_i} = 0.5$, as proposed by Kato et al. [90]. Some noise can be seen in the figures, especially for higher frequencies. This noise could have been removed by applying a sliding window, but for the current analysis that was unnecessary.

Several observations based on these figures can be made. First, it becomes obvious that there is a front representing the increase of the coherence. This front is already visible at $x/c = 0$, after which it moves to higher frequencies when going further down the foil. The associated effect is that for those frequencies, the coherence length also (wrongfully) increases. The increase of coherence is a combination of the averaging behaviour of RANS near the foil and the drop in pressure (fluctuations) over the foil. The latter will become clear later on in this section. This implies that Equation 4.6 should be not only a function of frequency and span but also a function of the chordwise position. The current setup, however, does not allow for a correction based on the chordwise position. For future work, it is recommended to divide the FW-H surface into different strips along the chord of the foil. Then corrections can be applied per strip accounting for the increasing coherence length over the chord of the foil. Note that the Von Kármán estimate of the coherence length also does not account for this moving front.

To remove the effect of the increasing coherence (length), a lower frequency bound for the data evaluation is chosen. This method is favourable since acoustic data will be evaluated from spectra as well, and it removes a portion of the data for which the duration of the simulations is likely too short. Additionally, it removes the need for assumptions on how to model the coherence within the front where it does not go to zero. The choice of the lower bound should satisfy $L_\gamma(f) < d_{sim}\ \forall f$ such that the spanwise correction is always incoherent and thereby applicable to all chordwise positions of the (later determined) FW-H surface. From Figure 5.10 it becomes clear that the front has proceeded the furthest for $x/c = 0.5$. If the lower bound is indeed chosen from Figure 5.10d, the statement $L_\gamma(f) < d_{sim} \forall f$ will always be true as long as it is proven that $L_\gamma(f_{low}) < d_{sim}\ at\ x/c = 0.5$ where f_{low} represents the chosen lower frequency bound. From Figure 5.10d, the lower bound is set a $f_{low} = 400$ Hz. This is outside of the front where the coherence is ill-defined. The requirement for the coherence length to be smaller than the span is satisfied at that frequency. By using Equation 4.8 it follows that $L_\gamma(f_{low} = 400\ Hz) \approx 0.044\ m < d_{sim}\ at\ x/c = 0.5$. A more detailed analysis with probes between $x/c = 0.05$ (Figure 5.10c) and $x/c = 0.5$ (Figure 5.10d) could result in a downwards shift of the frequency bound. It will, however, become clear in Section 5.4 that lowering this bound is not feasible based on the acoustics validation.

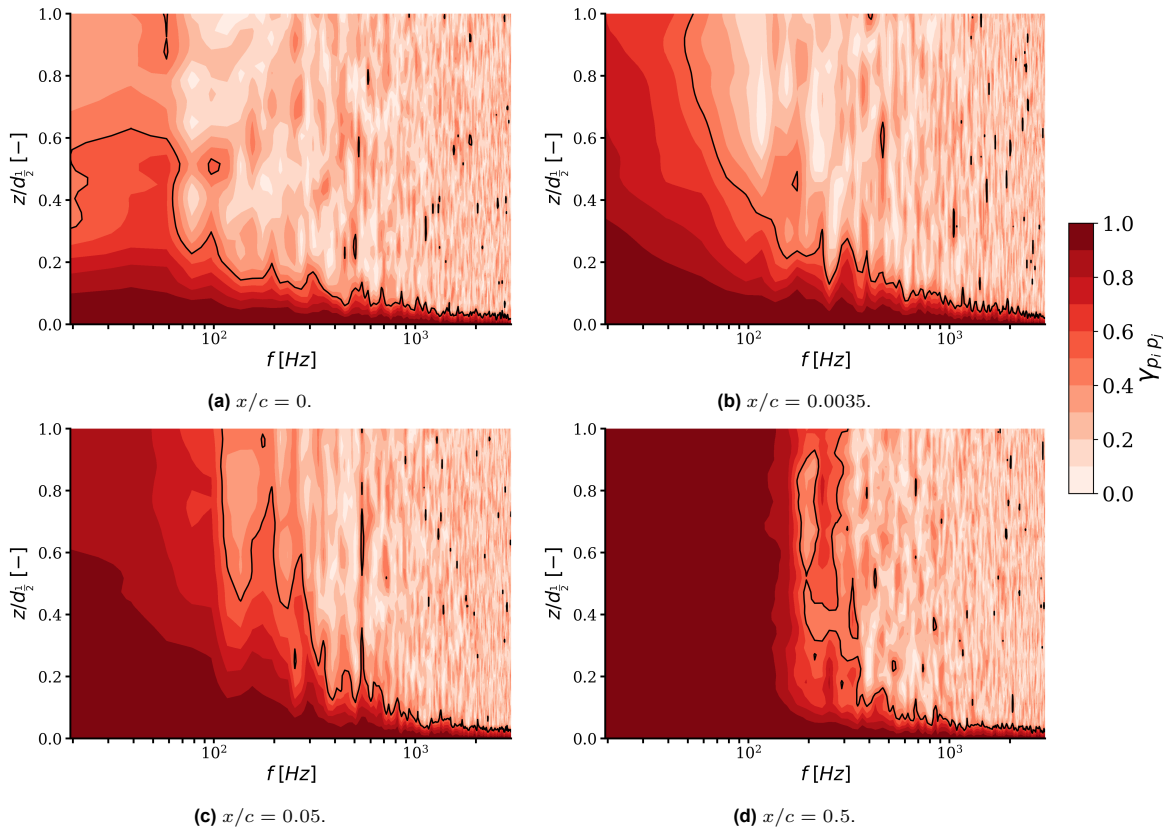

(a) $x/c = 0.$

(b) $x/c = 0.0035.$

(c) $x/c = 0.05.$

(d) $x/c = 0.5.$

Figure 5.10: Spanwise coherence for different chordwise positions for the numerical validation case. The reference for each coherence calculation is taken at midspan ($z/d_{\frac{1}{2}} = 0$) and the y-axis is made non-dimensional by the half span ($d_{\frac{1}{2}}$). The black contour line represents $\gamma_{p_i,p_i} = 0.5$.

For the frequency bound to hold, two requirements for this and future cases have to be satisfied:

1. The FW-H solid data surface (SDS) may not extend beyond $x/c = 0.5$ since after that point, the lower frequency bound may not hold.
2. For other simulations the requirement $L_\gamma(f_{low} = 400\,Hz) < d_{sim}\ at\ x/c = 0.5$ should be verified.

Figure 5.10 does not present a clear upper bound for the frequency. Not included in the figure ($f > 3000$ Hz) is, however, a region where numerical errors heavily influenced the coherence. This is far above the estimated mesh cut-off frequency and is therefore not visualised.

As stated before, the upper limit of the FW-H solid data surface (SDS) has to be chosen at a chordwise position smaller than $x/c = 0.5$. Within this work, the upper chordwise limit of the SDS was determined to be the position where the far-field noise was no longer directly influenced by the distortion of the turbulence on the leading edge. To quantify this position, the root-mean-square of the wall pressure can be evaluated. Figure 5.11 shows the RMS of the wall pressure at midspan over the chord of the foil. There is an obvious peak near the leading edge of the foil due to the distortion of the turbulence. The wall pressure decays when moving along the chord to a near-constant state. The position where the leading edge no longer influences the wall pressure is determined to be at the point where the RMS has levelled out. From Figure 5.11b this position was set at $x/c = 0.2$. This fits the requirement made previously for the FW-H surface not to extend beyond $x/c = 0.5$. Additionally, such a choice would also remove any unwanted noise sources associated with the trailing edge, as introduced in Section 2.1.

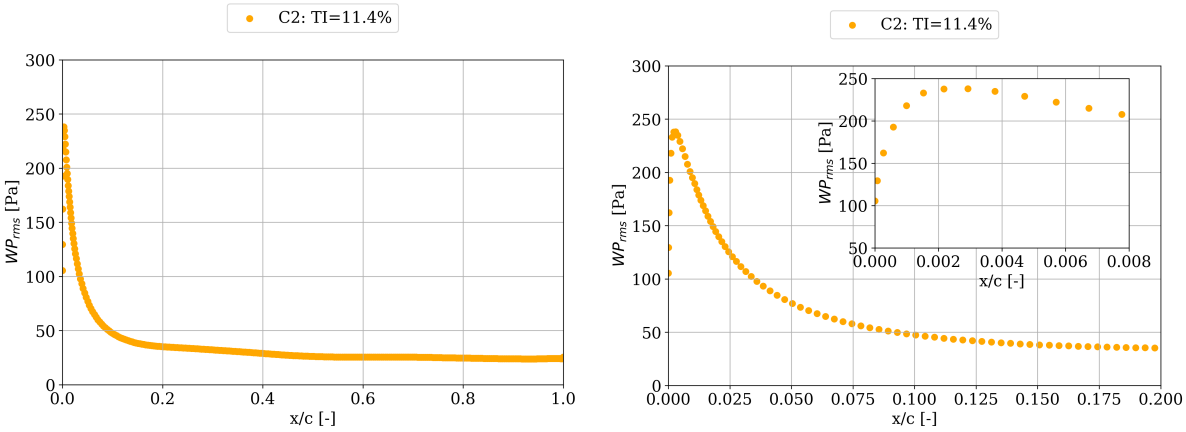

(a) Full chord.

(b) Detailed view of (a) showing data closer to the leading edge.

Figure 5.11: Root-mean-square of the wall pressure over the foil at midspan for the numerical validation case.

This choice of FW-H data surface can be supported by evaluating the spectra of the wall pressure fluctuations. To do so, these first have to be validated. Figure 5.12 shows the wall pressure fluctuations spectra at midspan of the foil for two chordwise positions. Experimental data is shown for both grid and rod-generated turbulence to establish differences between the two methods. Several observations based on Figure 5.12a can be made. First, there is a clear difference between the three experimental cases. For $f > 120$ Hz both rod-generated spectra show more energy than the grid-generated turbulence. This is due to the higher velocity fluctuations in the wake of the rod compared to the grid for similar inflow velocity. The peaks in the spectra for the rod-generated turbulence represent the shedding frequency of the Von Kármán vortex street in the wake of the rod. Most energy will be created at these frequencies, which will be cascaded to higher frequencies as explained in Section 2.2. This shedding frequency represents the lowest frequency where energy is put into the system. This also explains why, for $10 < f < 120$ Hz, both rod-generated spectra contain less energy compared to the grid-generated one. These mechanisms have readily been introduced in Section 3.2 and should, therefore, not come as a surprise.

Comparing the numerical and grid experimental data shows excellent overlap for $80 < f < 800$ Hz. This overlap is straightforward since the turbulence has been tuned for a similar inflow velocity. From $f > 800$ Hz the numerical data starts to underpredict the experimental data. This is somewhat in

line with the mesh cut-off frequency. For $f < 80$ Hz, the numerical data significantly overpredicts the experimental data. A possible reason could be the stronger interaction with the boundary conditions at those lower frequencies. Larger coherent structures likely tend to interact more with the boundary conditions than smaller structures. Figure 5.10b indeed shows that for $f < 80$ Hz the coherence no longer reaches zero, indicating coherent structures larger than the computational domain. Figure 5.12b confirms this suspicion by showing that the numerical spectrum now overpredicts the energy at most frequencies. This aligns with the movement of the coherence front to higher frequencies when moving along the chord of the foil, see Figure 5.10. The overprediction will likely lead to an increased sound pressure level at the different receivers as well. The choice for a lower frequency bound based on the coherence will slightly improve on this, but as visible in Figure 5.12b, energy is still spread to higher frequencies as well. Contradicting this statement are the results from Section 4.6.2 that did not indicate this effect. It could, however, still be the case that the variation in spanwise domain size is still too small to quantify this effect accurately. It is, therefore, recommended for future work to further address this low-frequency difference (by increasing the span size of the domain).

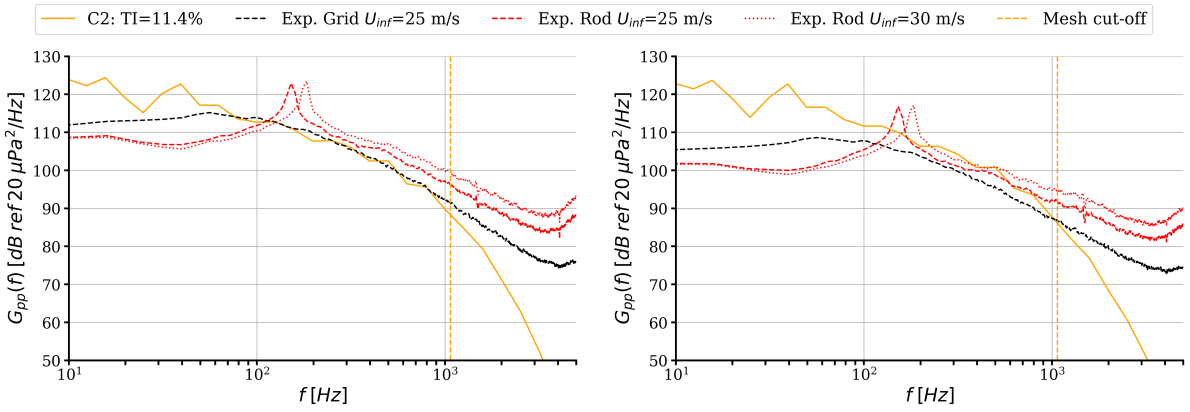

(a) $x/c = 0.0035$. **(b)** $x/c = 0.007$.

Figure 5.12: Mean decidecade band power density of the wall pressure fluctuations at midspan for different chordwise positions for the numerical validation and experimental [26] cases. Experimental data is not scaled.

Finally, to support the data surface for the FW-H analysis, Figure 5.13 shows the numerical spectra of the wall pressure fluctuations for different chordwise positions. Close to the leading edge, the energy levels are similar over the whole frequency range. What stands out is that, for movement along the chord, the energy levels first increase after which they start decreasing. This behaviour aligns with the development of the wall pressure RMS values very close to the leading edge, as is visible in the detailed view of Figure 5.11b. The energy levels drop rapidly afterwards when moving along the chord of the foil. A big drop is especially seen when moving from $x/c = 0.05$ to $x/c = 0.5$. This aligns with the significant drop in wall pressure RMS values as visualised in Figure 5.11b. The choice for the FW-H surface was made such that it no longer 'felt the influence of the leading edge'. Figure 5.13 confirms the choice for $x/c = 0.2$ by showing that energy levels have dropped significantly. Again, more probes between $x/c = 0.05$ and $x/c = 0.5$ could have improved this choice even further, but for the analysis made in this work this was deemed sufficient.

The significant drop in wall pressure fluctuations along the foil also aligns well with the increase of coherence, as was found in Figure 5.10. A significant drop in pressure fluctuations makes it 'easier' for RANS to average the result. An averaged result will evidently show a coherence value tending to one. This explains the moving front in Figure 5.10, the combined effect of the pressure fluctuations and RANS on the coherence, and it again signifies the need for a lower frequency bound as well as a solid definition for the FW-H surface. Both of those were given within this section.

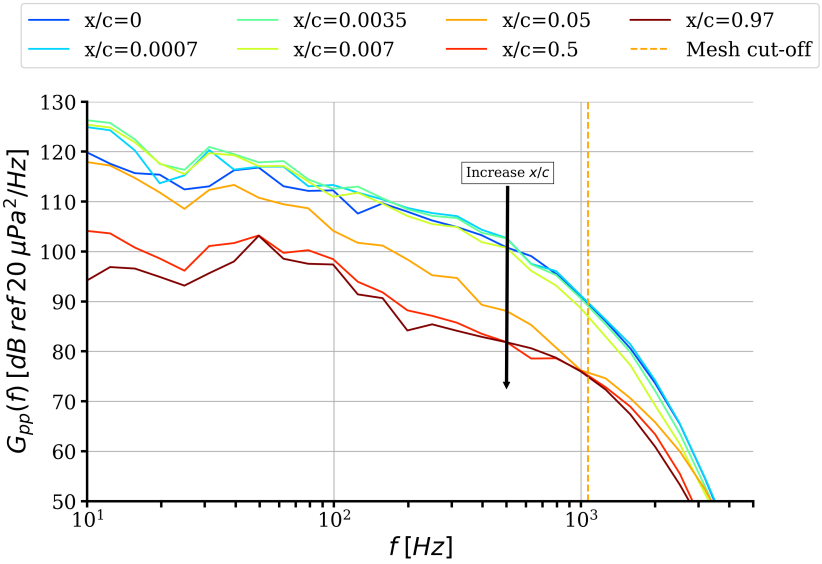

Figure 5.13: Mean decidecade band power density of the wall pressure fluctuations at midspan for different chordwise positions for the numerical validation case.

5.4. Far-field acoustics

Finally, the far-field acoustics, as generated by the airfoil's leading edge, can be validated. Remember Figure 4.3, which showed the placement of the receivers relative to the foil. Receivers are placed at every two degrees in a circle around the foil. The circle has a radius of 1.5 m, with its centre at mid-chord and midspan. The angle θ defines the angle of the receiver. The receiver downstream is defined as $\theta = 0$ degrees, which is in line with the trailing edge of the foil. The receiver upstream, in line with the leading edge of the foil, is located at $\theta = 180$ degrees. Experimental validation data is only present for $\theta = 90$ degrees, whereas numerical data is available for the receivers at $\theta = 30, 60, 90, 120, 150$ degrees. Numerical data is taken from Ribeiro et al. [29] who performed a similar analysis for leading edge generated noise. They simulated the flow using the lattice-Boltzmann method (LBM). The turbulence is generated by modelling a grid in the flow with a set inflow speed of $U_{inf} = 25$ m/s. The similar inflow speed makes direct comparison possible. Experimental data is only available for rod-generated turbulence as grid-generated turbulence generated too much background noise, as was described in Section 3.2.1. Evaluations regarding far-field noise are made based on spectral analysis as described in Section 4.5.2 rather than directly computing RMS values from the data. This method is preferred since it allows validation over the frequency range and the opportunity to base the far-field noise on a desired frequency range and, hence, adhere to the lower frequency bound readily set.

Figure 5.14 shows the far-field noise spectra for an receiver at $\theta = 90$ degrees. Several observations can be made. The vortex shedding frequency for the rod, which was visible in Figure 5.12, is also present in the far-field noise spectra at similar frequencies, indicated by 1. It becomes clear that a lot of energy is emitted at this shedding frequency, which is also partially spread to other nearby frequencies. These frequencies are thus irrelevant since the associated coherent turbulent structures are absent in the numerically-generated isotropic turbulent flow. Section 3.2.1 stated that the shedding frequency could be beneficial since it does not emit noise over the full frequency range, but from Figure 5.14 it becomes clear that this is not the case. Additionally, any data outside the bounds indicated by 2 and 4 is to be disregarded since the wind tunnel background noise dominates the signal outside these bounds. Experimental validation data is therefore only available for higher frequencies ($400 < f < 2500$ Hz), which is deemed adequate since the lower bound for integration was readily set at $f_{low} = 400$ Hz.

When comparing the numerical data to either of the experimental cases, poor overlap is found for $10 < f < 400$ Hz. The shedding frequency of the rod readily explained this. For $600 < f < 2000$ Hz the overlap between the numerical and $U_{inf} = 30$ m/s rod case is very good. However, it is unexpected since the turbulence parameters differ for rod-generated turbulence compared to grid-generated turbulence (for which numerical tuning was performed). Section 3.2.1 already introduced these differences,

namely the velocity, fluctuations, isotropy and integral length scale. The deficit in velocity and increase of integral length scale in the wake reduce the far-field noise according to Equation 3.1, whereas the increase in fluctuations increases the far-field noise. It is hard to quantify how these exactly scale the data, but the overlap of data in Figure 5.14 might not be entirely wrong.

The numerical data does, however, show the same trend observed from the experimental data regarding the high-frequency decay of the far-field noise. Independent of the experimental case, the slope of the numerical spectrum is similar to that of the experiments, indicating that the solver can accurately capture the high-frequency decay, disregarding the exact levels. This is sufficient for the current work since the scaling based on the four cases is going to be evaluated rather than exact levels. For $f > 2000$ Hz does the numerical data start to decay faster compared to experimental results, where the latter might already be influenced by the wind tunnel background noise. The upper bound for acoustic integration is set at $f_{high} = 2000$ Hz based on the overlap shown in Figure 5.14. This is almost twice as high as the estimated numerical mesh cut-off frequency, which seems too conservative for acoustic data. The difference is likely induced by the input used to calculate the cut-off frequency. The cut-off frequency was estimated from the average cell size between the ITG and the foil in the empty domain. Since mesh refinement is adopted near the leading edge and in the boundary layer, as explained in Section 4.4, the mesh cut-off frequency is likely higher at those positions. It could, however, also be possible that turbulence at certain frequencies also induces pressure fluctuations at higher frequencies. The current results, however, do not allow an investigation into this hypothesis.

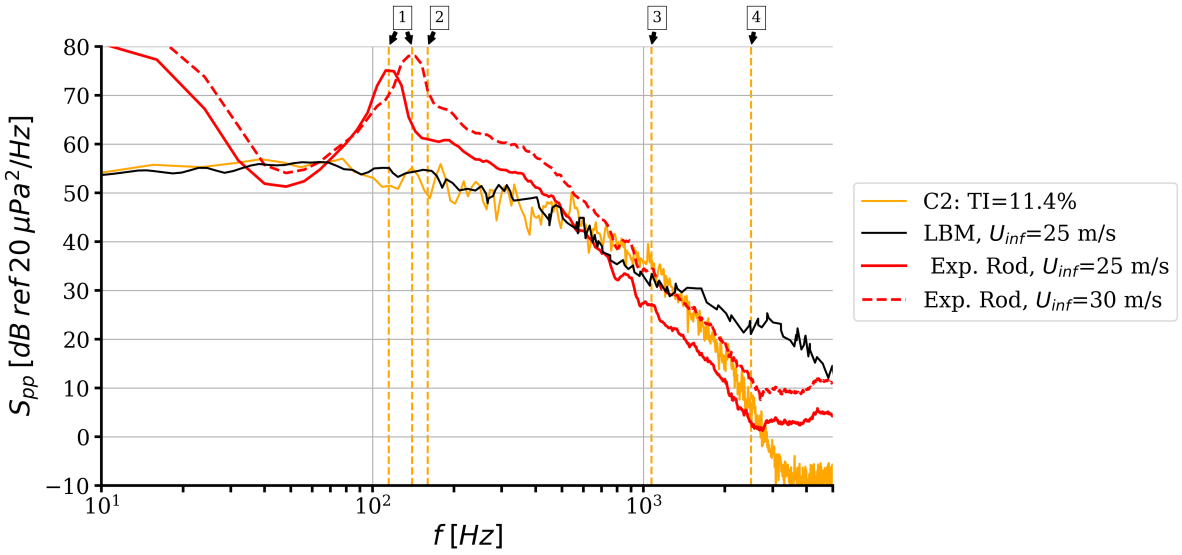

Figure 5.14: Power spectral density of the far-field noise for the numerical validation, LBM [29] and experimental [26] cases. Data is for a receiver at $\theta = 90$ degrees. The numerical validation case is corrected for the limited span, and the experimental/LBM data is not scaled. The numbers signify the rod-shedding frequencies (1), lower and upper bounds of experimental acoustic data (2, 4) and the estimated numerical mesh cut-off (3).

The numerical validation data can also be compared to the numerical data based on the LBM as presented by Ribeiro et al. [29]. Both data sets show excellent overlap for $10 < f < 1500$ Hz after which the LBM data deviates more from the current methodology. This is to be expected since both are for equal inflow velocity and turbulence generated by a grid. The deviations for $f > 1500$ Hz show that the current methodology can better capture the high-frequency decay behaviour when compared to experimental trends. The LBM result shows that the solver can also capture the low-frequency trend, which could not be done from experimental data. They also show that the lower bound for integration ($f_{low} = 400$ Hz) is acceptable.

Key takeaway is that the current methodology can accurately capture the high-frequency trend of far-field noise for $600 < f < 2000$ Hz as observed from experimental data. Additionally, the current setup is accurate for $10 < f < 1500$ Hz compared to LBM simulation data. For $f > 2000$ Hz, does the numerical data start to decay faster compared to experimental results, where the latter might already be influenced by the wind tunnel background noise. Based on the experimental and numerical validation data, the frequency bounds for sound pressure level integration are set at $400 < f < 2000$ Hz.

Figure 5.15 shows the sound pressure level as integrated from the far-field noise power spectral densities (such as that in Figure 5.14) between the lower and upper bounds as determined before. From the figure it becomes clear that limited validation data is available. At $\theta = 90$ degrees, the overlap between three of the cases is perfect. This is, however, not expected since those three cases did not show perfect overlap in Figure 5.14. This highlights the importance of evaluation based on the integration of the PSD rather than taking the RMS of the pressure fluctuations. Key takeaway from comparing the numerical and experimental cases in Figure 5.15 is, therefore, that the acoustics at $\theta = 90$ degrees are similar with a maximum difference of approximately six decibels

Comparing the numerical case to the LBM case shows less overlap for $\theta = 30, 60, 120, 150$. It should first of all be noted that this data is taken directly from the paper by Ribeiro et al. [29]. Since other data covers the taken data, small errors could be induced by interpolating the data. Additionally, it was readily known that the LBM does not predict the high-frequency decay of the spectra well. Since the higher frequencies are more likely to direct noise downstream, see the cardioid in Figure 2.2, it makes sense that the SPL from the LBM is biased towards the trailing edge. Within that work, they also took the FW-H surface as the whole foil such that the dipole would be biased towards $\theta = 0$ degrees as well. The combination of these should explain the discrepancies in Figure 5.15.

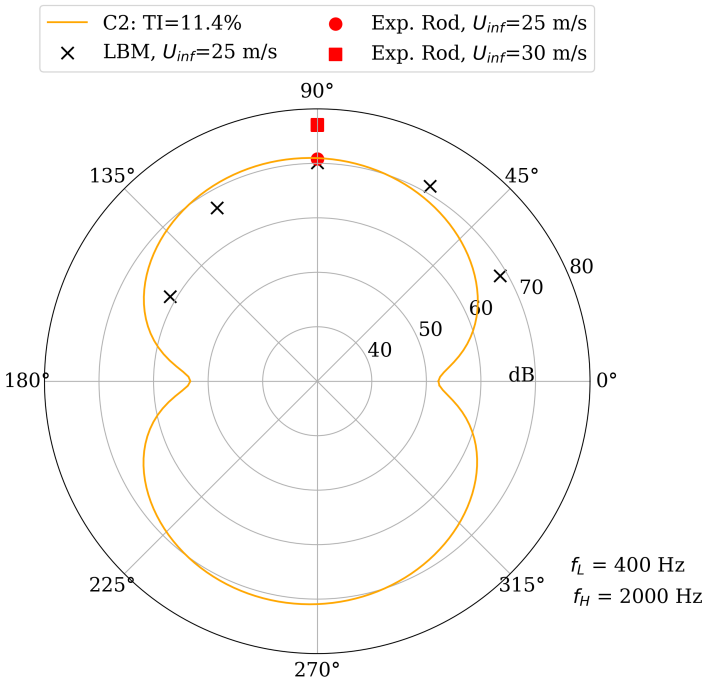

Figure 5.15: Sound pressure level for different receivers for numerical validation, LBM [29] and experimental [26] cases. f_l and f_h signify the lower and upper bound for the SPL integration, respectively.

To conclude, within this chapter the turbulence parameters with and without the foil have been validated showing similar values to experimental data. Coherence and pressure data have been validated and were used to determine the lower bound of PSD integrations as well as the upper bound for the FW-H surface. The numerical results seem to overpredict the wall pressure when moving along the chord of the foil, resulting in increased noise predictions. The latter has been validated by comparison to experimental and numerical data such that the numerical method is accurate within six decibels. More importantly, based on both validation sets, it has been proven that the numerical methodology captures both the low and high-frequency trends of the far-field pressure fluctuations well. This is most important for the comparison in sound pressure level that will be made for different turbulence intensities in the next chapter.

6

Results of turbulence intensity cases

This chapter will present the results of four numerical cases with different turbulence intensities, of which one was readily used for the validation in Chapter 5. The chapter will have a similar structure to the previous chapter. First, in Section 6.1 a short description of the four cases will be given. Afterwards, the results of the turbulence intensity on the turbulence statistics without and with the foil will be presented in Sections 6.2 and 6.3, respectively. Results on coherence and pressure will be given in Section 6.4. Finally, the effects of turbulence intensity on the leading edge radiated noise will be shown in Section 6.5.

6.1. Turbulence intensity cases description

Four cases with different turbulence intensities are investigated. All cases follow the methodology as presented in Chapter 4. The only difference is the Reynolds stresses that are used as input in the controls of the inflow turbulence generator (ITG). The change of Reynolds stresses results in a change of body forces according to Equation 4.2. All other parameters of the ITG (integral length scale, amplification factor, thickness and size) were kept the same. Reynolds stresses were tuned in the empty domain until desired values were achieved at the intended location of the leading edge. Table 6.1 gives an overview of the four cases that will be evaluated in this chapter.

Table 6.1: Parameters of the four numerical turbulence intensity cases.

Parameter	**Symbol**	**Case 1**	**Case 2**	**Case 3**	**Case 4**
Label figures	N.A.	C1: TI=13.5%	C2: TI=11.4%	C3: TI=7.6%	C4: TI=4.1%
Foil type	N.A.	NACA0008			
Foil chord [m]	c	0.3			
Foil span [m]	d	0.2			
Foil leading edge radius [mm]	r_{LE}	2.1			
Foil maximum thickness [mm]	t_{max}	24			
Turbulence generation	N.A.	Synthetic body forces, see Section 4.2			
Turbulence intensity [%] At $x/c = 0$ in empty domain	$TI = u_{rms}/\overline{u}$	13.5	11.4	7.6	4.1
Inflow velocity [m/s]	U_{inf}	25.26			

6.2. Inflow turbulence without the foil

Figure 6.1 shows a render of the four simulations without the foil present. The nondimensionalized spanwise vorticity clearly shows a decrease aligning with the decrease in turbulence intensity. One can also observe increased decay for the higher turbulence intensity cases, this will be highlighted later on as well.

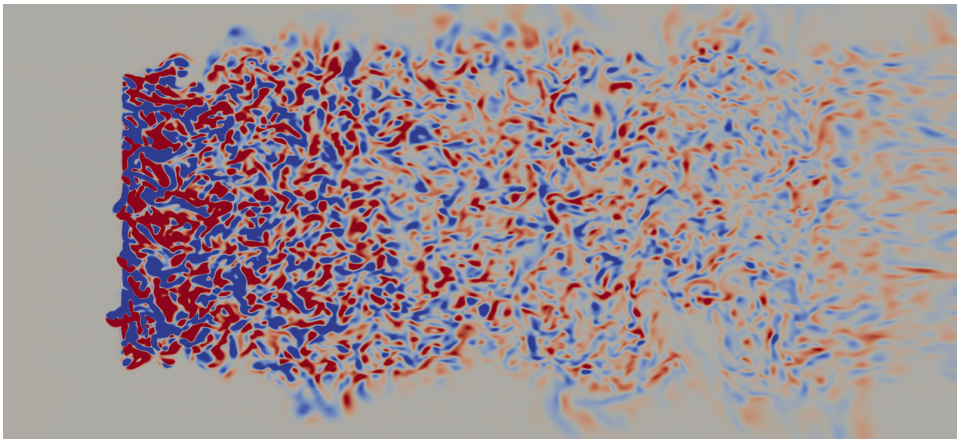

(a) C1: TI=13.5%.

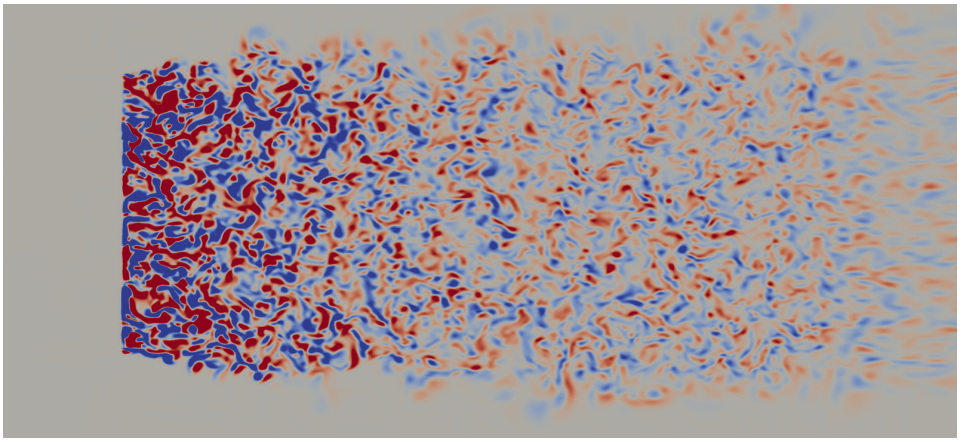

(b) C2: TI=11.4%.

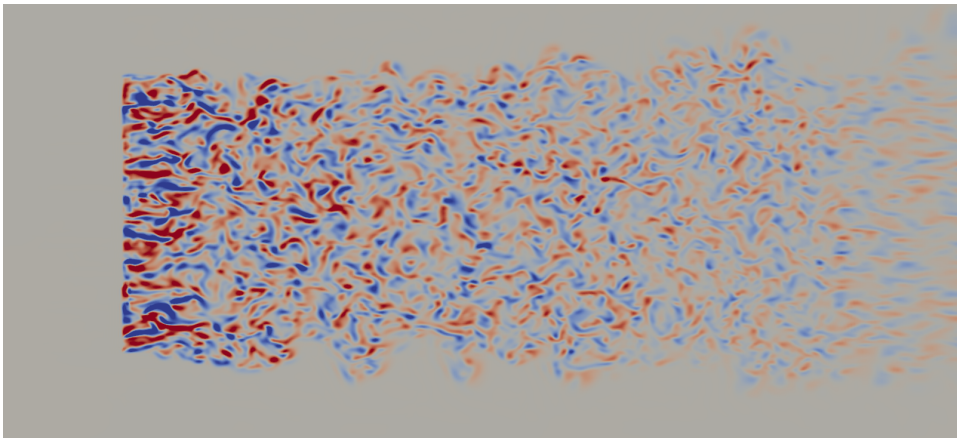

(c) C3: TI=7.6%.

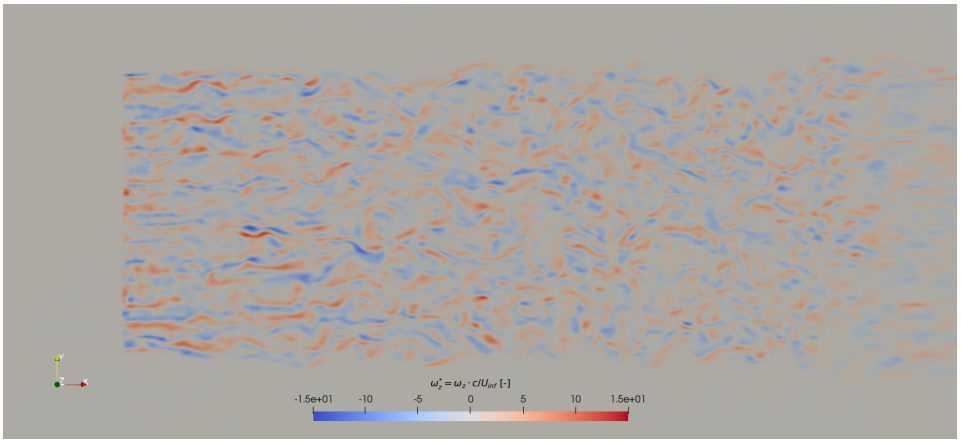

(d) C4: TI=4.1%.

Figure 6.1: Instantaneous spanwise vorticity as a visualisation of the four numerical cases with different turbulence intensities. The slice is taken at midspan of the foil.

Again, similar to the validation, the first step is to analyse the results of the inflow turbulence without the foil present. The transient scanning analysis (TSA), as explained in Section 4.5.1, was applied to all four cases. The results of the TSA for the streamwise velocity at the intended leading edge and midspan can be seen in Figure 6.2. The TSA returns different start-up times for the four cases. The lowest turbulence intensity, case C4, has the least start-up effects, whereas case C3 has the largest. Cases C1 and C2 show similar start-up times. The results of the TSA are used throughout this chapter. Similar to the validation chapter, it is only overruled for the integral length scale computation. There, the discarded time is set at 0.284 s, which includes turbulence convection up to the (intended) leading edge and at least one hundred flow troughs of the intended integral length scale (50 mm). The different outcomes of the TSA will mainly impact the outcomes of the PSD for the low-frequency range and the uncertainty estimates, as introduced in Section 4.5.4. The increase of local instantaneous streamwise velocity in Figure 6.2 is already indicative of an increase in turbulence intensity.

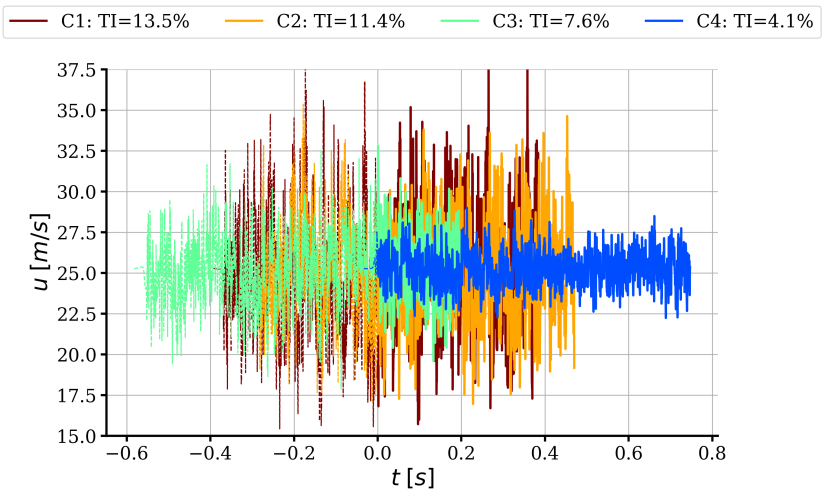

Figure 6.2: Numerical results of the transient scanning analysis applied to the local streamwise velocity u at $x/c = 0$ and midspan. The dashed part of the signal is flagged as the initial transient and is removed from the results.

The outcomes of the TSA are used to quantify the turbulence statistics. Figure 6.3a shows the RMS of the three velocity components for each of the four cases. A clear peak in fluctuations is seen directly after the ITG. The magnitude of the peak seems to be related to the Reynolds stresses prescribed on the ITG. Case C4 has the lowest Reynolds stresses and accordingly the lowest peak in the RMS of the velocity, whereas the opposite is true for case C1. This peak is then, in turn, linked to the decay behaviour of the turbulence throughout the domain. Case C4 shows the lowest decay, whereas case C1 decays rapidly after the ITG. The decay close to the ITG is not problematic as long as the decay has levelled out when moving close to the intended leading edge ($x/c = 0$). Otherwise, the assumption of homogenous turbulence needed for the integral length scale calculation will not hold. From Figure 6.3a, and its detailed view, it becomes clear that cases C2, C3 and C4 have decayed sufficiently to become homogenous. Case C1, however, is still decaying after reaching the intended leading edge. Although slight, this will likely influence the results in the remainder of this section as well. For future analysis, it is desired to either move the ITG further upstream or the foil further downstream.

From the detailed view in Figure 6.3a, it also becomes clear that the turbulence becomes less isotropic when increasing the turbulence intensity. Cases C3 and C4 show good overlap at $x/c = 0$, while cases C1 and C2 show less favourable results. Both cases show that w_{rms} decays less rapidly than v_{rms}. Close to the ITG this is not seen, meaning that the development over the domain induces these differences. The size of the domain in the flow (x) direction is much larger compared to the vertical direction (y). The latter is, in turn, larger than the spanwise (z) direction. The relative sizes of the domain aligns with the development of their respective velocity fluctuations throughout the domain.

Figure 6.3b present the development of the turbulence intensity over the domain. The turbulence intensity is calculated based on the local mean and RMS of the streamwise velocity. This version, over all three RMS components, was deliberately chosen since it became clear from Section 3.3.1 that the radiated noise mostly depends on the streamwise velocity fluctuations. Again, a clear peak

close to the ITG is seen which follows from the peak in velocity fluctuations readily described. Decay behaviour throughout the domain is also similar to what was described previously. The detailed view of Figure 6.3b shows that the turbulence intensity has developed to a constant state, which is beneficial for the acoustic analysis. The case labels as introduced in Table 6.1 were determined from Figure 6.3b at $x/c = 0$.

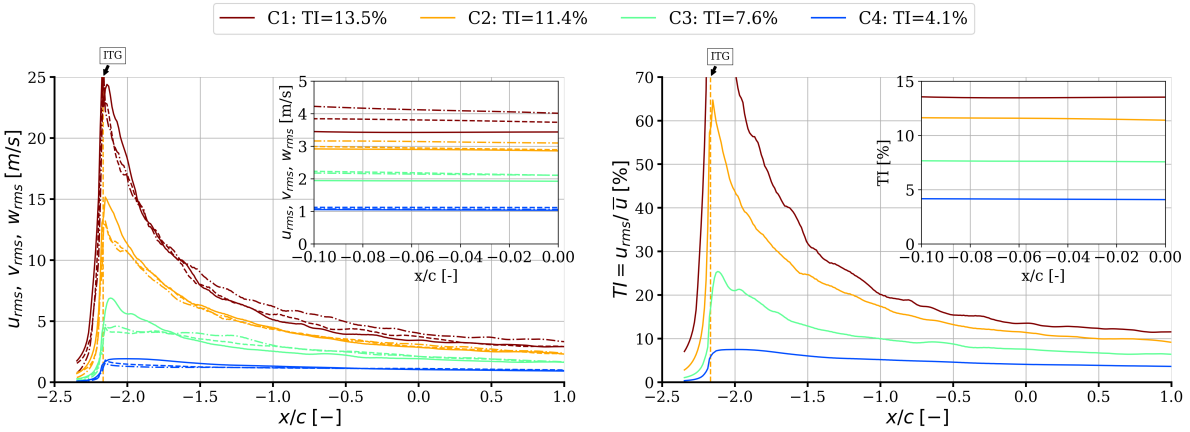

(a) Root-mean-square of velocity fluctuations u_{rms} (——), v_{rms} (- - -) and w_{rms} (-·-·).

(b) Turbulence Intensity (TI) based on local mean streamwise velocity.

Figure 6.3: Velocity fluctuations (a) and turbulence intensity (b) over the domain at midspan for the numerical cases. The vertical orange line represents the location of the inflow turbulence generator (ITG).

Figure 6.4 shows the development of the local mean streamwise velocity normalised by the set inflow velocity (equal for all four cases) at midspan over the domain. All four cases experience a velocity decrease or increase when going past the ITG. The relative size of this increase or decrease is again related to the turbulence intensity. All of the simulations recover the velocity increase or decrease well before reaching the intended leading edge, indicating that the turbulence intensity from Figure 6.3b is dominated by the change in velocity fluctuations.

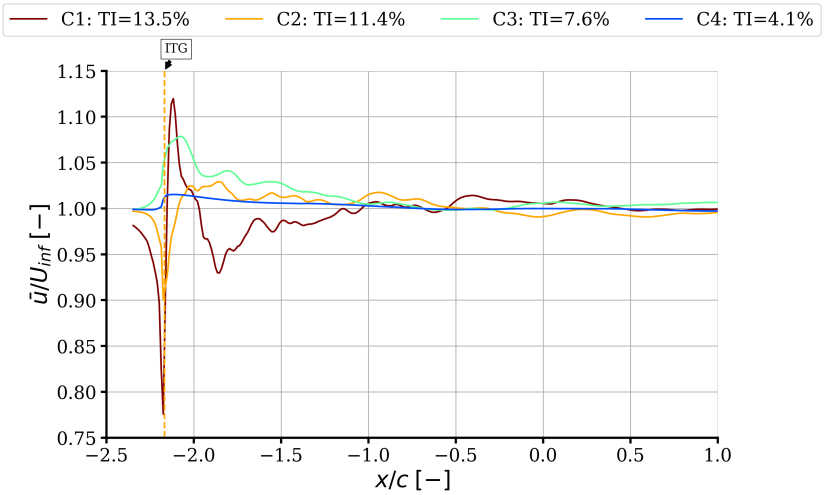

Figure 6.4: Mean streamwise velocity component over the domain at midspan for the numerical cases. The y-axis is normalised by the set inflow velocity.

Figure 6.3a already gave some information about the isotropy of the cases. To further explore this, the relations between fluctuations over time are analysed. Figures 6.5a and 6.5b show the relations of the fluctuations $u'v'$ and $u'w'$ over time, respectively. For clarity, the fluctuations have been plotted for every five time steps rather than every single one. What mainly stands out is that the spread of the fluctuations significantly increases when the turbulence intensity increases. The two highest cases

C1 and C2 seem to be stretched more in Figure 6.5b, signifying that the ratio $w_{rms} : u_{rms}$ is not 1:1. This was readily visible in the RMS of the velocity fluctuations. Nonetheless, it is difficult to retrieve correlations from Figure 6.5 visually, so the Pearson correlation has been calculated for each simulation. Table 6.2 shows the Pearson correlations and p-values for the numerical validation case at $x/c = 0$ and midspan. Although unexpected, all Pearson correlation values show no clear linear relation between the fluctuations while still being statistically significant based on the p-values. This contradicts the statement of isotropy from Figure 6.3a. The calculation of the Pearson correlation has, however, been applied to the whole data signal returned by the TSA. It is, therefore, less likely to find correlations that occur within short segments of the signal. The turbulence can, for example, be anisotropic for a part of the signal which is dampened out in the Pearson correlation by taking the whole signal. Correlations for shorter signals were not calculated since a comparison of the PSDs to the Von Kármán spectrum will be made as well.

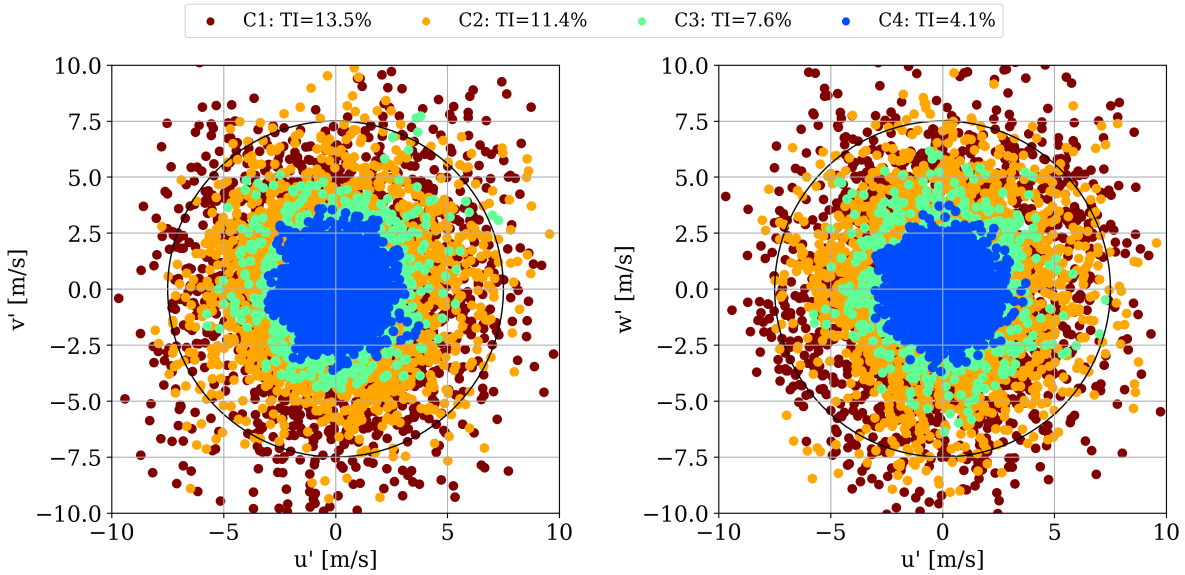

(a) Relation of $u'v'$.

(b) Relation of $u'w'$.

Figure 6.5: Relations of velocity fluctuations at $x/c = 0$ and midspan for the numerical cases. The circle is plotted as a reference representing isotropic behaviour for which the Pearson correlation goes to zero.

Table 6.2: Pearson correlation and p-values for the numerical cases. Correlation and p-value are shown for $u'v'$ and $u'w'$.

Case	Pearson correlation $u'v'$ [-]	p-value $u'v'$ [-]	Pearson correlation $u'w'$ [-]	p-value $u'w'$ [-]
C1	1.67E-02	8.11E-02	4.85E-02	4.39E-07
C2	1.96E-02	2.42E-02	1.77E-02	4.23E-02
C3	6.37E-02	2.03E-06	-3.47E-02	9.65E-03
C4	-3.74E-02	5.79E-08	-2.16E-02	1.76E-03

The mean decidecade band power density and several other parameters for the numerical cases are plotted in Figure 6.6. The uncertainty is estimated based on Equation 4.11. Several observations can be made. First, cases C2 and C3 show big fluctuations for $10 < f < 70$ Hz. Additionally, case C3 shows no data for $10 < f < 16$ Hz. These effects are both induced by the rather short time signal used to calculate the PSD and mean decidecade band power density. This is in line with the outcome of the TSA as seen in Figure 6.2, where case C3 has a much shorter accepted signal resulting in the absence of data for low frequencies in Figure 6.6. Although undesired, it does not influence the analysis of this work since the high-frequency range is of interest.

Second, all cases show increasingly poorer overlap with the Von Kármán spectrum for increasing turbulence intensity. All cases show reasonable overlap with the Von Kármán spectrum for $60 < f < 200$ Hz. For $f > 200$ Hz the overlap becomes progressively worse for increasing turbulence intensity. This is indicative of increased anisotropic turbulence, which is supported by the statements made previously. It should, however, be noted that the Von Kármán spectrum is heavily dependent on its inputs. Both the velocity and RMS of the fluctuations are well defined at $x/c = 0$, but the integral length scale is known to be problematic. That is why a comparison to the $f^{-5/3}$ power law is also valuable. All four cases show similar slopes compared to the visualised power law for $250 < f < 1300$ Hz, indicating that all four cases show similar levels of isotropy.

Finally, the estimated mesh cut-off frequency is similar for cases C1, C2 and C3. Case C4, however, loses energy about 300 Hz before the estimated mesh cut-off. The lower turbulence intensity should (partially) induce this effect, but the difference between cases C4-C3 is much more than between cases C3-C2, while the drop in turbulence intensity is similar. There is likely another effect which forces case C4 to dissipate energy faster, or that causes less energy to be put into the system over the whole frequency range in general. The latter is more likely since it was readily proven in Section 5.1 that the high-frequency decay for case C2 is accurate compared to experimental values. All other cases (C1, C3 and C4) show, apart from the energy levels, similar decay behaviour, making it more likely that too little energy is resolved by case C4. More arguments for this hypothesis will be given later on.

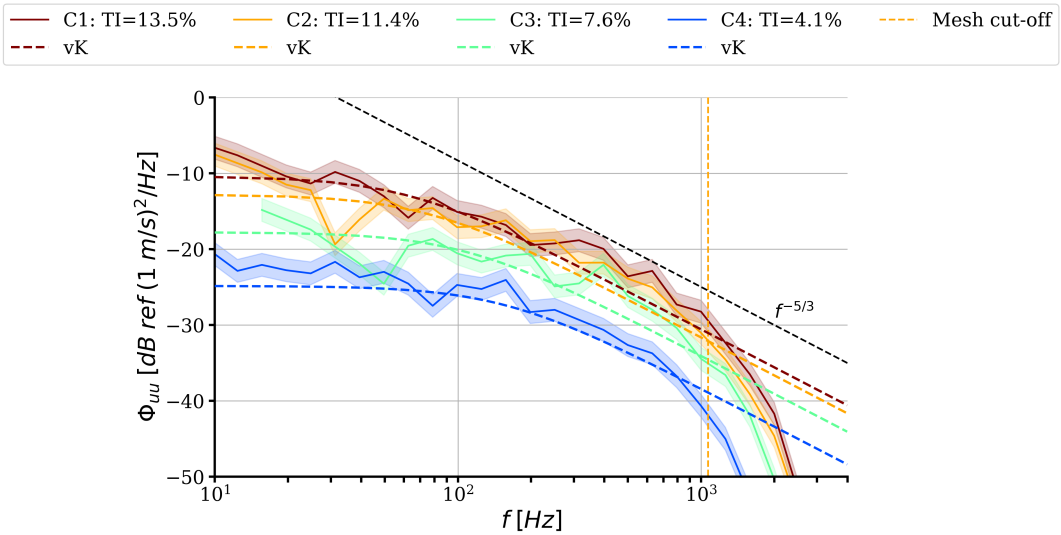

Figure 6.6: Mean decidecade band power density, Von Kármán (vK, see Equation 3.3) and uncertainty bands of the streamwise velocity component at $x/c = 0$ and midspan for the numerical cases.

Figure 6.7 shows the integral length scale over the domain at midspan for the four numerical cases. Only the fitting method, as explained in Section 4.3, is included. This method has readily proven useful by removing the highly fluctuating behaviour of the length scale while still predicting the integral length scale accurately (although slightly conservative). The zero-crossing method showed similar results for cases C1, C3 and C4. Case C2 showed bigger deviations, which has readily been adressed in the previous chapter. From Figure 6.7, one can observe a coupling between the turbulence intensity and the integral length scale. Close after the ITG the turbulence is not yet homogeneous, rendering the length scale results unrealistic. The large integral length scales in front of the ITG are also unrealistic since no turbulence has yet been introduced. The autocorrelation of such a signal will always be correlated for a long time since there are no distortions. Only from $x/c > -0.5$ is the turbulence (close to) homogeneous for all cases. From there, one can observe an increase of the integral length scale for increasing turbulence intensity. The zero-crossing method confirms these results. It was desired to decouple the two as explained in Section 2.2. However, since Section 5.1 showed that more accurate control over the length scale is not feasible, corrections should be applied to acoustic data to determine the effect of the integral length scale on the generated sound.

Figure 6.7 shows that cases C1, C2 and C3 rapidly decay after the ITG while further in the domain the integral length scale increases. Case C4 contradicts this by decaying less rapidly close to the ITG. It also does not increase throughout the domain, which all other cases do. This could be (one of) the reasons why the spectrum in Figure 6.6 shows lower energy levels for that case. The integral length scale at $x/c = 0$ for case C4 is approximately 22 mm. Assuming that eight cells are needed for accurately resolving the length scale, a maximum cell size of 2.75 mm would be required. The average cell size between the ITG and the intended leading edge is approximately two millimetres. Even though the integral length scale can thus be resolved, it could still mean that the solver switches to modelling the turbulence rather than resolving it for slightly smaller length scales. This aligns with the modelled stress depletion, as introduced in Section 3.1.2, which is known to affect IDDES. This switch induces less energy being put into the system. The low integral length scale can thus negatively affect the energy levels captured by the solver. No attempt was made to solve the problem since it is a direct effect of the lower turbulence intensity, showing a potential pitfall to the use of the current setup.

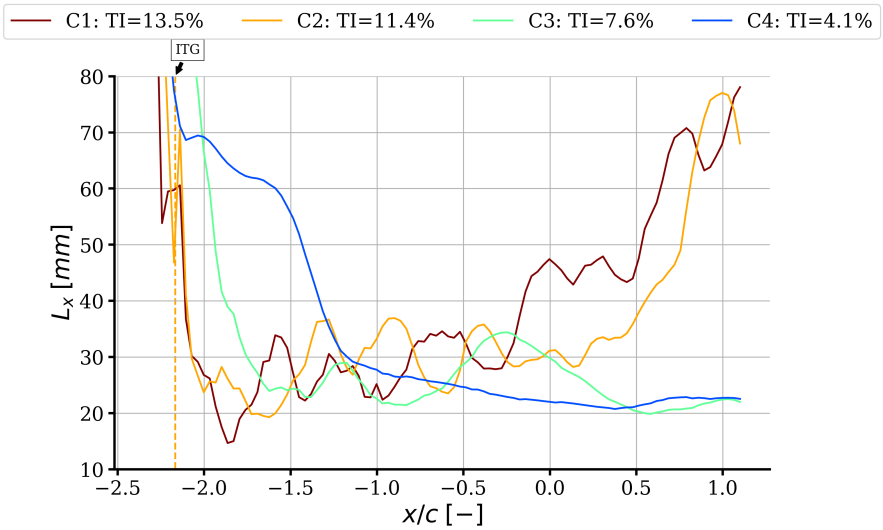

Figure 6.7: Integral length scale over the domain at midspan for the numerical cases. Only results from the fitting procedure are visualised.

To conclude, four numerical cases with varying turbulence intensity have been introduced. The turbulence intensity, and hence fluctuations, show realistic behaviour when moving from the ITG to the leading edge. Unrealistic behaviour of the integral length scale due to inhomogeneous turbulence is found close to the ITG. The lowest turbulence intensity case generates integral length scales for which the solver likely switches from resolving to modelling these, thereby losing energy as input to the spectrum. Spectra show realistic decay behaviour for higher frequencies, whereas data for the low-frequency range is not trustworthy due to the limited signal duration. The next section will discuss the inflow turbulence for the different cases when the foil is present.

6.3. Inflow turbulence with the foil

Figure 6.8 shows a render of the four simulations with the foil present. Similar to those shown before, one can clearly observe a link between the nondimensionalized vorticity and the decay with the turbulence intensity.

Analysis of the inflow turbulence with the foil present is conducted similarly as was done for the validation case. Again, all data is normalised unless stated otherwise. The normalisation point is taken at $x/r_{LE} = -47$, which was proven to be the first point where the normalised velocity reached a plateau as seen from the leading edge, see Section 5.2. Figure 6.9 presents the normalised local mean streamwise velocity over the domain. All four cases show excellent overlap when approaching the leading edge. Only a slight difference is visible in Figure 6.9b. That difference is likely induced by the normalisation procedure, which takes a value depending on each case. The slight difference of $\overline{u}_\infty$ at $x/r_{LE} = -47$ likely induces the minor difference seen in Figure 6.9b.

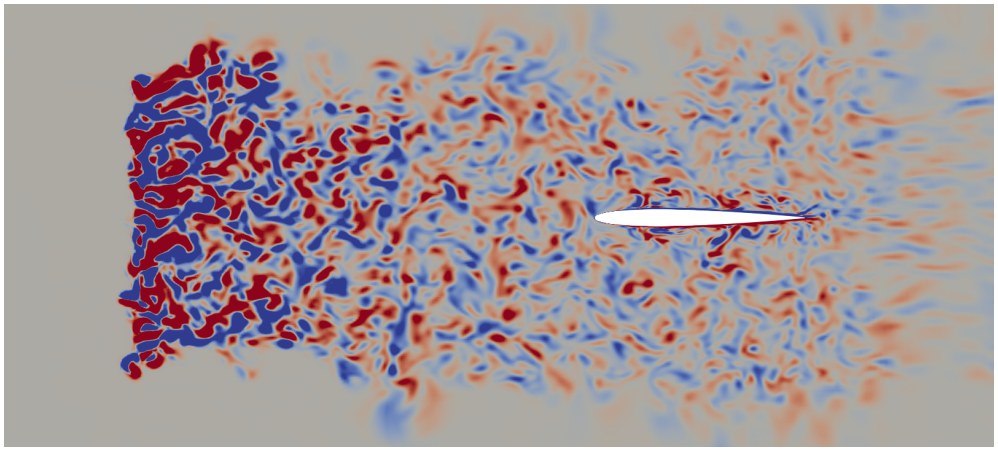

(a) C1: TI=13.5%.

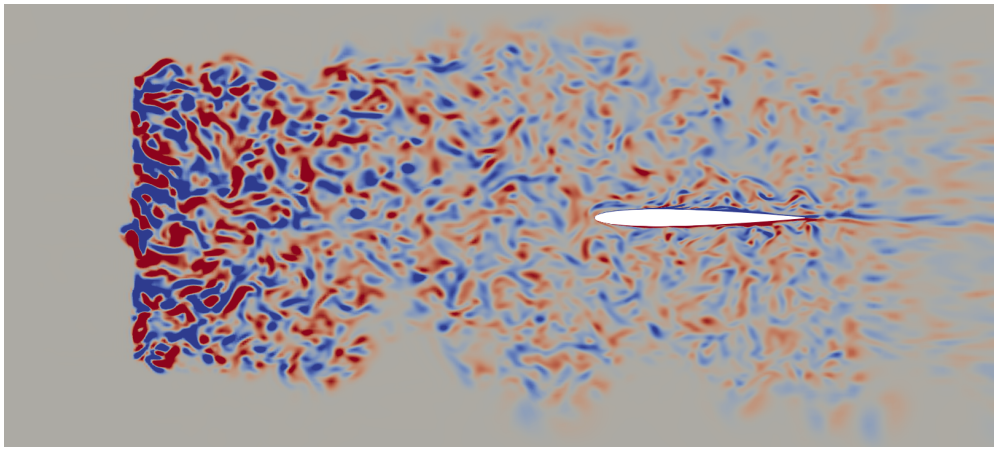

(b) C2: TI=11.4%.

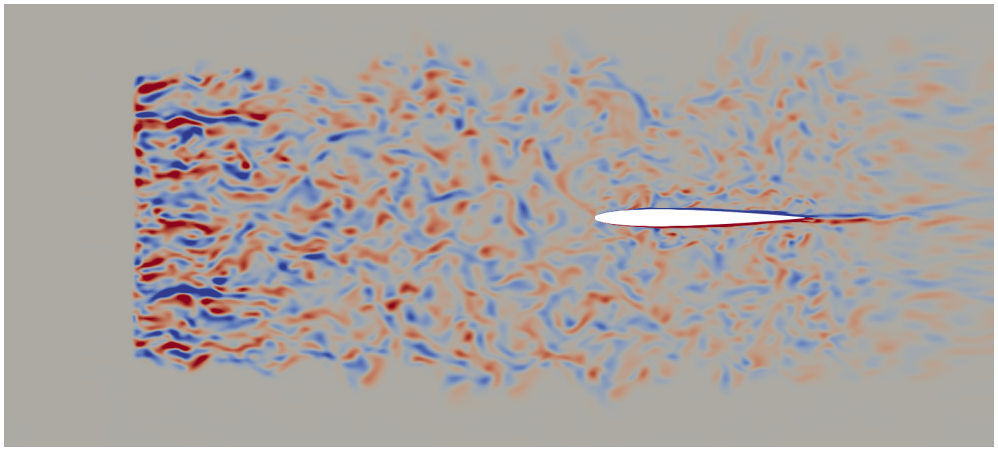

(c) C3: TI=7.6%.

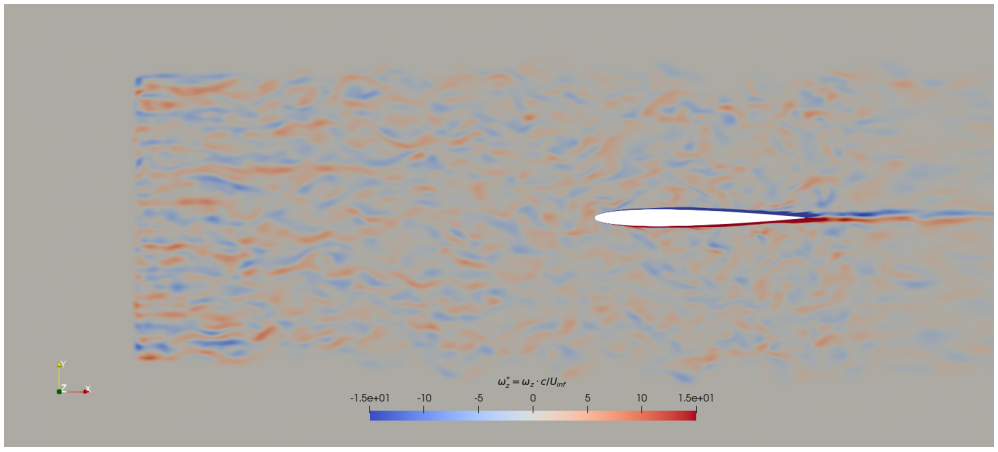

(d) C4: TI=4.1%.

Figure 6.8: Instantaneous spanwise vorticity as a visualisation of the four numerical cases with different turbulence intensities. The slice is taken at midspan of the foil.

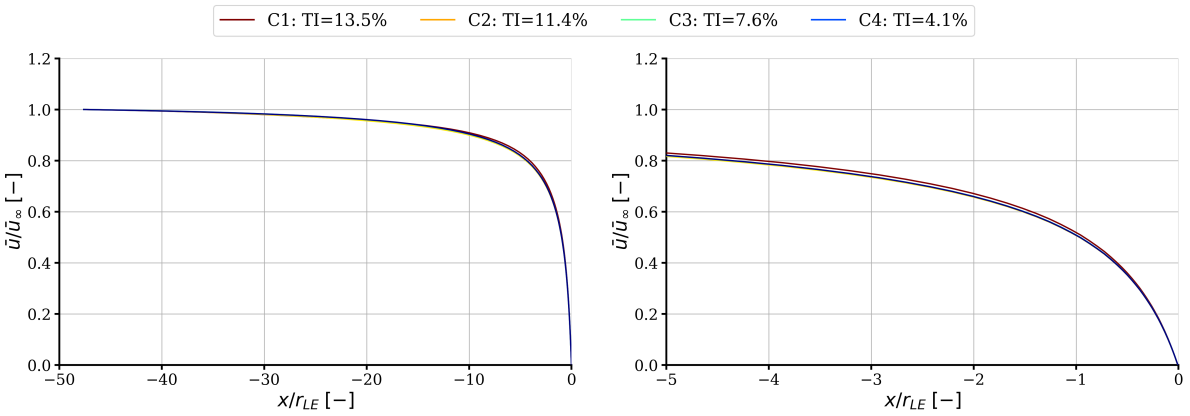

(a) Normalisation taken at $\frac{x}{r_{LE}} = -47$.

(b) Detailed view of (a), normalisation taken at $\frac{x}{r_{LE}} = -47$.

Figure 6.9: Normalised mean local streamwise velocity over the domain for the numerical cases. The y-axis is normalised by the streamwise velocity at the specified location in the sub-caption.

The results for the normalisation of the RMS of the streamwise velocity fluctuations and a detailed view close to the leading edge can be seen in Figures 6.10a and 6.10b, respectively. Normalisation is taken at the same position as the velocity normalisation to make a fair comparison between results. It can be observed that there is little to no overlap between the four cases, apart from really close to the leading edge. Cases C2 and C3 correspond well, whereas cases C1 and C4 deviate much more. Case C1 seems to feel the presence of the foil much earlier, which makes sense since it has much more energy contained in its eddies approaching the leading edge. The exact opposite reasoning also holds as to why case C4 can advect closer to the leading edge before being influenced by the foil. This hypothesis is in line with the integral length scale as presented in Figure 6.7. Cases C2 and C3 have similar length scales at $x/c = 0$ and, therefore, show similar decays for the RMS. Case C1 has a much bigger length scale, which will 'hit' the leading edge from further upstream, thereby losing its energy earlier. Case C4 has a smaller length scale and can thus advect closer to the leading edge before it must also lose its energy.

It should, however, be noted that the experimental data from Figure 5.8a does not confirm this hypothesis. The rod-generated turbulence has, compared to grid-generated, bigger integral length scales and higher (streamwise) velocity fluctuations. Nonetheless, the decay behaviour of the streamwise RMS of the velocity fluctuations is the same for both cases while the current hypothesis predicts that the rod-generated turbulence should decay earlier.

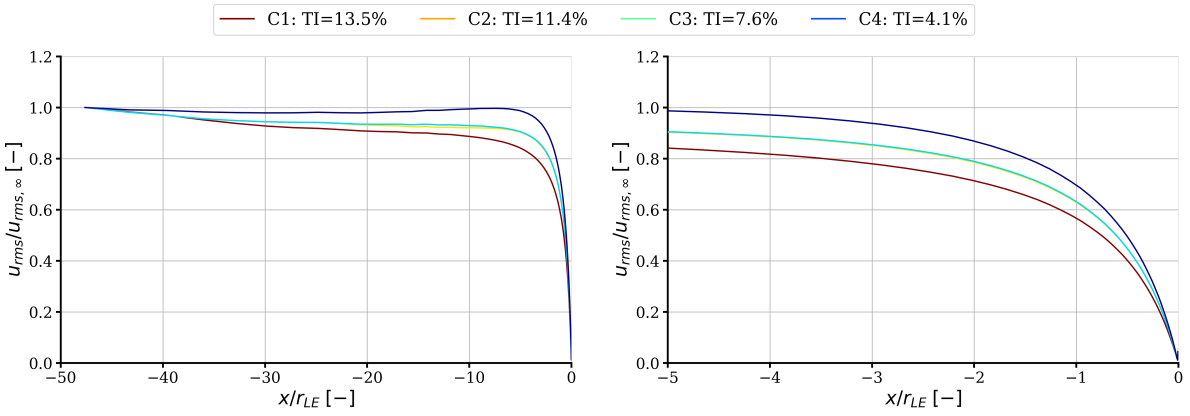

(a) Normalisation taken at $\frac{x}{r_{LE}} = -47$.

(b) Detailed view of (a), normalisation taken at $\frac{x}{r_{LE}} = -47$.

Figure 6.10: Normalised root-mean-square velocity fluctuations over the domain for the numerical cases. The y-axis is normalised by the value at the specified location in the sub-caption.

Since the previous line of reasoning does not seem to (solely) hold, two other effects must also be discussed. It has already been determined that for case C4 the turbulence might not be sufficiently resolved. The poor resolution of the turbulence could be why less energy is put into that solution. This could also affect the decay of the RMS, such that a lower energy content can move closer to the leading edge. It is hard, if not impossible, to separate this effect from the effect previously introduced (assuming that it is present). These two reasons could explain why case C4 can move much closer to the leading edge before decaying.

Second, the faster decay of case C1 might be due to the natural decay of the turbulence intensity in the domain. Figure 6.11 presents the turbulence intensity based on the inflow speed for three different probes:

- Probe 1 is located on the stagnation line midspan of the foil. Its data points are exponentially divided such that the distance between them decreases when moving closer to the leading edge. It allows for data analysis close to the leading edge;
- Probe 2 is located on the stagnation line midspan of the foil. Its data points are linearly spread such that the distance between them is equal. It does not allow for data analysis close to the leading edge but is meant for data analyses in the bulk of the flow between the ITG and the foil;
- Probe 3 is located above the foil ($y/t_{max} = 6.67$) at midspan. Its data points are linearly spread such that the distance between them is equal and the same as Probe 2. It allows for data analysis in the freestream behind the ITG so that it does not feel the influence of the airfoil.

It becomes clear that for case C1 the turbulence is still rapidly decaying for probes 1 and 2, whereas this effect is less for cases C2, C3 and C4. This natural decay will influence the normalisation of Figure 6.10. To conclude the analysis of Figure 6.10, three combined effects play a part in the decay behaviour when approaching the leading edge: the poor resolution of the turbulence for the smaller length scale (case C4); the difference in integral length scale for all four cases; and the natural decay of the turbulence intensity (case C1). The overall decay behaviour for the three cases looks good in combination with these three effects and therefore no effort is made to separate or quantify these effects or to improve the results.

Two more observations can be made based on Figure 6.11. First, there is a difference between the turbulence intensity on the stagnation line (Probes 1 and 2) and above the foil in the freestream (Probe 3). This difference becomes larger for increased turbulence intensity. This is a logical effect based on how the ITG has been defined. Body forces are uniformly prescribed on the ITG grid. Turbulence generated from the centre of the grid has less space to decay energy to. Turbulence generated near the top/bottom edge of the ITG can distribute its energy into the freestream where no turbulence is generated. Furthermore, the turbulence near the stagnation line is going to interact more with one another than that near the edge of the ITG. These two effects will play a bigger effect for higher turbulence intensities explaining the differences between the cases.

Second, the turbulence intensity levels on the stagnation line (Probes 1 and 2) do not match well with the turbulence intensity levels in the empty domain, as seen in Figure 6.3b. Again, the results match less for higher turbulence intensity cases. This is a direct consequence of the two runs performed on different meshes. The cases without the foil have been performed on a finer mesh. The validation still holds for the no-foil and foil cases since those have been performed separately. The main importance is that any acoustic evaluation based on turbulence intensity should be performed with the turbulence intensity taken from Figure 6.11.

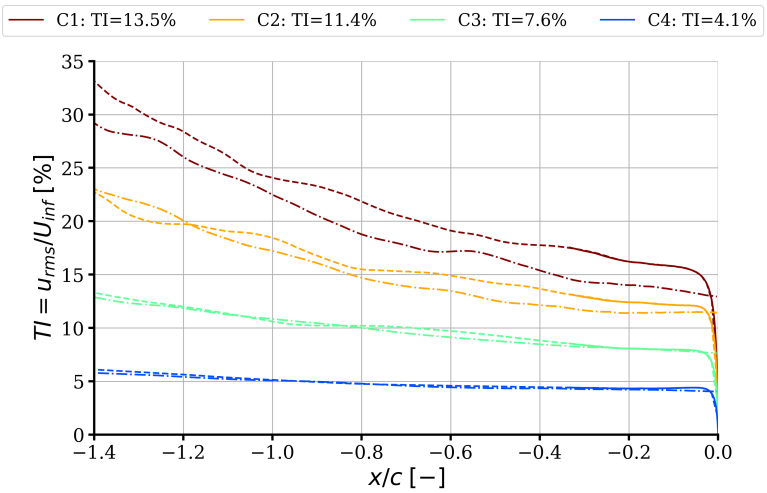

Figure 6.11: Turbulence intensity over the domain at midspan for the numerical cases. Probes 1 (——), 2 (- - -), and 3 (-·-·) have been defined in the text.

The final part of the turbulence evaluation for the four cases is to look at the integral length scale when approaching the leading edge. Figure 6.12a shows the integral length scale from the fitting method normalised at $x/r_{LE} = -20$. Reasons for these choices have readily been presented in Section 5.2. For $x/r_{LE} < -20$ cases C2, C3 and C4 show similar tendencies. Case C1, however, substantially deviates. Closer to the leading edge, $x/r_{LE} > -20$, the four cases do show similarities, although levels do deviate. What stands out most is that case C2 decays slower than case C3, although the integral length scale upstream is bigger for case C2, see Figure 6.12b. This contradicts the reasoning given earlier in this section, which stated that the RMS of the streamwise velocity fluctuation decays faster for larger length scales.

Forging conclusions from the normalised values is difficult since there is also the natural behaviour of the integral length scale throughout the domain. It is, therefore, also useful to look at the values which have not been normalised, see Figure 6.12b. It again becomes clear that there is a coupling between the integral length scale and turbulence intensity, although no clear formulation for this relationship can be made based on Figure 6.12b. Furthermore, cases C2, C3 and C4 show realistic behaviour when approaching the leading edge and further upstream. Case C1, however, presents strange behaviour when moving further upstream. This also explains the difference in normalisation that was readily found. It is possible that the decay of case C1 for $x/r_{LE} < -20$ is due to the interaction with the foil but the current results cannot confirm nor deny that hypothesis. Since more accurate control over the integral length scale is not possible, see Section 5.1, the results are left as are. Similar to the turbulence intensity, the integral length scale might differ due to the difference in meshes. Therefore, any evaluation of acoustic data will be performed with the integral length scale from Figure 6.12b.

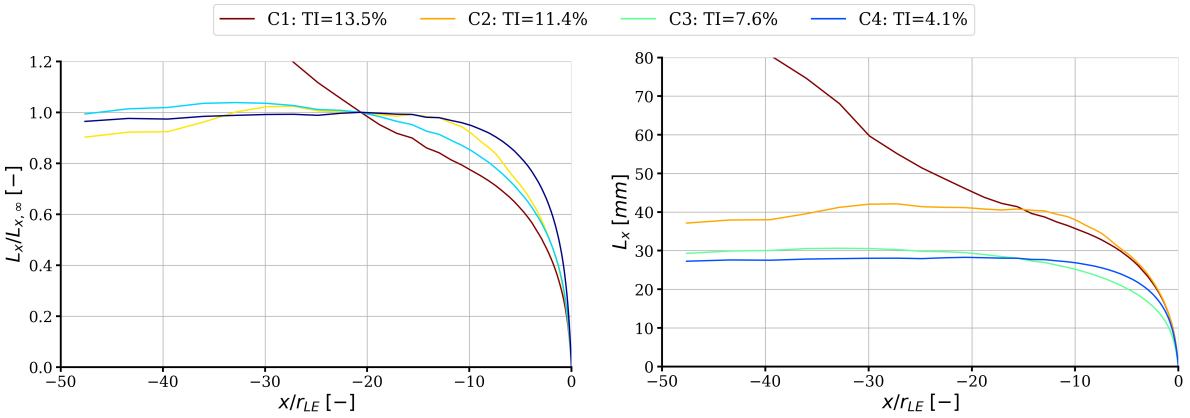

(a) Normalisation taken at $\frac{x}{r_{LE}} = -20$.

(b) No normalisation to the data is applied.

Figure 6.12: ntegral length scale over the domain at midspan for the numerical cases. Only data from the fitting method is presented. For (a) the y-axis is normalised by the value at the specified location in the sub-caption.

6.4. Coherence and pressure

In Section 5.3 the scaling for the limited span was investigated. It was concluded that an acoustic correction for case C2 can only be applied if the coherence length remains smaller than the span of the simulation. Even though a correction does not have to be applied for the numerical cases to be compared, it is desired to remove the low-frequency range for which it is known that $L_\gamma > d_{sim}$. This lower frequency range is likely interfering with the boundary conditions due to its large coherence length. To make the comparison between cases fair, a singular lower bound for all cases is preferred. It was readily proven for case C2 that a lower bound of 400 Hz is achievable. For this to be true for the other cases, it was required that for all simulations the following requirement holds $L_\gamma(f_{low} = 400\ Hz) < d_{sim}\ at\ x/c = 0.5$.

Figure 6.13 shows the coherence at $x/c = 0.5$ for the four different cases. It becomes clear that the coherence front reclines when going to lower turbulence intensities. Cases C2, C3 and C4 all show acceptable coherence levels for $f_{low} = 400$ Hz. Case C1, however, is on the verge of being in the increased coherence front. Figure 6.14 shows the coherence for that case at $x/c = 0.05$, i.e. much closer to the leading edge of the foil. Here the lower frequency bound is sufficiently high to be outside the coherence front. Note that the FW-H surface is defined until $x/c = 0.2$, such that the true lower bound should be chosen between Figures 6.14 and 6.13a. It is expected that this will result in the coherence front having moved sufficiently, such that the lower bound $f_{low} = 400$ Hz is acceptable. The lower bound will, therefore, be kept at $f_{low} = 400$ Hz for all four numerical cases.

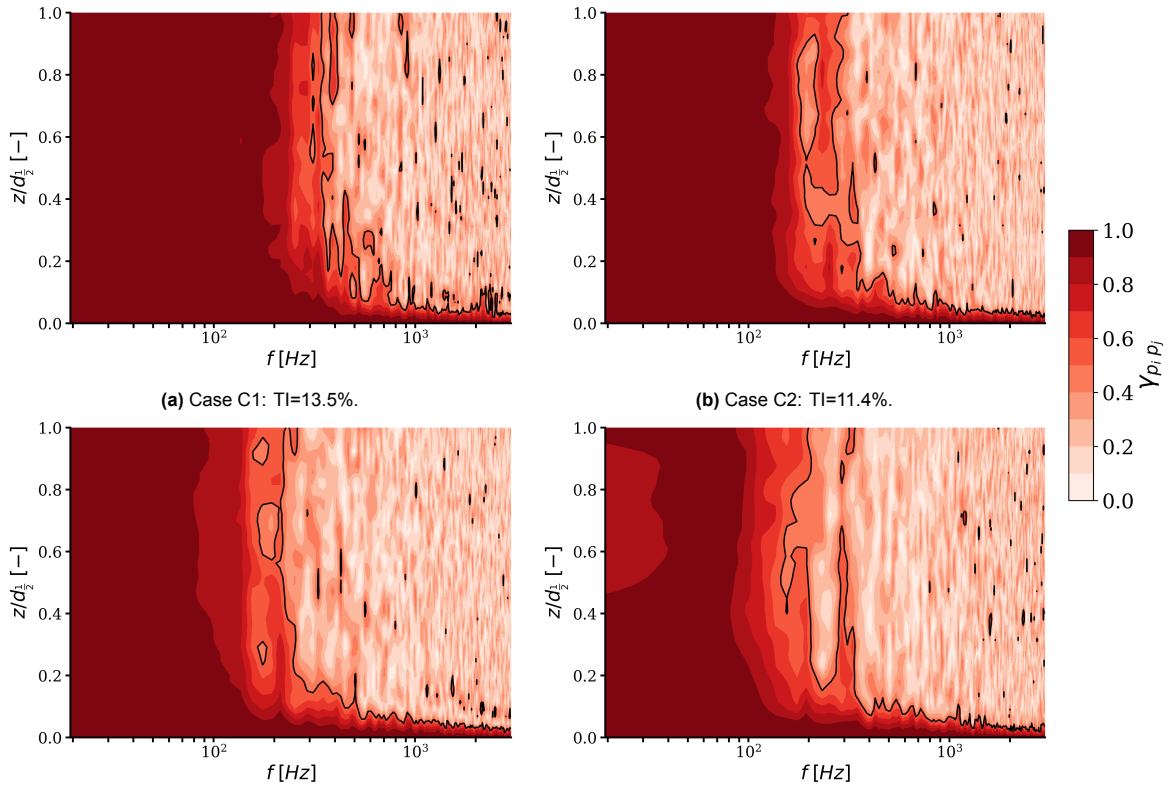

(a) Case C1: TI=13.5%.

(b) Case C2: TI=11.4%.

(c) Case C3: TI=7.6%.

(d) Case C4: TI=4.1%.

Figure 6.13: Spanwise coherence at $x/c = 0.5$ for the numerical cases. The reference for each coherence calculation is taken at midspan ($z/d_{\frac{1}{2}} = 0$) and the y-axis is made non-dimensional by the half span ($d_{\frac{1}{2}}$). The black contour line represents $\gamma_{p_i,p_i} = 0.5$.

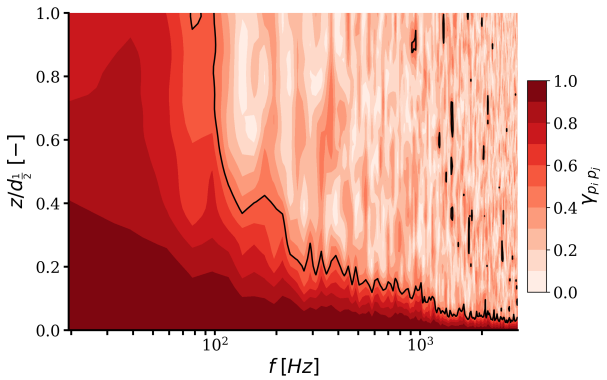

Figure 6.14: Spanwise coherence at $x/c = 0.05$ for the numerical case C1: TI=13.5%. The reference for the coherence calculation is taken at midspan ($z/d_{\frac{1}{2}} = 0$) and the y-axis is made non-dimensional by the half span ($d_{\frac{1}{2}}$). The black contour line represents $\gamma_{p_i,p_i} = 0.5$.

Besides the lower integration bound, the size of the solid FW-H data surface is also kept constant, i.e. up to $x/c = 0.2$. Figure 6.15 shows the RMS of the wall pressure at midspan over the foil. Several observations can be made. First, the used definition of the FW-H surfaces captures the 'effect' of the leading edge for all cases well. Only case C1 has not levelled out entirely. On the other hand, cases C3 and C4 level out much earlier towards the leading edge. Both observations could result in different definitions of the FW-H surface. The best way to overcome this problem, readily introduced in Section 5.3, is to divide the FW-H surface into strips. The far-field noise of each strip can then be calculated and the 'effect' on the total far-field noise can be determined. This will remove the impact of the user-defined choice for the FW-H surface, assuming that the strip furthest downstream is chosen such that the RMS of the wall pressure has levelled out for all of the cases. This adaption was not possible within the current work. To keep the comparison between cases as fair as possible, it was decided to retain the FW-H surface until $x/c = 0.2$ throughout the remainder of this work.

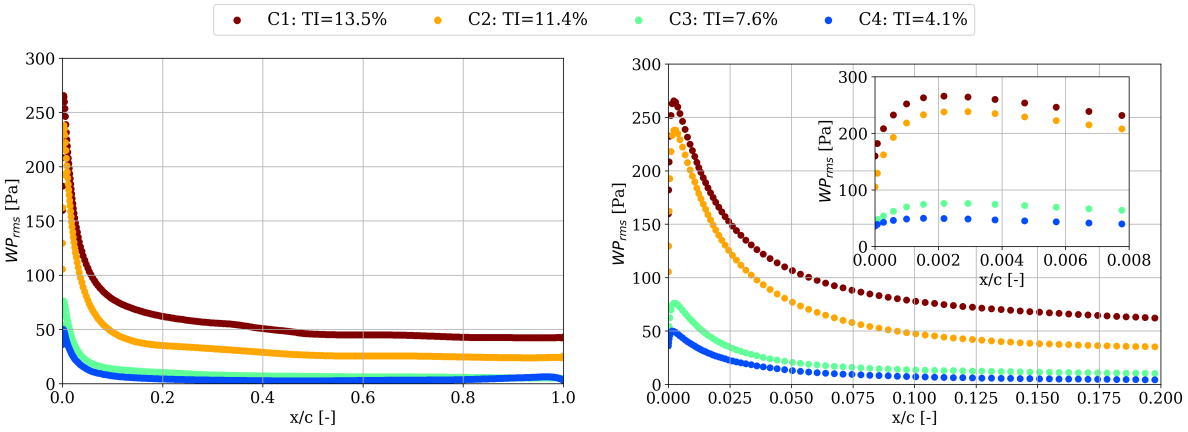

(a) Full chord.

(b) Detailed view of (a) showing data closer to the leading edge.

Figure 6.15: Root-mean-square of the wall pressure over the foil at midspan for the numerical cases.

From Figure 6.15, it also becomes clear that there is a relation between the turbulence intensity and the wall pressure. An increase in turbulence intensity leads to an increase in wall pressure (fluctuations). There does, however, not seem to be a clear parameter for which this relation scales. The spectra of the wall pressure fluctuations could explain the difference. Figure 6.16 shows the spectra for the four cases at two locations along the foil. The difference between cases C1, C2 and C3 are in line with the difference in turbulence intensity of those cases for $f > 100$ Hz, as shown in Figure 6.16a. However, for $f < 100$ Hz the difference between those three cases no longer seems straightforward. Cases C1 and C2 show similar energy levels, whereas case C3 significantly lacks energy. The energy for lower frequency is likely overestimated for cases C1 and C2. The latter also became apparent by comparison with experimental results, as done in Section 5.3. This overestimation of energy also leads to increased levels of the wall pressure RMS. It was readily shown that the coherence increases

when moving along the chord of the foil. For the line of reasoning to hold, it is expected that the wall pressure difference between the four cases also increases. Figure 6.16b indeed shows this. Case C4 has dropped the most for $f < 100$ Hz, whereas the other cases show a lesser energy drop. This is similar to the coherence levels which, further down the foil, are lower for the C4. This emphasises why a choice for the lower bound of acoustic data integration is needed.

In Figure 6.16b it also becomes clear that the overall energy level for case C4 is much lower, even for $f > 100$ Hz. This was readily attributed to the poor resolution of the turbulence for this case. It is likely, based on the pressure on the foil, that the acoustics will, therefore, also be significantly underpredicted.

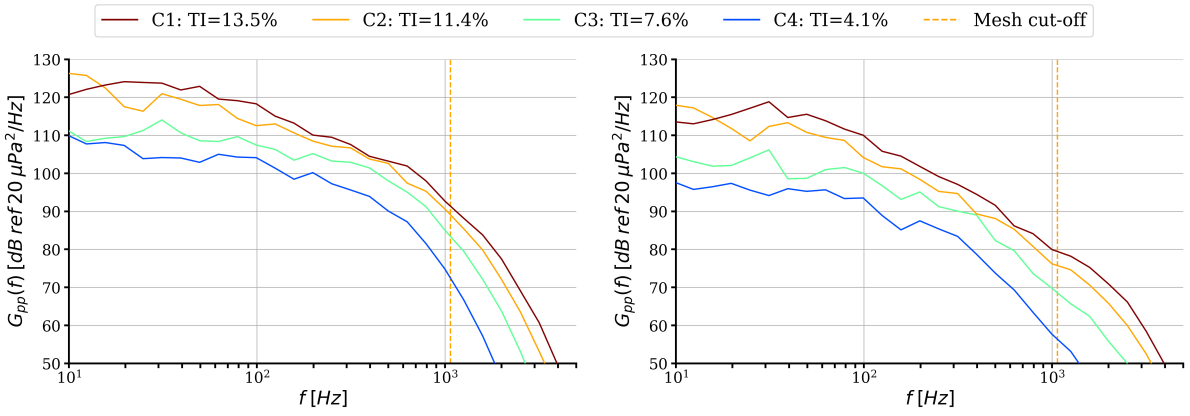

(a) $x/c = 0.0035$. **(b)** $x/c = 0.05$.

Figure 6.16: Mean decidecade band power density of the wall pressure fluctuations at midspan for different chordwise positions for the numerical cases.

6.5. Far-field acoustics

At last, the acoustic results can be evaluated. Figure 6.17 shows the far-field noise spectra for the four numerical cases for receivers at $\theta = 90, 180$ degrees. Note that the y-axis have different limits for the two figures. Several observations can be made, most of which have readily become clear from previous results. For $\theta = 90$ degrees and $f < 2000$ Hz, cases C1, C2 and C3 show similar differences and decay behaviour. Case C4 shows far-field energy levels much lower than expected, which is in line with results previously shown. This also holds for $\theta = 180$ degrees. For $f > 2000$ Hz cases C1, C3 and C4 all level out, whereas case C2 keeps decaying further (before levelling out). It is likely that the mesh is not able to resolve the turbulence for these higher frequencies, i.e. the estimated mesh cut-off frequency is much lower. This highlights the importance of having an upper boundary for integration of the spectra such that numerical noise is removed from the SPL levels. The lower bound for integration was readily validated in the previous section. The upper bound, as determined in Section 5.4, of $f_{high} = 2000$ Hz is acceptable for integration of all cases. Only case C4 shows slight undesirable levels near that frequency. The energy levels are, however, much smaller for those frequencies ($SPL < 0$ dB), such that integration of that portion of the signal does not influence the results. All other receiver angles showed spectra with shapes and levels in between Figures 6.17a and 6.17b.

It is also valuable to compare the two different receiver locations. Two things stand out. First, the shape of the spectra differs substantially. For $\theta = 180$ degrees the spectra lose energy for lower frequencies. This is in line with the theory as presented in Section 2.2 and Figure 2.2, which stated that bigger length scales (lower frequencies) direct sound less efficiently in that direction. Second, the differences between the cases in Figure 6.17b is much more than in Figure 6.17a. Additionally, case C1 only loses about 10 dB, whereas case C4 loses 20 to 30 dB when moving from 90 to 180 degrees. This contradicts the statement made about the dipole directivity. It becomes clear from the data that the increase of turbulence intensity, by which energy is added to higher frequencies as well, dominates over the decrease in integral length scale. In other words, cases C1, C2 and C3 drop less when moving from 90 to 180 degrees due to the increase in turbulence intensity. This aligns with the statements made about case C4, which showed lower energy levels. Directional plots will, therefore, be biased towards the dipole directivity for integration between 400 Hz and 2000 Hz, irrespective of the length scale.

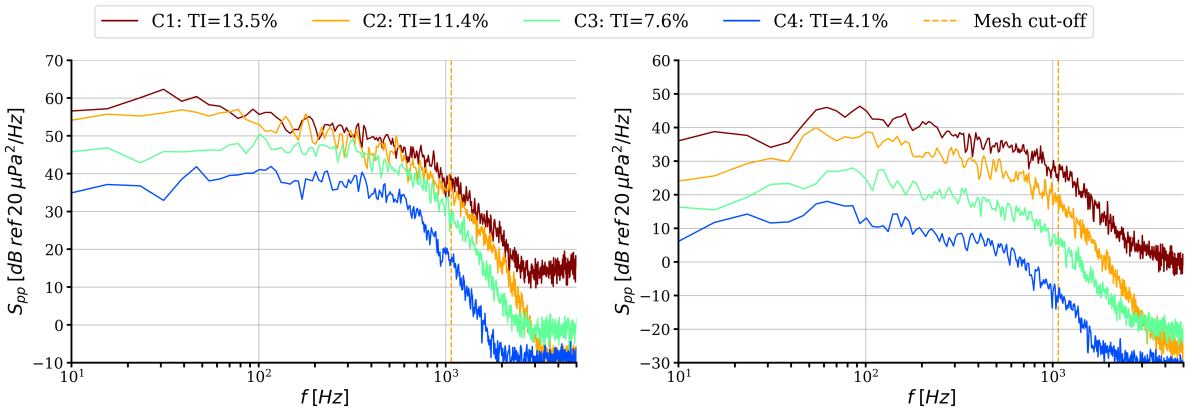

(a) $\theta = 90$ degrees. **(b)** $\theta = 180$ degrees.

Figure 6.17: Power spectral density of the far-field noise for the numerical cases at two different receiver locations. Numerical cases are corrected for limited span.

Figure 6.18 shows such a polar plot of the SPL. Differences in levels are in line with the results readily presented. The key takeaway should, again, be the much faster increase in SPL for receiver angles that are more on the stagnation line, i.e. $\theta \approx 0$ degrees and $\theta \approx 180$ degrees. It should, however, be noted that the choice of radial axis (dB) significantly influences the data representation in a polar plot. It is, therefore, better to present the data in a different format.

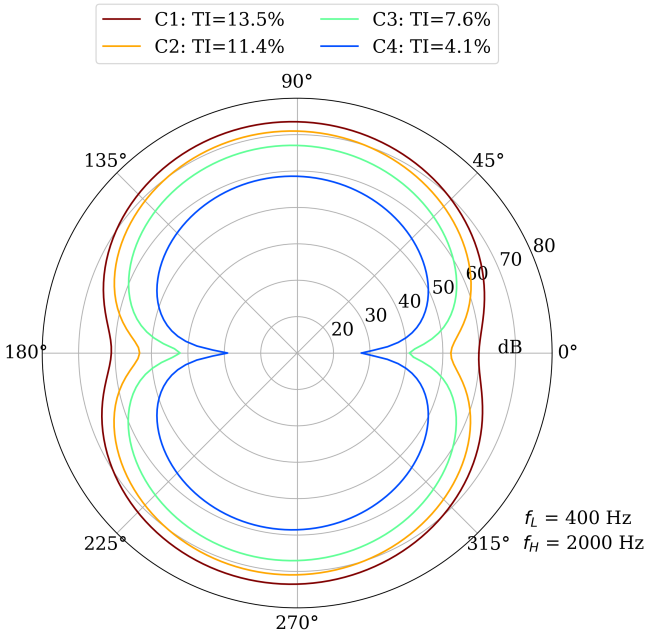

Figure 6.18: Sound pressure level for different receivers for the numerical cases. f_l and f_h signify the lower and upper bound for the SPL integration, respectively.

Figure 6.19 shows the sound pressure level for different receiver angles against the turbulence intensity for the different numerical cases. The SPL values have been retrieved by integrating the mean decidecade band power density, as explained in Section 4.5.2. The turbulence intensity for the four numerical cases is taken from Probe 1 of Figure 6.11 at $x/c = -0.2$. This point represents the first point upstream of the foil where the foil has not influenced the flow yet, such that this is 'the true' turbulence intensity that the foil experiences. This is confirmed by Figure 6.9a, which shows that the mean local streamwise velocity has barely started to decay at $x/c = -0.2 \rightarrow x/r_{LE} \approx -30$. The Amiet curves represent the predicted increase of SPL for an increase of u_{rms}. Equation 3.1 readily showed that the power spectral density of the far-field pressure fluctuations increases quadratically for a linear increase of velocity fluctuations, i.e. $G_{pp} \propto u_{rms}^2$. Under the assumption that the turbulence intensity is not a

function of the velocity, this can be rewritten to $G_{pp} \propto TI^2$. This was readily confirmed by Figures 6.4 and 6.9. Plotting such a relation on a log-log scale, as done in Figure 6.19, leads to a linear relation since $log(a^b) = b \cdot log(a)$. The starting points for the Amiet scaling are arbitrarily chosen and do not represent an actual outcome of the Amiet theory.

Fits through the data are only performed for cases C1, C2 and C3 since it was readily proven that case C4 contains errors induced by the solver. Fitting is performed using the curve-fit procedure from the scipy.optimize library in Python. The baseline curve to fit was chosen as

$$SPL(TI) = a + 10 \cdot log_{10}(TI^b), \tag{6.1}$$

where a and b are coefficients determined by the fitting procedure. For clarity, data is only presented for the quadrant $0 \leq \theta \leq 90$ degrees. Similar results are, however, found for all three other quadrants.

From Figure 6.19, several observations can be made. First, it becomes clear that all receivers on a log-log plot show a linear increase of SPL for a linear increase of TI. This is readily what Amiet predicted as well. The efficiency, or slope, at which the increase happens is, however, heavily dependent on the receiver angle. A receiver at $\theta = 90$ degrees does see an increase of SPL, but only limited. On the other hand, a receiver at $\theta = 0$ degrees sees a much steeper increase of the SPL for the same increase of TI. Table 6.3 presents the coefficients of the fits. These coefficients represent the value b in Equation 6.1, thereby representing the relation $SPL = f(TI^b)$. Note that the coefficient as predicted by Amiet, independent of the receiver angle, is $b = 2$. It can be concluded that the scaling, as introduced by Amiet, is accurate for receiver angles closer to 90 degrees. The theory loses its usefulness for receiver angles closer to the stagnation line. This aligns with Amiet's assumption that the airfoil is a plate of negligible thickness, thereby losing any interaction effect of the foil. These interaction effects dominate for receiver angles on the stagnation line.

An uncertainty estimate of the numerical cases can quantify how accurate Amiet is. The uncertainty interval is calculated based on Equation 4.11, which, integrated over the frequency, will give a total uncertainty in decibels. The uncertainty for the numerical cases is 5.6 dB, meaning that the scaling as introduced by Amiet is accurate within 5.6 dB for receiver angles close to 90 degrees.

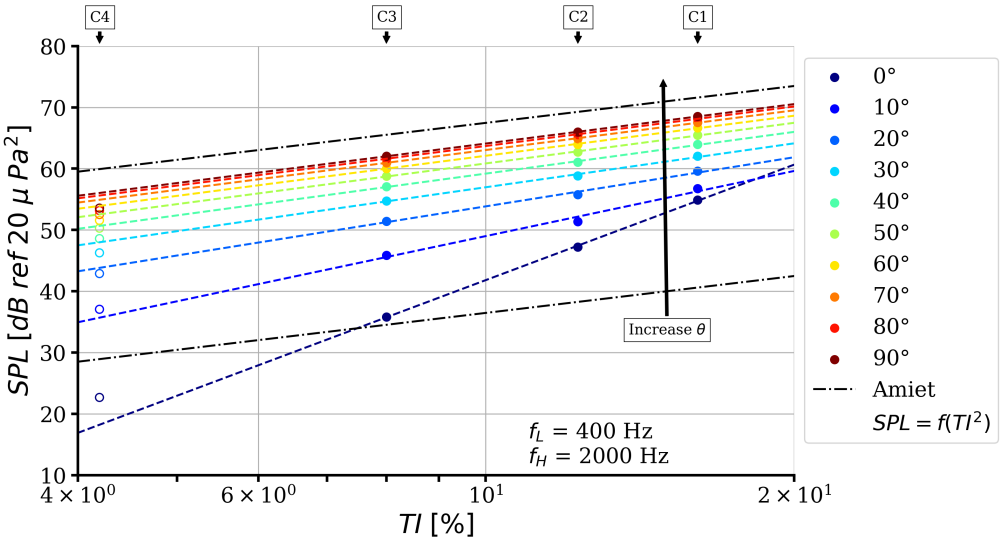

Figure 6.19: Sound pressure level (SPL) against turbulence intensity (TI) at different receiver angles for the numerical cases. The Amiet curve depicts the increase of SPL for a linear increase of TI. Dashed lines represent fits through the data points; hollow data points are excluded from the fits. f_l and f_h signify the lower and upper bound for the SPL integration, respectively.

Table 6.3: Fitting coefficients and coefficient of determination R^2 for different receiver angles.

Receiver angle θ [degrees]	0	10	20	30	40	50	60	70	80	90
Slope, fitting parameter b [-]	6.26	3.53	2.66	2.38	2.26	2.20	2.17	2.15	2.14	2.14
$R^2[-]$	1.000	0.984	0.991	0.996	0.998	0.999	0.999	1.000	1.000	1.000

The excellent fits in Figure 6.19 already indicate that the turbulence intensity is the dominant factor in the leading edge radiated noise. The coefficients of determination in Table 6.3 support the accuracy of these fits and this statement. To prove that the turbulence intensity is indeed dominant, an attempt is made to remove its effect. The reason for this is that several other variables might also affect the far-field radiated noise. One of these is the integral length scale, which is linked to the turbulence intensity as was readily proven in Sections 6.2 and 6.3. Such a confound [93, p. 119] can indirectly also influence the sound pressure level. Figure 6.20 gives an overview of different confounds that might influence the far-field noise. One can see the relationship between the integral length scale and the turbulence intensity, which might have an indirect effect on the SPL. The other way around may also be true, but results from this work cannot prove that statement. Figure 6.20 also highlights the dependence of the turbulence intensity and integral length scale on the mean local velocity. This should not be surprising as both relations were readily indicated by Equations 2.4 and 2.7. Additionally Equations 3.1 and 3.4 show that the flow speed also has an effect on the far-field radiated noise. Figures 6.4 and 6.9, however, showed that the difference in local mean speed is less than two percent at the (intended) leading edge. The confound mean speed is, therefore, not of importance. The variable denoted by Q resembles any other parameters (such as density, temperature, angle of attack, etc.) that have not been investigated in this research and, hence, remain constant. These should not affect the outcomes of the procedure.

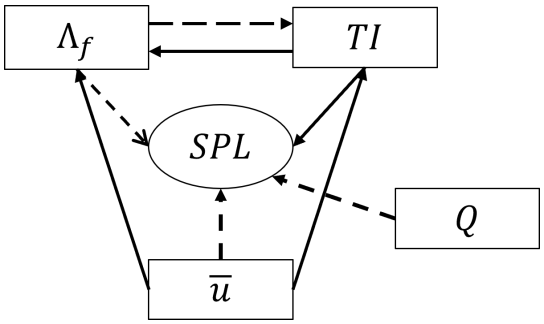

Figure 6.20: Relations between variables and their influence on the sound pressure level (SPL). Lines indicate a proven effect (——) and a possible effect (- - -). Q indicates all (constant) variables outside of this works scope.

McElreath [93, p. 119–164] proposes several methods to determine the effect of confounds. One is to fix the confound (integral length scale), which was proven unsuccessful with the current setup. The other is to perform a multivariate regression. Since the turbulence intensity and integral length scale are the only variables that can influence the far-field noise (see Figure 6.20), it is sufficient to prove that a change in SPL can be attributed to a change in turbulence intensity. This can be done by removing the effect of the turbulence intensity and showing that the results do not change for a change in the integral length scale. If so, the turbulence intensity is the only contributing factor to the SPL (at least in the range of values evaluated in this work).

To do so, a scaling similar to Equation 6.1 is applied. The scaling assumes case C2 as the baseline and scales all other cases based on the difference in turbulence intensity, which for equal velocities is the same as scaling for the difference in u_{rms}. Data is thus scaled by

$$SPL_{corrected} = SPL_{sim} + 10 \cdot log_{10}\left(\left(\frac{TI_{C2}}{TI_{Ci}}\right)^{b}\right), \tag{6.2}$$

with $i = 1, 2, 3, 4$ representing the numerical cases and b the fitting coefficient from Table 6.3. This correction thus scales case C2 by zero decibels, gives case C1 a negative scaling and cases C3 and C4 a positive scaling. The scaled results, now plotted against the integral length scale Λ_f, can be seen in Figure 6.21. The integral length scale for the numerical cases is taken from Figure 6.12b at the same position where the turbulence intensity was taken, i.e. $x/c = -0.2 \rightarrow x/r_{LE} \approx -30$. This was, of course, kept constant to allow for a fair interpretation of the results.

Cases C1, C2 and C3 and associated fits indeed indicate that for all receiver angles, the turbulence intensity is the dominant parameter for the SPL. If not, a trend should have been visible for the far-field noise as a function of the integral length scale. The range of integral length scales within this work (30 to 65 mm) does not seem to affect the far-field noise radiated from the leading edge of an airfoil.

It is, however, now valuable to also evaluate case C4. It has often been stated that the poor resolution of the turbulence for case C4 should also impact the far-field noise by underpredicting it. Figure 6.21 shows that the SPL is indeed underpredicted for most receiver angles. On the other hand, for $\theta = 0, 10$ degrees, the SPL is overestimated compared to the fits at those angles. This contradicts the previously made statement, but it is in line with the theory as presented in Section 2.2 and Figure 2.2. There it was explained that smaller integral length scales (hence higher frequencies) are more efficient in radiating sound in the direction of the stagnation line. This might dominate for observers on the stagnation line over the poorer resolution of turbulence by which less energy is put into the system. This could explain the overestimation for $\theta = 0, 10$ degrees, but it is impossible to say this for certain with the current range of integral length scales tested. It is, therefore, recommended for future work to put more effort into the separation of the turbulence intensity and integral length scale to accurately quantify the effects of both on the far-field radiated noise. The current setup only allows for accurate analysis of the turbulence intensity, as was done before. Additionally, future work should put effort into more accurate resolution of smaller length scales by adapting finer meshes. Based on the results presented in this section, the conclusion about the turbulence intensity being the dominant factor on the sound pressure level still holds.

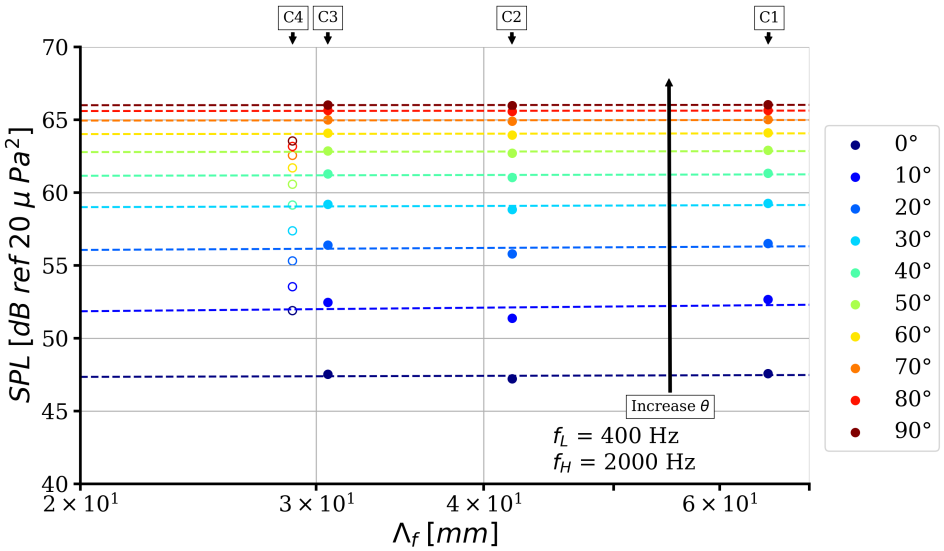

Figure 6.21: Sound pressure level (SPL) against the integral length scale (Λ_f) at different receiver angles for the numerical cases. Dashed lines represent fits through the data points; hollow data points are excluded from the fits. f_l and f_h signify the lower and upper bound for the SPL integration, respectively.

7

Conclusion

In this work, an attempt was made to address the research gap regarding airfoil leading edge radiated noise for varying inflow turbulence. To do so, a numerical framework within ReFRESCO was proposed to simulate the interaction between freestream turbulence and the leading edge of a NACA0008 airfoil. Turbulence was generated with a synthetic inflow turbulence generator (ITG). Turbulence was modelled using the improved delayed detached eddy simulations (IDDES) framework employing the $k-\omega$ model. This resulted in the solver switching between the large eddy simulations (LES) method in the bulk of the flow, to the Reynolds-averaged Navier-Stokes (RANS) method in the boundary layer of the foil. The Ffowcs Williams-Hawkings (FW-H) acoustic analogy with a solid data surface was used to predict far-field noise.

The application of body forces to the flow by the synthetic ITG proved to be computationally cheap and showed no adverse effects on requirements set for generated turbulence. The downside to this method is the inherent coupling of the integral length scale to the applied body forces and, hence, turbulence intensity. A study on the input parameters showed little to no control over the integral length scale. This should be improved by modifying the ITG such that integral length scales are not prescribed via body forces.

A new fitting procedure to the autocorrelation of the velocity fluctuations was proposed to calculate the integral length scale in the flow direction. The fitting procedure was validated by computing the integral length scale for experimental data. The fitting procedure can accurately predict the integral length scale by a maximum error of six percent. Numerical results of the fitting procedure show more deviation from other methods due to the much shorter duration of time signals within the simulation.

Inflow turbulence, as generated by the ITG, was validated by measurement data both with and without the foil present. Turbulence in the empty domain agrees reasonably well with experimental data regarding velocity fluctuations, turbulence intensity and energy spectra. The latter shows a maximum difference of five decibels when compared to the experimental spectra. A difference in the integral length scale is observed at the intended leading edge. This was deemed acceptable since more accurate control was impossible with the current setup.

Inflow turbulence with the foil shows excellent overlap between numerical and experimental data regarding mean velocity, velocity fluctuations and integral length scale when approaching the leading edge. Coherence and pressure data are used to determine the data surface for the FW-H computation and to set a lower frequency bound for acoustic data integration at 400 Hz. Coherence data shows an increase in coherence length when moving along the chord. Close to the leading edge, the surface pressure spectrum aligns well with experimental data for frequencies above 90 Hz, whereas lower frequencies are substantially overestimated. Moving along the chord results in an overestimation of the wall pressure spectra across the whole frequency range. The lower frequency bound partially resolves this problem, but acoustics data is also overestimated. Sound pressure levels from the FW-H analogy indeed show increased noise levels when compared to experiments. A good agreement of the far-field noise decay is found for frequencies between 400 and 2000 Hz, which is much higher than what is supposedly supported by the mesh.

Tuning of the turbulence intensity cases was done in the empty domain until desirable values were achieved. Turbulence intensity, with the foil present, varies between 4 % and 16 %. Results show an increase in integral length scale for increased turbulence intensity, as well as less isotropic turbulence. Since more accurate control over the length scale with the current setup was impossible, scaling of the acoustic data is applied. Velocity spectra show that the turbulence for the lowest turbulence intensity case is poorly resolved, leading to lower energy levels than expected. This is a direct result of the lower integral length scale in combination with the mesh. Turbulence parameters approaching the leading edge are, apart from the mean velocity, strongly dependent on the natural behaviour through the domain. Coherence and pressure data show favourable outcomes regarding the set lower frequency bound and the FW-H surface.

Sound pressure levels (SPL) from the FW-H analogy increase less rapidly for receivers above the foil ($\theta = 90$ degrees). In contrast, receivers down- ($\theta = 0$ degrees) and upstream ($\theta = 180$ degrees) of the foil experience a much steeper increase in SPL. A log-log plot of the SPL against turbulence intensity (TI) confirms this statement. Amiet proposed a scaling for the SPL based on the turbulence intensity of $SPL = f(TI^2)$, independent of the receiver angle. Numerical results of SPL show a similar scaling to Amiet, namely $SPL = f(TI^b)$ with $2.66 \leq b \leq 2.14$ for $20 \leq \theta \leq 90$ degrees with a numerical uncertainty of approximately five decibels. The Amiet framework loses accuracy for observers up- and downstream of the foil ($\theta \approx 180, 0$ degrees), for which numerical results predict the SPL to scale with TI to the power of six, i.e. $b \approx 6$. Scaling of SPL levels to remove turbulent intensity effects is performed. Results show that the researched integral length scale range does not affect the far-field radiated noise. This confirms that the change in turbulence intensity between 4 % and 16 % dominates over a change in the integral length scale from 30 mm to 65 mm.

8

Recommendations

This chapter provides several recommendations for work that can be performed based on the results presented in this report:

- **Analysis of different foil geometries**: It has been proven that the scaling for the turbulence intensity on far-field noise aligns with that predicted by Amiet. Only for receiver angles closer to the stagnation line does the scaling change rapidly. It would be most interesting for further works to investigate if the scaling from this work also applies to other foil geometries. If so, it significantly increases the robustness of such a scaling (in the initial design phase).

- **FW-H strip analysis:** It became clear that the correction applied to the acoustic data for the limited span is not only a function of the span and frequency but also of the coherence. Since the coherence, and thus coherence length, increases over the chord of the foil, a correction should be applied based on the chordwise position. The current setup, which used one solid FW-H data surface, returns only one value to the far-field. In future work, it is proposed that the FW-H surface be divided into equal strips along the chord. This allows for a correction to be applied at different chordwise positions. Additionally, such a division in strips also allows for allocating far-field noise sources to actual locations on the foil. This is likely a more accurate way to determine the actual effect of the leading edge than taking the RMS of the wall pressure fluctuations.

- **Improve artificial generation of turbulence (ITG):** It became clear that the integral length scale not only changed for a change in turbulence intensity but that all input parameters showed little to no control over it. This is likely a consequence of the implemented method, which only allows for the prescription of body forces. Further research should look into different turbulence generation approaches that can give the user more accurate control over the length scale. Ideally, an approach is implemented in which the integral length scale can be separately altered.

- **Improve low-frequency results:** It became clear that low-frequency results are predominantly influenced by the duration of the simulation and possibly the spanwise domain size, leading to low frequencies results being inaccurate. Further work is proposed to make the computational domain even wider and to let simulations run longer. Both should increase the reliability of the results, especially at lower frequencies (assuming that validation sets for low-frequency sound are available).

- **Improve small length scale results:** Results have shown that the energy of the lowest turbulence intensity case was substantially lower than the other cases, while an equal spread in turbulence intensity was realized. It is likely a consequence of the mesh together with the chosen turbulence modelling approach (IDDES). To investigate smaller length scales (under the assumption that a future ITG can generate those), a finer mesh or a different turbulence modelling approach has to be selected.

References

[1] D. Yelmanov, *Propeller and rudder of big ship underway view from underwater. Close up image detail of ship. Transportation industry. Ship repair, underwater survey and shipping business concept. Stock photo*, May 2019. [Online]. Available: https://www.istockphoto.com/photo/propeller-and-rudder-of-big-ship-underway-view-from-underwater-close-up-image-detail-gm1145708827-308470821.

[2] H. Slabbekoorn, N. Bouton, I. Van Opzeeland, A. Coers, C. Ten Cate, and A. N. Popper, "A noisy spring: The impact of globally rising underwater sound levels on fish," en, *Trends in Ecology & Evolution*, vol. 25, no. 7, pp. 419–427, Jul. 2010, ISSN: 01695347. DOI: 10.1016/j.tree.2010.04.005. [Online]. Available: https://linkinghub.elsevier.com/retrieve/pii/S0169534710000832.

[3] R. E. Kurt, H. Khalid, O. Turan, M. Houben, J. Bos, and I. H. Helvacioglu, "Towards human-oriented norms: Considering the effects of noise exposure on board ships," en, *Ocean Engineering*, vol. 120, pp. 101–107, Jul. 2016, ISSN: 00298018. DOI: 10.1016/j.oceaneng.2016.03.049. [Online]. Available: https://linkinghub.elsevier.com/retrieve/pii/S0029801816300129.

[4] M. C. Zwart, J. C. Dunn, P. J. McGowan, and M. J. Whittingham, "Wind farm noise suppresses territorial defense behavior in a songbird," en, *Behavioral Ecology*, vol. 27, no. 1, pp. 101–108, 2016, ISSN: 1045-2249, 1465-7279. DOI: 10.1093/beheco/arv128. [Online]. Available: https://academic.oup.com/beheco/article-lookup/doi/10.1093/beheco/arv128.

[5] H. Ö. Sertlek, H. Slabbekoorn, C. Ten Cate, and M. A. Ainslie, "Source specific sound mapping: Spatial, temporal and spectral distribution of sound in the Dutch North Sea," en, *Environmental Pollution*, vol. 247, pp. 1143–1157, Apr. 2019, ISSN: 02697491. DOI: 10.1016/j.envpol.2019.01.119. [Online]. Available: https://linkinghub.elsevier.com/retrieve/pii/S0269749118344932.

[6] F. Porté-Agel, Y.-T. Wu, H. Lu, and R. J. Conzemius, "Large-eddy simulation of atmospheric boundary layer flow through wind turbines and wind farms," en, *Journal of Wind Engineering and Industrial Aerodynamics*, vol. 99, no. 4, pp. 154–168, Apr. 2011, ISSN: 01676105. DOI: 10.1016/j.jweia.2011.01.011. [Online]. Available: https://linkinghub.elsevier.com/retrieve/pii/S0167610511000134.

[7] I. Sharland, "Sources of noise in axial flow fans," en, *Journal of Sound and Vibration*, vol. 1, no. 3, pp. 302–322, Jul. 1964, ISSN: 0022460X. DOI: 10.1016/0022-460X(64)90068-9. [Online]. Available: https://linkinghub.elsevier.com/retrieve/pii/0022460X64900689.

[8] B. Amirsalari and J. Rocha, "Recent Advances in Airfoil Self-Noise Passive Reduction," en, *Aerospace*, vol. 10, no. 9, p. 791, Sep. 2023, ISSN: 2226-4310. DOI: 10.3390/aerospace10090791. [Online]. Available: https://www.mdpi.com/2226-4310/10/9/791.

[9] J. Carlton, "Propeller Noise," en, in *Marine Propellers and Propulsion*, Elsevier, 2019, pp. 261–280, ISBN: 978-0-08-100366-4. DOI: 10.1016/B978-0-08-100366-4.00010-9. [Online]. Available: https://linkinghub.elsevier.com/retrieve/pii/B9780081003664000109.

[10] M. Liefvendahl and C. Troëng, "Simulation Based Analysis of the Hydrodynamics and Load Fluctuations of a Submarine Propeller Behind a Fully Appended Submarine Hull," en, Gothenburg, Aug. 2012. [Online]. Available: https://www.researchgate.net/profile/Mattias-Liefvendahl/publication/299599086_Simulation_Based_Analysis_of_the_Hydrodynamics_and_Load_Fluctuations_of_a_Submarine_Propeller_Behind_a_Fully_Appended_Submarine_Hull/links/57023c9608ae650a64f9372d/Simulation-Based-Analysis-of-the-Hydrodynamics-and-Load-Fluctuations-of-a-Submarine-Propeller-Behind-a-Fully-Appended-Submarine-Hull.pdf.

[11] C. Doolan and D. Moreau, *Flow Noise: Theory*, en. Singapore: Springer Nature Singapore, 2022, ISBN: 978-981-19248-3-5 978-981-19248-4-2. DOI: 10.1007/978-981-19-2484-2. [Online]. Available: https://link.springer.com/10.1007/978-981-19-2484-2.

[12] T. Von Karman and W. R. Sears, "Airfoil Theory for Non-Uniform Motion," en, *Journal of the Aeronautical Sciences*, vol. 5, no. 10, pp. 379–390, Aug. 1938, ISSN: 1936-9956. DOI: 10.2514/8.674. [Online]. Available: https://arc.aiaa.org/doi/10.2514/8.674.

[13] W. R. Sears, "Some Aspects of Non-Stationary Airfoil Theory and Its Practical Application," en, *Journal of the Aeronautical Sciences*, vol. 8, no. 3, pp. 104–108, Jan. 1941, ISSN: 1936-9956. DOI: 10.2514/8.10655. [Online]. Available: https://arc.aiaa.org/doi/10.2514/8.10655.

[14] J. M. R. Graham, "Similarity rules for thin aerofoils in non-stationary subsonic flows," en, *Journal of Fluid Mechanics*, vol. 43, no. 4, pp. 753–766, Oct. 1970, ISSN: 0022-1120, 1469-7645. DOI: 10.1017/S0022112070002719. [Online]. Available: https://www.cambridge.org/core/product/identifier/S0022112070002719/type/journal_article.

[15] C. Osborne, "Unsteady thin-airfoil theory for subsonic flow.," en, *AIAA Journal*, vol. 11, no. 2, pp. 205–209, Feb. 1973, ISSN: 0001-1452, 1533-385X. DOI: 10.2514/3.6730. [Online]. Available: https://arc.aiaa.org/doi/10.2514/3.6730.

[16] R. K. Amiet, "Compressibility Effects in Unsteady Thin-Airfoil Theory," en, *AIAA Journal*, vol. 12, no. 2, pp. 252–255, Feb. 1974, ISSN: 0001-1452, 1533-385X. DOI: 10.2514/3.49212. [Online]. Available: https://arc.aiaa.org/doi/10.2514/3.49212.

[17] R. Amiet, "Acoustic radiation from an airfoil in a turbulent stream," en, *Journal of Sound and Vibration*, vol. 41, no. 4, pp. 407–420, Aug. 1975, ISSN: 0022460X. DOI: 10.1016/S0022-460X(75)80105-2. [Online]. Available: https://linkinghub.elsevier.com/retrieve/pii/S0022460X75801052.

[18] J. C. R. Hunt, "A theory of turbulent flow round two-dimensional bluff bodies," en, *Journal of Fluid Mechanics*, vol. 61, no. 4, pp. 625–706, Dec. 1973, ISSN: 0022-1120, 1469-7645. DOI: 10.1017/S0022112073000893. [Online]. Available: https://www.cambridge.org/core/product/identifier/S0022112073000893/type/journal_article.

[19] W. J. Devenport, J. K. Staubs, and S. A. Glegg, "Sound radiation from real airfoils in turbulence," en, *Journal of Sound and Vibration*, vol. 329, no. 17, pp. 3470–3483, Aug. 2010, ISSN: 0022460X. DOI: 10.1016/j.jsv.2010.02.022. [Online]. Available: https://linkinghub.elsevier.com/retrieve/pii/S0022460X10001458.

[20] J. R. Gill, X. Zhang, and P. Joseph, "Effects of Real Airfoil Geometry on Leading Edge Gust Interaction Noise," en, in *19th AIAA/CEAS Aeroacoustics Conference*, Berlin, Germany: American Institute of Aeronautics and Astronautics, May 2013, ISBN: 978-1-62410-213-4. DOI: 10.2514/6.2013-2203. [Online]. Available: https://arc.aiaa.org/doi/10.2514/6.2013-2203.

[21] J. Gill, X. Zhang, and P. Joseph, "Symmetric airfoil geometry effects on leading edge noise," en, *The Journal of the Acoustical Society of America*, vol. 134, no. 4, pp. 2669–2680, Oct. 2013, ISSN: 0001-4966, 1520-8524. DOI: 10.1121/1.4818769. [Online]. Available: https://pubs.aip.org/jasa/article/134/4/2669/897953/Symmetric-airfoil-geometry-effects-on-leading-edge.

[22] T. Hainaut, G. Gabard, and V. Clair, "A CAA Study of Turbulence Distortion in Broadband Fan Interaction Noise," en, in *22nd AIAA/CEAS Aeroacoustics Conference*, Lyon, France: American Institute of Aeronautics and Astronautics, May 2016, ISBN: 978-1-62410-386-5. DOI: 10.2514/6.2016-2839. [Online]. Available: https://arc.aiaa.org/doi/10.2514/6.2016-2839.

[23] L. Bowen, A. Celik, and M. Azarpeyvand, "A thorough experimental investigation on airfoil turbulence interaction noise," en, *Physics of Fluids*, vol. 35, no. 3, p. 035 123, Mar. 2023, ISSN: 1070-6631, 1089-7666. DOI: 10.1063/5.0142704. [Online]. Available: https://pubs.aip.org/pof/article/35/3/035123/2882088/A-thorough-experimental-investigation-on-airfoil.

[24] F. L. Dos Santos, L. Botero, C. Venner, and L. D. De Santana, "On the turbulence distortion effects for airfoil leading-edge noise prediction," en, in *28th AIAA/CEAS Aeroacoustics 2022 Conference*, Southampton, UK: American Institute of Aeronautics and Astronautics, Jun. 2022, ISBN: 978-1-62410-664-4. DOI: 10.2514/6.2022-3045. [Online]. Available: https://arc.aiaa.org/doi/10.2514/6.2022-3045.

[25] L. Botero-Bolívar, F. L. Dos Santos, C. H. Venner, and L. D. De Santana, “Experimental and predicted leading- and trailing-edge noise of symmetric airfoils under zero mean-loading,” en, *Applied Acoustics*, vol. 212, p. 109 579, Sep. 2023, ISSN: 0003682X. DOI: 10.1016/j.apacoust.2023.109579. [Online]. Available: https://linkinghub.elsevier.com/retrieve/pii/S0003682X23003778.

[26] F. L. Dos Santos, L. Botero-Bolívar, C. H. Venner, and L. D. De Santana, “Inflow turbulence distortion for airfoil leading-edge noise prediction for large turbulence length scales for zero-mean loading,” en, *The Journal of the Acoustical Society of America*, vol. 153, no. 3, pp. 1811–1822, Mar. 2023, ISSN: 0001-4966, 1520-8524. DOI: 10.1121/10.0017458. [Online]. Available: https://pubs.aip.org/jasa/article/153/3/1811/2881349/Inflow-turbulence-distortion-for-airfoil-leading.

[27] A. K. Lidtke, M. Klapwijk, and T. Lloyd, “Scale-Resolving Simulations of a Circular Cylinder Subjected to Low Mach Number Turbulent Inflow,” en, *Journal of Marine Science and Engineering*, vol. 9, no. 11, p. 1274, Nov. 2021, ISSN: 2077-1312. DOI: 10.3390/jmse9111274. [Online]. Available: https://www.mdpi.com/2077-1312/9/11/1274.

[28] A. Piccolo, R. Zamponi, F. Avallone, and D. Ragni, “Turbulence-distortion analysis for leading-edge noise-prediction enhancement,” en, in *AIAA AVIATION 2023 Forum*, San Diego, CA and Online: American Institute of Aeronautics and Astronautics, Jun. 2023, ISBN: 978-1-62410-704-7. DOI: 10.2514/6.2023-3628. [Online]. Available: https://arc.aiaa.org/doi/10.2514/6.2023-3628.

[29] A. F. P. Ribeiro, F. L. Dos Santos, K. Venner, and L. D. De Santana, “Numerical study of inflow turbulence distortion and noise for airfoils,” en, *Physics of Fluids*, vol. 35, no. 11, p. 115 112, Nov. 2023, ISSN: 1070-6631, 1089-7666. DOI: 10.1063/5.0169000. [Online]. Available: https://pubs.aip.org/pof/article/35/11/115112/2919903/Numerical-study-of-inflow-turbulence-distortion.

[30] M. Roger, “Sound Radiation by Moving Surfaces and the Green’s Functions Technique,” in *Noise Sources in Turbulent Shear Flows: Fundamentals and Applications*, R. Camussi, Ed., vol. 545, Series Title: CISM International Centre for Mechanical Sciences, Vienna: Springer Vienna, 2013, pp. 73–116, ISBN: 978-3-7091-1457-5 978-3-7091-1458-2. DOI: 10.1007/978-3-7091-1458-2_2. [Online]. Available: http://link.springer.com/10.1007/978-3-7091-1458-2_2.

[31] T. F. Brooks, S. D. Pope, and M. A. Marcolini, *Airfoil Self-Noise and Prediction*, en, 1989. [Online]. Available: https://ntrs.nasa.gov/citations/19890016302.

[32] H. H. Hubbard and K. P. Shepherd, “Aeroacoustics of large wind turbines,” en, *The Journal of the Acoustical Society of America*, vol. 89, no. 6, pp. 2495–2508, Jun. 1991, ISSN: 0001-4966, 1520-8524. DOI: 10.1121/1.401021. [Online]. Available: https://pubs.aip.org/jasa/article/89/6/2495/629938/Aeroacoustics-of-large-wind-turbines.

[33] F. Ricciardelli and S. Polimeno, “Some characteristics of the wind flow in the lower Urban Boundary Layer,” en, *Journal of Wind Engineering and Industrial Aerodynamics*, vol. 94, no. 11, pp. 815–832, Nov. 2006, ISSN: 01676105. DOI: 10.1016/j.jweia.2006.06.003. [Online]. Available: https://linkinghub.elsevier.com/retrieve/pii/S0167610506000894.

[34] S. B. Pope, *Turbulent flows*, eng, 1. publ., 12. print. Cambridge: Cambridge Univ. Press, 2015, ISBN: 978-0-521-59886-6 978-0-521-59125-6.

[35] F. T. Nieuwstadt, J. Westerweel, and B. J. Boersma, *Turbulence: Introduction to Theory and Applications of Turbulent Flows*, en. Cham: Springer International Publishing, 2016, ISBN: 978-3-319-31597-3 978-3-319-31599-7. DOI: 10.1007/978-3-319-31599-7. [Online]. Available: http://link.springer.com/10.1007/978-3-319-31599-7.

[36] J. O. Hinze, *Turbulence* (McGraw-Hill series in mechanical engineering), 2d ed. New York: McGraw-Hill, 1975, ISBN: 978-0-07-029037-2.

[37] G. I. Taylor, “The Spectrum of Turbulence,” en, *Proceedings of the Royal Society of London. Series A - Mathematical and Physical Sciences*, vol. 164, no. 919, pp. 476–490, Feb. 1938, ISSN: 0080-4630, 2053-9169. DOI: 10.1098/rspa.1938.0032. [Online]. Available: https://royalsocietypublishing.org/doi/10.1098/rspa.1938.0032.

[38] C. C. Lin, “On Taylor’s hypothesis and the acceleration terms in the Navier-Stokes equation,” en, *Quarterly of Applied Mathematics*, vol. 10, no. 4, pp. 295–306, 1953, ISSN: 0033-569X, 1552-4485. DOI: 10.1090/qam/51649. [Online]. Available: https://www.ams.org/qam/1953-10-04/S0033-569X-1953-51649-7/.

[39] A. Trush, S. Pospíšil, and H. Kozmar, “Comparison of turbulence integral length scale determination methods,” Nov. 2020, pp. 113–123. DOI: 10.2495/AFM200111. [Online]. Available: http://library.witpress.com/viewpaper.asp?pcode=AFM20-011-1.

[40] T. N. Nandi and D. Yeo, “Estimation of integral length scales across the neutral atmospheric boundary layer depth: A Large Eddy Simulation study,” en, *Journal of Wind Engineering and Industrial Aerodynamics*, vol. 218, p. 104 715, Nov. 2021, ISSN: 01676105. DOI: 10.1016/j.jweia.2021.104715. [Online]. Available: https://linkinghub.elsevier.com/retrieve/pii/S0167610521001951.

[41] B. E. Rapp, “Computational Fluid Dynamics,” en, in *Microfluidics: Modelling, Mechanics and Mathematics*, Elsevier, 2017, pp. 609–622, ISBN: 978-1-4557-3141-1. DOI: 10.1016/B978-1-4557-3141-1.50029-0. [Online]. Available: https://linkinghub.elsevier.com/retrieve/pii/B9781455731411500290.

[42] J. H. Ferziger, M. Perić, and R. L. Street, *Computational Methods for Fluid Dynamics*, en. Cham: Springer International Publishing, 2020, ISBN: 978-3-319-99691-2 978-3-319-99693-6. DOI: 10.1007/978-3-319-99693-6. [Online]. Available: http://link.springer.com/10.1007/978-3-319-99693-6.

[43] E. Terry, *CFD: The truth and the tales*, en, Aug. 2018. [Online]. Available: https://actiflow.com/cfd-the-truth-and-the-tales-2/.

[44] S. Rodriguez, *Applied Computational Fluid Dynamics and Turbulence Modeling: Practical Tools, Tips and Techniques*, en. Cham: Springer International Publishing, 2019, ISBN: 978-3-030-28690-3 978-3-030-28691-0. DOI: 10.1007/978-3-030-28691-0. [Online]. Available: http://link.springer.com/10.1007/978-3-030-28691-0.

[45] B. Pena and L. Huang, “A review on the turbulence modelling strategy for ship hydrodynamic simulations,” en, *Ocean Engineering*, vol. 241, p. 110 082, Dec. 2021, ISSN: 00298018. DOI: 10.1016/j.oceaneng.2021.110082. [Online]. Available: https://linkinghub.elsevier.com/retrieve/pii/S0029801821014104.

[46] G. Sun and J. A. Domaradzki, “Implicit LES using adaptive filtering,” en, *Journal of Computational Physics*, vol. 359, pp. 380–408, Apr. 2018, ISSN: 00219991. DOI: 10.1016/j.jcp.2018.01.009. [Online]. Available: https://linkinghub.elsevier.com/retrieve/pii/S0021999118300196.

[47] J. M. Foale, “Simulating Extinction and Blow-off in Kerosene Swirl Spray Flames,” en, Thesis (Doctoral), University of Cambridge, Oct. 2021. DOI: 10.17863/CAM.82714. [Online]. Available: https://www.repository.cam.ac.uk/handle/1810/335283.

[48] J. Tu, G.-H. Yeoh, and C. Liu, “Practical Guidelines for CFD Simulation and Analysis,” en, in *Computational Fluid Dynamics*, Elsevier, 2018, pp. 255–290, ISBN: 978-0-08-101127-0. DOI: 10.1016/B978-0-08-101127-0.00007-6. [Online]. Available: https://linkinghub.elsevier.com/retrieve/pii/B9780081011270000076.

[49] A. K. Lidtke, T. Lloyd, F. H. Lafeber, and J. Bosschers, “Predicting cavitating propeller noise in off-design conditions using scale-resolving CFD simulations,” en, *Ocean Engineering*, vol. 254, p. 111 176, Jun. 2022, ISSN: 00298018. DOI: 10.1016/j.oceaneng.2022.111176. [Online]. Available: https://linkinghub.elsevier.com/retrieve/pii/S0029801822005820.

[50] M. Liefvendahl and C. Fureby, “Grid requirements for LES of ship hydrodynamics in model and full scale,” en, *Ocean Engineering*, vol. 143, pp. 259–268, Oct. 2017, ISSN: 00298018. DOI: 10.1016/j.oceaneng.2017.07.055. [Online]. Available: https://linkinghub.elsevier.com/retrieve/pii/S0029801817304419.

[51] M. Liefvendahl and M. Johansson, “Wall-Modeled LES for Ship Hydrodynamics in Model Scale,” en, *Journal of Ship Research*, vol. 65, no. 01, pp. 41–54, Mar. 2021, ISSN: 0022-4502, 1542-0604. DOI: 10.5957/JOSR.09180065. [Online]. Available: https://onepetro.org/JSR/article/65/01/41/450660/Wall-Modeled-LES-for-Ship-Hydrodynamics-in-Model.

[52] S.-H. Peng, P. Doerffer, W. Haase, *et al.*, Eds., *Progress in Hybrid RANS-LES Modelling* (Notes on Numerical Fluid Mechanics and Multidisciplinary Design). Berlin, Heidelberg: Springer Berlin Heidelberg, 2010, vol. 111, ISBN: 978-3-642-14167-6 978-3-642-14168-3. DOI: 10.1007/978-3-642-14168-3. [Online]. Available: http://link.springer.com/10.1007/978-3-642-14168-3.

[53] P. R. Spalart, S. Deck, M. L. Shur, K. D. Squires, M. K. Strelets, and A. Travin, "A New Version of Detached-eddy Simulation, Resistant to Ambiguous Grid Densities," en, *Theoretical and Computational Fluid Dynamics*, vol. 20, no. 3, pp. 181–195, Jul. 2006, ISSN: 0935-4964, 1432-2250. DOI: 10.1007/s00162-006-0015-0. [Online]. Available: http://link.springer.com/10.1007/s00162-006-0015-0.

[54] P. Roach, "The generation of nearly isotropic turbulence by means of grids," en, *International Journal of Heat and Fluid Flow*, vol. 8, no. 2, pp. 82–92, Jun. 1987, ISSN: 0142727X. DOI: 10.1016/0142-727X(87)90001-4. [Online]. Available: https://linkinghub.elsevier.com/retrieve/pii/0142727X87900014.

[55] R. E. Seoud and J. C. Vassilicos, "Dissipation and decay of fractal-generated turbulence," en, *Physics of Fluids*, vol. 19, no. 10, p. 105 108, Oct. 2007, ISSN: 1070-6631, 1089-7666. DOI: 10.1063/1.2795211. [Online]. Available: https://pubs.aip.org/pof/article/19/10/105108/938603/Dissipation-and-decay-of-fractal-generated.

[56] T. Kurian and J. H. M. Fransson, "Grid-generated turbulence revisited," *Fluid Dynamics Research*, vol. 41, no. 2, p. 021 403, Apr. 2009, ISSN: 0169-5983, 1873-7005. DOI: 10.1088/0169-5983/41/2/021403. [Online]. Available: https://iopscience.iop.org/article/10.1088/0169-5983/41/2/021403.

[57] P.-Å. Krogstad and P. Davidson, "Homogeneous Turbulence Generated by Multi-scale Grids," *Journal of Physics: Conference Series*, vol. 318, no. 3, p. 032 042, Dec. 2011, ISSN: 1742-6596. DOI: 10.1088/1742-6596/318/3/032042. [Online]. Available: https://iopscience.iop.org/article/10.1088/1742-6596/318/3/032042.

[58] L. Bowen, A. Celik, M. Azarpeyvand, and C. R. I. Da Silva, "Grid Generated Turbulence for Aeroacoustic Facility," en, *AIAA Journal*, vol. 60, no. 3, pp. 1833–1847, Mar. 2022, ISSN: 0001-1452, 1533-385X. DOI: 10.2514/1.J060851. [Online]. Available: https://arc.aiaa.org/doi/10.2514/1.J060851.

[59] T. Geyer, E. Sarradj, J. Giesler, and M. Hobracht, "Experimental assessment of the noise generated at the leading edge of porous airfoils using microphone array techniques," en, in *17th AIAA/CEAS Aeroacoustics Conference (32nd AIAA Aeroacoustics Conference)*, Portland, Oregon: American Institute of Aeronautics and Astronautics, Jun. 2011, ISBN: 978-1-60086-943-3. DOI: 10.2514/6.2011-2713. [Online]. Available: https://arc.aiaa.org/doi/10.2514/6.2011-2713.

[60] F. L. Dos Santos, L. Botero-Bolívar, C. H. Venner, and L. D. De Santana, "Wall-pressure spectra, spanwise correlation, and far-field noise measurements of a NACA 0008 airfoil under uniform and turbulent inflows," en, *Applied Acoustics*, vol. 211, p. 109 546, Aug. 2023, ISSN: 0003682X. DOI: 10.1016/j.apacoust.2023.109546. [Online]. Available: https://linkinghub.elsevier.com/retrieve/pii/S0003682X23003444.

[61] C.-L. Shih, W.-C. Chen, K.-C. Chang, and M.-R. Wang, "Velocity measurements of turbulent wake flow over a circular cylinder," en, *International Journal of Modern Physics: Conference Series*, vol. 42, p. 1 660 182, Jan. 2016, ISSN: 2010-1945, 2010-1945. DOI: 10.1142/S2010194516601824. [Online]. Available: https://www.worldscientific.com/doi/abs/10.1142/S2010194516601824.

[62] P. Liu, D. Wang, and F. Yan, "Experimental study on the wake characteristics of the circular cylinder with the V-groove surface," en, *International Journal of Naval Architecture and Ocean Engineering*, vol. 14, p. 100 449, 2022, ISSN: 20926782. DOI: 10.1016/j.ijnaoe.2022.100449. [Online]. Available: https://linkinghub.elsevier.com/retrieve/pii/S2092678222000152.

[63] G. Tabor and M. Baba-Ahmadi, "Inlet conditions for large eddy simulation: A review," en, *Computers & Fluids*, vol. 39, no. 4, pp. 553–567, Apr. 2010, ISSN: 00457930. DOI: 10.1016/j.compfluid.2009.10.007. [Online]. Available: https://linkinghub.elsevier.com/retrieve/pii/S0045793009001601.

[64] N. Jarrin, S. Benhamadouche, D. Laurence, and R. Prosser, "A synthetic-eddy-method for generating inflow conditions for large-eddy simulations," en, *International Journal of Heat and Fluid Flow*, vol. 27, no. 4, pp. 585–593, Aug. 2006, ISSN: 0142727X. DOI: 10.1016/j.ijheatfluidflow.2006.02.006. [Online]. Available: https://linkinghub.elsevier.com/retrieve/pii/S0142727X06000282.

[65] A. K. Lidtke and M. Klapwijk, *Synthetic inflow turbulence generator in ReFRESCO*, en, Jun. 2020. (visited on 09/01/2023).

[66] T. Blackmore, W. M. Batten, and A. S. Bahaj, "Inlet grid-generated turbulence for large-eddy simulations," en, *International Journal of Computational Fluid Dynamics*, vol. 27, no. 6-7, pp. 307–315, Jul. 2013, ISSN: 1061-8562, 1029-0257. DOI: 10.1080/10618562.2013.819972. [Online]. Available: http://www.tandfonline.com/doi/abs/10.1080/10618562.2013.819972.

[67] X. Wu, "Inflow Turbulence Generation Methods," en, *Annual Review of Fluid Mechanics*, vol. 49, no. 1, pp. 23–49, Jan. 2017, ISSN: 0066-4189, 1545-4479. DOI: 10.1146/annurev-fluid-010816-060322. [Online]. Available: https://www.annualreviews.org/doi/10.1146/annurev-fluid-010816-060322.

[68] T. Lloyd, "Large eddy simulations of inflow turbulence noise: Application to tidal turbines," en, Thesis (Doctoral), University of Southampton, Fluid Structure Interactions Group, Dec. 2013. [Online]. Available: http://eprints.soton.ac.uk/id/eprint/361691.

[69] T. Colonius and S. K. Lele, "Computational aeroacoustics: Progress on nonlinear problems of sound generation," en, *Progress in Aerospace Sciences*, vol. 40, no. 6, pp. 345–416, Aug. 2004, ISSN: 03760421. DOI: 10.1016/j.paerosci.2004.09.001. [Online]. Available: https://linkinghub.elsevier.com/retrieve/pii/S0376042104000570.

[70] S. Glegg and W. Devenport, "The Ffowcs Williams and Hawkings equation," en, in *Aeroacoustics of Low Mach Number Flows*, Elsevier, 2017, pp. 95–114, ISBN: 978-0-12-809651-2. DOI: 10.1016/B978-0-12-809651-2.00005-9. [Online]. Available: https://linkinghub.elsevier.com/retrieve/pii/B9780128096512000059.

[71] L. D. De Santana, "Semi-analytical methodologies for airfoil noise prediction," en, Thesis (Doctoral), Katholieke Universiteit Leuven, Leuven, Sep. 2015. [Online]. Available: https://lirias.kuleuven.be/retrieve/332128.

[72] L. D. Santana, J. Christophe, C. Schram, and W. Desmet, "A Rapid Distortion Theory modified turbulence spectra for semi-analytical airfoil noise prediction," en, *Journal of Sound and Vibration*, vol. 383, pp. 349–363, Nov. 2016, ISSN: 0022460X. DOI: 10.1016/j.jsv.2016.07.026. [Online]. Available: https://linkinghub.elsevier.com/retrieve/pii/S0022460X1630356X.

[73] J. Ffowcs Williams and D. Hawkings, "Sound Generation by Turbulence and Surfaces in Arbitrary Motion," en, *Philosophical Transactions of the Royal Society of London. Series A, Mathematical and Physical Sciences*, vol. 264, no. 1151, pp. 321–342, May 1969. [Online]. Available: https://www.jstor.org/stable/73790?seq=22.

[74] A. F. Ribeiro, M. R. Khorrami, R. Ferris, B. König, and P. A. Ravetta, "Lessons learned on the use of data surfaces for Ffowcs Williams-Hawkings calculations: Airframe noise applications," en, *Aerospace Science and Technology*, vol. 135, p. 108 202, Apr. 2023, ISSN: 12709638. DOI: 10.1016/j.ast.2023.108202. [Online]. Available: https://linkinghub.elsevier.com/retrieve/pii/S1270963823000998.

[75] Y. Jin, F. Liao, J. Cai, and P. J. Morris, "Investigation on rod-airfoil noise with high-order cell-centered finite difference method and acoustic analogy," en, *Aerospace Science and Technology*, vol. 102, p. 105 851, Jul. 2020, ISSN: 12709638. DOI: 10.1016/j.ast.2020.105851. [Online]. Available: https://linkinghub.elsevier.com/retrieve/pii/S1270963820305332.

[76] W. Chen, H. Lei, Y. Xing, L. Wang, T. Zhou, and W. Qiao, "On the airfoil leading-edge noise reduction using poro-wavy leading edges," en, *Physics of Fluids*, vol. 36, no. 3, p. 035 158, Mar. 2024, ISSN: 1070-6631, 1089-7666. DOI: 10.1063/5.0198034. [Online]. Available: https://pubs.aip.org/pof/article/36/3/035158/3277874/On-the-airfoil-leading-edge-noise-reduction-using.

[77] MARIN, *ReFRESCO.pdf*, en. [Online]. Available: https://www.marin.nl/en/about/facilities-and-tools/software/refresco (visited on 03/28/2024).

[78] L. Eça, C. Klaij, G. Vaz, M. Hoekstra, and F. Pereira, "On code verification of RANS solvers," en, *Journal of Computational Physics*, vol. 310, pp. 418–439, Apr. 2016, ISSN: 00219991. DOI: 10.1016/j.jcp.2016.01.002. [Online]. Available: https://linkinghub.elsevier.com/retrieve/pii/S0021999116000036.

[79] M. Ye, H.-C. Chen, and A. Koop, "Verification and validation of CFD simulations of the NTNU BT1 wind turbine," en, *Journal of Wind Engineering and Industrial Aerodynamics*, vol. 234, p. 105 336, Mar. 2023, ISSN: 01676105. DOI: 10.1016/j.jweia.2023.105336. [Online]. Available: https://linkinghub.elsevier.com/retrieve/pii/S0167610523000399.

[80] F. R. Menter, M. Kuntz, and R. Langtry, "Ten Years of Industrial Experience with the SST Turbulence Model," en, *Heat and Mass Transfer 4*, pp. 625–632, 2003. [Online]. Available: https://cfd.spbstu.ru/agarbaruk/doc/2003_Menter,%20Kuntz,%20Langtry_Ten%20years%20of%20industrial%20experience%20with%20the%20SST%20turbulence%20model.pdf.

[81] M. S. Gritskevich, A. V. Garbaruk, J. Schütze, and F. R. Menter, "Development of DDES and IDDES Formulations for the k-ω Shear Stress Transport Model," en, *Flow, Turbulence and Combustion*, vol. 88, no. 3, pp. 431–449, Apr. 2012, ISSN: 1386-6184, 1573-1987. DOI: 10.1007/s10494-011-9378-4. [Online]. Available: http://link.springer.com/10.1007/s10494-011-9378-4.

[82] Y. Kim, I. P. Castro, and Z.-T. Xie, "Divergence-free turbulence inflow conditions for large-eddy simulations with incompressible flow solvers," en, *Computers & Fluids*, vol. 84, pp. 56–68, Sep. 2013, ISSN: 00457930. DOI: 10.1016/j.compfluid.2013.06.001. [Online]. Available: https://linkinghub.elsevier.com/retrieve/pii/S0045793013002132.

[83] N. Jarrin, R. Prosser, J.-C. Uribe, S. Benhamadouche, and D. Laurence, "Reconstruction of turbulent fluctuations for hybrid RANS/LES simulations using a Synthetic-Eddy Method," en, *International Journal of Heat and Fluid Flow*, vol. 30, no. 3, pp. 435–442, Jun. 2009, ISSN: 0142727X. DOI: 10.1016/j.ijheatfluidflow.2009.02.016. [Online]. Available: https://linkinghub.elsevier.com/retrieve/pii/S0142727X09000538.

[84] M. Klapwijk, T. Lloyd, G. Vaz, and T. Van Terwisga, "Evaluation of scale-resolving simulations for a turbulent channel flow," en, *Computers & Fluids*, vol. 209, p. 104 636, Sep. 2020, ISSN: 00457930. DOI: 10.1016/j.compfluid.2020.104636. [Online]. Available: https://linkinghub.elsevier.com/retrieve/pii/S0045793020302085.

[85] F. L. Dos Santos, L. Botero-Bolívar, C. Venner, and L. D. De Santana, "Modeling the Turbulence Spectrum Dissipation Range for Leading-Edge Noise Prediction," en, *AIAA Journal*, vol. 60, no. 6, pp. 3581–3592, Jun. 2022, ISSN: 0001-1452, 1533-385X. DOI: 10.2514/1.J061106. [Online]. Available: https://arc.aiaa.org/doi/10.2514/1.J061106.

[86] J. Brouwer, J. Tukker, Y. Klinkenberg, and M. Van Rijsbergen, "Random uncertainty of statistical moments in testing: Mean," en, *Ocean Engineering*, vol. 182, pp. 563–576, Jun. 2019, ISSN: 00298018. DOI: 10.1016/j.oceaneng.2019.04.068. [Online]. Available: https://linkinghub.elsevier.com/retrieve/pii/S0029801819301970.

[87] J. Brouwer, J. Tukker, and M. Rijsbergen, "Uncertainty Analysis of Finete Length Measurement Signals," en, Gdansk, Sep. 2013. [Online]. Available: https://www.researchgate.net/publication/295702719.

[88] P. Welch, "The use of fast Fourier transform for the estimation of power spectra: A method based on time averaging over short, modified periodograms," en, *IEEE Transactions on Audio and Electroacoustics*, vol. 15, no. 2, pp. 70–73, Jun. 1967, ISSN: 0018-9278. DOI: 10.1109/TAU.1967.1161901. [Online]. Available: http://ieeexplore.ieee.org/document/1161901/.

[89] J.-C. Giret, A. Sengissen, S. Moreau, M. Sanjosé, and J.-c. Jouhaud, "Prediction of the sound generated by a rod-airfoil configuration using a compressible unstructured LES solver and a FW-H analogy," en, in *18th AIAA/CEAS Aeroacoustics Conference (33rd AIAA Aeroacoustics Conference)*, Colorado Springs, CO: American Institute of Aeronautics and Astronautics, Jun. 2012, ISBN: 978-1-60086-932-7. DOI: 10.2514/6.2012-2058. [Online]. Available: https://arc.aiaa.org/doi/10.2514/6.2012-2058.

[90] C. Kato, A. Iida, Y. Takano, H. Fujita, and M. Ikegawa, “Numerical prediction of aerodynamic noise radiated from low Mach number turbulent wake,” en, in *31st Aerospace Sciences Meeting*, Reno,NV,U.S.A.: American Institute of Aeronautics and Astronautics, Jan. 1993. DOI: 10.2514/6.1993-145. [Online]. Available: https://arc.aiaa.org/doi/10.2514/6.1993-145.

[91] S. Glegg and W. Devenport, “Measurement, signal processing, and uncertainty,” en, in *Aeroacoustics of Low Mach Number Flows*, Elsevier, 2017, pp. 271–298, ISBN: 978-0-12-809651-2. DOI: 10.1016/B978-0-12-809651-2.00011-4. [Online]. Available: https://linkinghub.elsevier.com/retrieve/pii/B9780128096512000114.

[92] F. S. Pereira, L. Eça, G. Vaz, and S. S. Girimaji, “Toward Predictive RANS and SRS Computations of Turbulent External Flows of Practical Interest,” en, *Archives of Computational Methods in Engineering*, vol. 28, no. 5, pp. 3953–4029, Aug. 2021, ISSN: 1134-3060, 1886-1784. DOI: 10.1007/s11831-021-09563-0. [Online]. Available: https://link.springer.com/10.1007/s11831-021-09563-0.

[93] R. McElreath, *Statistical rethinking: a Bayesian course with examples in R and Stan* (Chapman & Hall/CRC texts in statistical science series), eng, Second edition. Boca Raton London New York: CRC Press, 2020, ISBN: 978-0-367-13991-9.

A

Paper for the Numerical Towing Tank Symposium 2024

Besides this master thesis report, a closed exam (defence) and a public presentation, a part of the work is also documented in a paper (extended abstract) titled ”*Quantifying the effect of turbulence intensity on turbulence-interaction noise of an airfoil using scale-resolving simulations*. This paper will be submitted to the 26th Numerical Towing Tank Symposium (NuTTS’24), which will take place in October 2024 in Duisburg, Germany. For more information on the conference, the reader is referred to their website. The current draft of the paper can be found on the following six pages. The draft is based on information found within this work, but may be altered after handing in the final version of this report. The paper, as well as this report, have been written by G.J. Dekkers. All other authors (mentioned in the paper) will only partake in the paper once the MSc Thesis has been handed in and graded.

26th Numerical Towing Tank Symposium (NuTTS)
23-25 October 2024 - Duisburg, Germany

Quantifying the effect of turbulence intensity on turbulence-interaction noise of an airfoil using scale-resolving simulations

Gert J. Dekkers*†, Artur K. Lidtke†, Thomas P. Lloyd†, Fernanda L. dos Santos†, and Gabriel D. Weymouth*

*TU Delft, Delft/The Netherlands, † MARIN, Wageningen/The Netherlands
gertdekkers07@gmail.com

1 Introduction

Noise pollution from ships, wind turbines and aircraft has been known to negatively impact people and wildlife. Even though noise control onboard ships has been strictly regulated, awareness has also been raised for underwater radiated noise. It is the low-frequency broadband noise component, which can travel over large distances, that is mostly relevant for marine wildlife, impacting their natural mating and hunting behaviours. In the absence of cavitation such as for tidal turbines, naval vessels and submarines, the low-frequency noise component is dominated by the interaction of the body with a turbulent inflow. The inflow turbulence generates pressure fluctuations on and near the surface of the foil, thereby radiating sound to the far-field. This turbulence-interaction phenomenon is not fully understood.

The framework by Amiet (1975) can be used to predict far-field turbulence-interaction noise for an airfoil, which predicts that the far-field sound pressure level (SPL) is a function of the square of the turbulence intensity (TI), i.e. $SPL = f(TI^2)$. Amiet's framework, however, does not account for the geometrical properties of the foil. This work presents the results of a numerical study to determine the effect of the turbulence intensity on the far-field turbulence-interaction noise for a NACA0008 airfoil. A comparison of the numerically predicted far-field noise to Amiet's work is performed to evaluate the accuracy of Amiet for different receiver angles. The Ffowcs Williams and Hawkings (1969) (FW-H) acoustic analogy, which separates the generation and propagation of the sound, is adopted in this work to predict the SPL. Validation of the inflow turbulence and generated sound are performed by comparing one of the numerical cases to an experimental and numerical investigation for the same airfoil.

2 Methodology

2.1 Numerical method and turbulence generation

Numerical simulations are performed using the finite volume code ReFRESCO developed by MARIN in collaboration with universities and other partners. It solves the unsteady, incompressible Navier-Stokes and mass continuity equations using a finite-volume and time-implicit framework. ReFRESCO allows the use of both structured and unstructured meshes as well as turbulence and cavitation models. Pressure-velocity coupling based on the SIMPLE scheme is used, where at every timestep the non-linear system is linearised using Picard's method. The FW-H framework has been implemented as a run-time postprocessing tool with a solid data surface aligning with the surface of the foil.

A scale-resolving simulation (SRS) framework is adapted, readily thoroughly validated in the work by Lidtke et al. (2022). The change between resolving and modelling of the turbulence is made by the improved delayed detached eddy simulations (IDDES) framework based on Gritskevich et al. (2012). It employs the $k-\omega$ shear stress transport model, switching between LES and RANS based on the turbulent length scale. A SRS approach is preferred due to its accuracy in the bulk of the flow (LES) and low computational time near the foil (RANS), which is sufficient for the current work.

All simulations are run with a fixed time step of $\Delta t = 3.55 \times 10^{-5}$ s, or based on the chord and set inflow speed $\Delta t^* = \Delta t \cdot U_{inf}/c = 3 \times 10^{-3}$. Simulations with a bigger timestep showed unsatisfactory results regarding the turbulence resolution and the Courant number, which remains lower than 15 for the current timestep with high values only sporadically found near the foil.

Turbulence is generated at the inflow turbulence generator (ITG) using a synthetic generation method based on the work of Kim et al. (2013) and implemented in ReFRESCO by Klapwijk et al. (2020). At each outer loop (timestep), body forces are applied at points (i) on a plane with its normal in the direction of the flow. At each point, desired Reynolds stresses are converted to velocity fluctuations (u_i'), which in turn determine the body forces ($F_{b,i}$) according to

$$F_{b,i} = \frac{\rho \overline{u_i}(\overline{u_i} + u_i' - u_i)}{L_{ITG}} \cdot b. \tag{1}$$

Here, L_{ITG} is the thickness over which the body forces are spread in the flow direction, and b is the amplification factor used to assure faster convergence to the desired values. One can recognize the Reynolds decomposition in the numerator of Eq. (1). In this case if the instantaneous velocity fluctuation (u_i') is readily achieved at that point ($\overline{u_i} - u_i = -u_i'$) the body force term iterates towards zero, thereby improving the convergence behaviour of the solver. This ensures low overhead within ReFRESCO.

2.2 Case description

Fig. 1 shows a side view of the numerical setup used. The coordinate system with x in the flow, y in the vertical and z in the spanwise directions has its origin at the leading edge of the foil. The boundary conditions of the sides are periodic to prevent interactions between them as much as possible, making the total span $d = 0.67c$. Dampening boxes (DB) are placed upstream of the ITG and downstream of the foil to prevent reflections from the inlet and outlet, respectively. Inflow turbulence is generated not over the full height of the domain to prevent strong interactions with the top and bottom boundary conditions and to save computational time. The acoustic receivers, for the FW-H computation, are placed at 1.5 m in a circle around the airfoil at every two degrees with the array's centre at midspan and half of the chord, i.e. $(x, y, z) = (0.5c, 0, 0)$. The angle defining the placement of the probes is θ with $\theta = 0$ degrees in the direction of the trailing edge. Table 1 presents a comprehensive overview of the inputs for the four numerical cases investigated in this paper. These cases only differ in turbulence intensity; all other inputs remain constant. A mesh resolution study has shown mesh convergence for the inflow turbulence, wall pressure on the foil and far-field acoustics. Similar results are also found for a study in which the spanwise domain size has been varied. For brevity, those results are not included in this paper. More details, also about the setup, can be found in the work by Dekkers (2024).

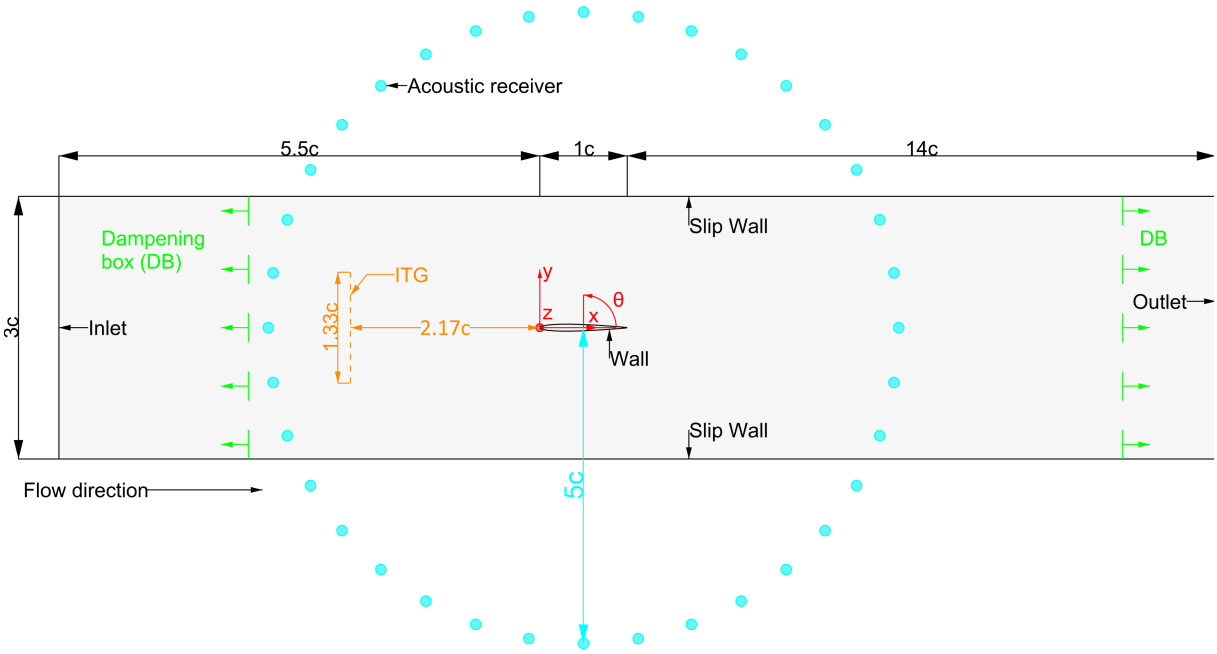

Fig. 1: Side view of the numerical setup. All distances are visualised based on the chord of the NACA0008 airfoil (c = 300 mm). The slice is taken at midspan of the foil.

Table 1: Parameters of the four numerical turbulence intensity cases. Case C2 is used for validation.

Parameter	**Symbol**	**Case 1**	**Case 2**	**Case 3**	**Case 4**
Label figures	N.A.	C1: TI=13.5%	C2: TI=11.4%	C3: TI=7.6%	C4: TI=4.1%
Foil type	N.A.	NACA0008			
Foil chord [m]	c	0.3			
Foil span [m]	d	0.2			
Foil leading edge radius [mm]	r_{LE}	2.1			
Turbulence intensity [%] At $x/c = 0$ in empty domain	$TI = u_{rms}/\overline{u}$	13.5	11.4	7.6	4.1
Inflow velocity [m/s]	U_{inf}	25.26 ($Re_c \approx 5.1 \times 10^5$)			

3 Validation

Two separate sets of validation are performed. Validation of the inflow turbulence is performed to show that the current setup can generate realistic homogeneous isotropic turbulence downstream of the ITG. This was done in an empty domain (without the foil) to allow for more accurate tuning of the ITG. Numerical results are compared to experimental results by Dos Santos et al. (2022), who applied grid-generated turbulence. Fig 2a shows the turbulence intensity over the domain with a peak just after the ITG. A clear decay after the ITG is visible, signifying the need for a development length for the turbulence. From $x/c = -0.5$ onwards, there is a good agreement between numerical and experimental results, signifying that the ITG has been accurately tuned so that the turbulence can develop to its intended state.

Fig. 2b shows the mean decidecade band power density[1] of the streamwise velocity. Experimental spectral levels and frequencies have been scaled based on the difference in inflow velocity, local velocity fluctuations and local integral length scale. For $f < 50$ Hz the numerical spectrum is occasionally under-predicted relative to the experimental spectrum. For $50 < f < 1400$ Hz, an over-prediction of a maximum of five decibels is observed. A similar slope of the numerical spectrum relative to the experimental spectrum and the power law with slope -5/3 is found in this frequency range. Both are indicative of isotropic turbulence at this point in the flow. This aligns with the velocity fluctuations being equal for all three directions. An under-prediction of the numerical spectrum relative to the experimental spectrum is observed for $f > 1400$ Hz. This aligns with the estimated mesh cut-off frequency of $f_{mesh} = \frac{0.6 \cdot U_{inf}}{8 \cdot \Delta x} \approx 1100$ Hz, with Δx the average cell size between the ITG and the foil. Generally, good agreement within +/- 5 dB is found between the numerical and experimental spectra for $60 < f < 1400$ Hz.

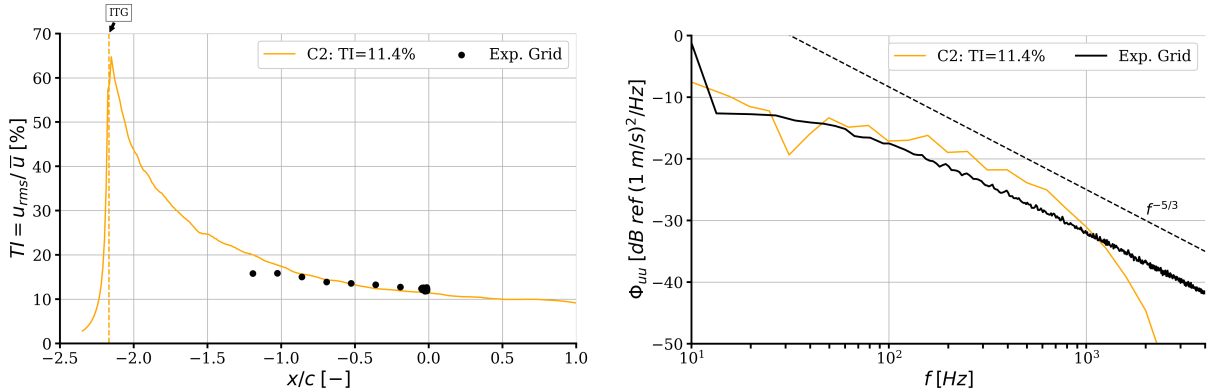

(a) Turbulence intensity at midspan in the direction of flow.

(b) Mean decidecade band power density of the streamwise velocity at the intended leading edge and midspan.

Fig. 2: Numerical and experimental (Dos Santos et al. (2022)) results. Experimental data is scaled for (b) due to a difference in inflow velocity, local velocity fluctuations and local integral length scale.

[1]This is a smoothing of the power spectral density (PSD) as calculated by the Scipy Welch algorithm in Python assuming a 50% overlap between the segment. Smoothing operations are performed using a one-third octave bandwidth top hat filter.

Validation of the acoustics is performed based on experimental data by Dos Santos et al. (2023) and a lattice-Boltzmann method (LBM) simulation by Ribeiro et al. (2023). Grid-generated data, such as that of the turbulence in Fig. 2, is not available for far-field noise since the noise generated by the grid itself was dominant over the foil turbulence-interaction noise. Only experimental data for rod-generated turbulence is, therefore, used. Fig. 3 shows the noise spectra for a receiver at $\theta = 90$ degrees. Data outside the bounds indicated by 2 and 4 is to be disregarded since the wind tunnel background noise dominates the signal outside these bounds. Any data around the rod-shedding frequency, indicated by 1, is also irrelevant since the associated coherent turbulent structures are absent in the numerically-generated isotropic turbulent flow. Experimental validation data is, therefore, only available for $400 < f < 2500$ Hz.

For $600 < f < 2000$ Hz the overlap between the numerical and $U_{inf} = 30$ m/s rod case is very good. However, it is unexpected since the turbulence parameters differ for rod-generated turbulence compared to grid-generated turbulence (for which numerical tuning was performed). The numerical data does, however, show the same trend observed from the experimental data regarding the high-frequency decay of the far-field noise. Independent of the experimental case, the slope of the numerical spectrum is similar to that of the experiments, indicating that the solver can accurately capture the high-frequency decay, disregarding the exact levels. Comparison of numerical data to LBM results shows excellent overlap for $10 < f < 1500$ Hz. This is to be expected since both are for equal inflow velocity and turbulence generated by a grid. The deviations for $f > 1500$ Hz show that the current methodology can better capture the high-frequency decay behaviour when compared to experimental trends. The LBM result shows that the solver can also capture the low-frequency trend, which could not be done from experimental data.

Key takeaway is that the current methodology can accurately capture the high-frequency trend of far-field noise for $600 < f < 2000$ Hz as observed from experimental data. Additionally, the current setup is accurate for $10 < f < 1500$ Hz compared to LBM simulation data. For $f > 2000$ Hz, does the numerical data start to decay faster compared to experimental results, where the latter might already be influenced by the wind tunnel background noise.

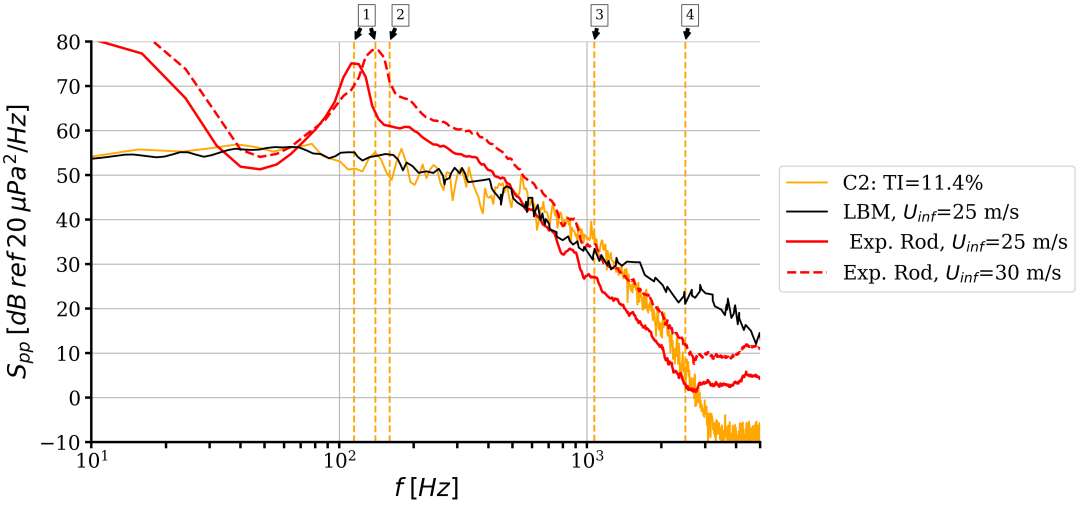

Fig. 3: PSD of the far-field noise for the numerical, LBM (Ribeiro et al. (2023)) and experimental (Dos Santos et al. (2023)) cases. Data is for a receiver at $\theta = 90$ degrees. The numerical case is scaled for the limited span. The dashed vertical lines signify the rod-shedding frequencies (1), lower and upper bounds of experimental acoustic data (2, 4) and estimated mesh cut-off frequency (3).

4 Results and discussion

Four cases, with parameters as shown in Table 1, are evaluated. Fig. 4a shows the turbulence intensity (TI) for the cases up to the leading edge. The higher TI cases are decaying more towards the leading edge, whereas the lower ones are readily homogeneous. Furthermore, the turbulence intensities in the labels do not match the values from Fig. 4a. The values in the labels are taken from the empty domains, which were run on a finer mesh. This is not problematic since the no-foil and foil simulations are validated separately and for different purposes. Any TI values in the remainder of this paper are taken from Fig. 4a.

Fig. 4b shows the far-field noise spectra for the four cases at $\theta = 90$ degrees. For $f < 2000$ Hz, cases C1, C2 and C3 show similar differences and decay behaviour. Case C4 shows far-field energy levels much lower than expected while the difference in intensity is similar between the cases, see Fig. 4a. From results not shown in this paper, it became clear that there is a distinct coupling between the turbulence intensity and the integral length scale. Case C4 has the lowest length scale, likely too small for the mesh to resolve accurately thereby significantly underpredicting the energy levels.

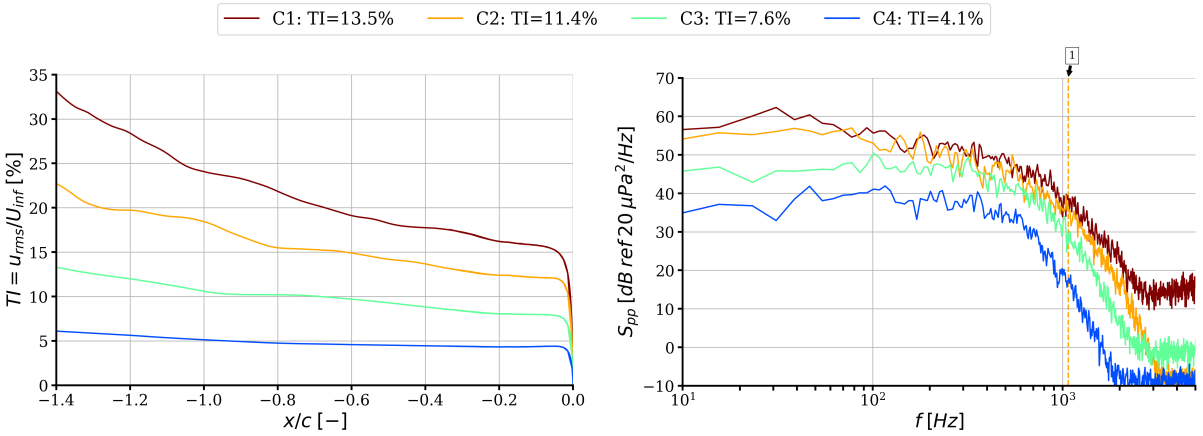

(a) Turbulence intensity at midspan as a function of the distance upstream of the leading edge.

(b) PSD of the far-fied noise at $\theta = 90$ degrees. The dashed line (1) is the estimated mesh cut-off frequency.

Fig. 4: Numerical results for TI and acoustics. Numerical data in (b) is scaled for the limited span.

Integration of a mean decidecade band power density gives the sound pressure level (SPL) in dB. Fig. 5 shows the SPL for the numerical cases at receiver angles $0 \leq \theta \leq 90$ degrees. The starting points for the Amiet scaling ($SPL = f(TI^2)$) are arbitrarily chosen and do not represent the actual outcomes of the Amiet framework. Fits through the data are only performed for cases C1, C2 and C3 since case C4 likely contains errors induced by the mesh/solver. Fitting is performed using the curve-fit procedure from the scipy.optimize library in Python. The baseline curve to fit was chosen as

$$SPL(TI) = a + 10 \cdot log_{10}(TI^b), \tag{2}$$

where a and b are coefficients determined by the fitting procedure. For clarity, data is only presented for the quadrant $0 \leq \theta \leq 90$ degrees. Similar results are, however, found for all three other quadrants.

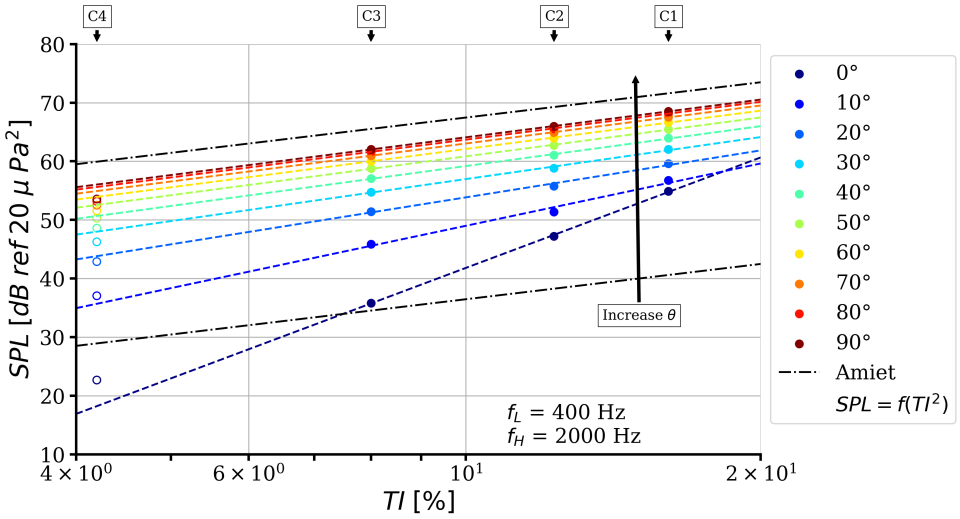

Fig. 5: Sound pressure level (SPL) against turbulence intensity (TI) at different receiver angles for the numerical cases. The Amiet curve depicts the theoretical increase of SPL for a linear increase of turbulence intensity. Dashed lines represent fits through the solid data points; hollow data points are excluded from the fits. f_l and f_h signify the lower and upper bound for the SPL integration, respectively.

A receiver at $\theta = 90$ degrees does see an increase of SPL with the turbulence intensity, but only limited. On the other hand, a receiver at $\theta = 0$ degrees sees a much steeper increase of the SPL for the same increase of TI. Table 2 presents the coefficients of the fits. These coefficients represent the value b in Eq. 2, thereby representing the relation $SPL = f(TI^b)$. Note that the coefficient as predicted by Amiet, independent of the receiver angle, is $b = 2$. It can be concluded that the scaling, as introduced by Amiet, is accurate for receiver angles closer to 90 degrees. The theory becomes less accurate for receiver angles closer to the stagnation line. This aligns with Amiet's assumption that the airfoil is a flat plate of negligible thickness, thereby not considering the interaction of the turbulence with the airfoil. These interaction effects seem to dominate for receiver angles on the stagnation line.

Table 2: Fitting coefficients based on the numerical fits for different receiver angles.

Receiver angle θ [degrees]	0	10	20	30	40	50	60	70	80	90
Slope, fitting parameter b [-]	6.26	3.53	2.66	2.38	2.26	2.20	2.17	2.15	2.14	2.14

5 Conclusion

The turbulence intensity effect on the far-field radiated noise for a NACA0008 airfoil has been addressed in this work. Results from the FW-H acoustic analogy have been compared to the empirical formulation by Amiet. The IDDES turbulence model, in combination with the inflow turbulence generator, has been shown to produce an accurate representation of homogeneous isotropic turbulence upstream of the foil. Reasonable results on far-field acoustics have been found, with agreement relative to experimental and numerical values to within approximately five decibels. Predicted far-field noise levels have been shown to follow the experimentally observed trends and exhibit the expected high-frequency decay behaviour. Results show that the far-field noise scaling with the turbulence intensity proposed by Amiet holds for receiver angles directly above the foil but the theory fails to predict the noise levels accurately for receiver angles more closely aligned with the flow direction for an increase of intensity.

Future work should focus on further tuning/optimizing the current inflow turbulence generator to allow separation of the turbulence intensity from the integral length scale. Also, more effort should be put in the allocation of acoustic data on the surface of the foil by dividing the FW-H surface into strips. This will ensure a better understanding of the turbulence-interaction phenomenon that generates the noise on the leading edge of the foil. Finally, different foil geometries should be evaluated to see whether the found scaling values also hold for other foil shapes.

References

R.K. Amiet (1975). Acoustic radiation from an airfoil in a turbulent stream. *J. of Sound and Vibration*, **41**(4), 407–420.

J. Ffowcs Williams and D. Hawkings (1969). Sound Generation by Turbulence and Surfaces in Arbitrary Motion. *Philosophical Transactions of the Royal Society of London. Series A, Mathematical and Physical Sciences*, **264**(1151), 321–342.

A.K. Lidtke, T. Lloyd, F.H. Lafeber, and J. Bosschers (2022). Predicting cavitating propeller noise in off-design conditions using scale-resolving CFD simulations. *Ocean Engineering*, **254**, 111176.

M.S. Gritskevich, A.V. Garbaruk, J. Schutze, and F.R. Menter (2012). Development of DDES and IDDES Formulations for the $k - \omega$ Shear Stress Transport Model. *Flow, Turbulence and Combustion*, **88**(3), 431–449.

Y. Kim, I.P. Castro, and Z.T. Xie (2013). Divergence-free turbulence inflow conditions for large-eddy simulations with incompressible flow solvers. *Computers & Fluids*, **84**, 56–68.

M. Klapwijk, T. Lloyd, G. Vaz, and T. van Terwisga (2020). Evaluation of scale-resolving simulations for a turbulent channel flow. *Computers & Fluids*, **209**, 104363.

G.J. Dekkers (2024). Numerical Predictions of Airfoil Acoustics with Inflow Turbulence. *MSc Thesis TU Delft*, **MT.23/24.030.M**. Available at `https://repository.tudelft.nl/`.

F.L. Dos Santos, L. Botero-Bolivar, C. Venner, and L.D. De Santana (2022). Modeling the Turbulence Spectrum Dissipation Range for Leading-Edge Noise Prediction. *AIAA J.*, **60**(6), 3581–3592.

F.L. Dos Santos, L. Botero-Bolivar, C.H. Venner, and L.D. De Santana (2023). Inflow turbulence distortion for airfoil leading-edge noise prediction for large turbulence length scales for zero-mean loading. *The J. of the Acoustical Society of America*, **153**(3), 1811–1822.

A.F.P. Ribeiro, F.L. Dos Santos, K. Venner, and L.D. De Santana (2023). Numerical study of inflow turbulence distortion and noise for airfoils. *Physics of Fluids*, **35**(11), 115112.